Universitat Autònoma de Barcelona

Universitat Autònoma de Barcelona

Facultat de Ciències, Departament de Física

PhD supervisors:
Verònica Ahufinger Breto and Jordi Mompart Penina

From quantum memories to single-site addressing with three-level atoms

Daniel Viscor Pagès

Bellaterra, Barcelona (Spain), November 19, 2012

A la familia, els amics, i l'Anita,
ja que són ells qui fan
que valgui la pena recórrer el camí.

Agraïments

La meva gratitud esta dirigida primerament cap als meus directors de Tesi, el Jordi Mompart i la Verònica Ahufinger, no només per tota la dedicació, esforç i interès que han posat en aquest treball, sinó també per haver-me ofert la oportunitat de treballar amb ells. Crec sincerament que són uns dels millors directors que un estudiant de Doctorat pot tenir (sé que sona a peloteo però és veritat! Si no us ho creieu us convido a fer un doctorat en Òptica Quàntica a la UAB...). Voldria ressaltar també l enorme confiança que han dipositat en mi durant aquest temps, la paciència que han tingut i els ànims que m han donat en els moments (que n hi ha hagut uns quants...) en què les coses no acabaven de sortir com esperàvem. Espero sincerament que aquesta Tesi demostri haver-ne estat mereixedor.

També vull donar les gràcies a tots els companys del Grup d Òptica, tant els que van compartir el temps amb mi durant la primera etapa del Doctorat la Rocío García-Maraver, el Miquel Soler, la Sònia Fernández-Vidal, el Joan Bagudà, l Alexander Pisarchik, la Georgina Olivares, la Giovanna Morigi, l Stefano Zippilli, l Stefan Rist, la Isabel Santanach, l Antonio Picón, el Gabriele De Chiara, Carlo Ottaviani, el Hessam Habibian i el Jens Balstruch com els que han estat presents fins ara o s han incorporat darrerament al grup el Ramón Corbalán, el Gaspar Orriols, el Francesc Pi, el Juan Campos, la Maria J. Yuzuel, l Angel Lizana, el Ricard Menchón, l Alba Peinado, la Laura Lobato, el Josep Vidal, el Todor Kirilov, l Àlex Turpin, el José Luís Martínez, la Raquel Ibanez i el Joan Polo per l immillorable ambient de treball i pel suport, ajuda i consells que en un moment o altre m han donat tots ells. Voldria fer una menció especial a l Albert Benseny, pel seu bon-seny (ho havia de posar!) i la seva ajuda en... bé quasi tot el relacionat amb LaTeX, gnuplot i correcció d estil. Al Yurii Loiko per ensenyar-me i ajudar-me amb les simulacions numèriques, i resoldre m (o també plantejar-me) molts altres dubtes de Física, relacionats o no amb la Tesi. A l Alessandro Ferraro, ja que la seva incorporació al grup, i concretament al tema

que jo estava investigant, va donar l impuls necessari a la feina que en aquell moment tenia una mica estancada. I per últim al Juan Luis Rubio, per fer més amenes les correccions i discussions sobre l adressament de llocs individuals , especialment els divendres a la tarda, les discussions filosòfiques, ja fossin al bar o no, i el seu incansable ritme de treball (del qual podia ser conscient gràcies a la carpeta compartida del Dropbox).

D altra banda vull agraır, a la gent del LENS, a Itàlia, on vaig fer una estada de tres mesos, a banda d altres visites curtes, la seva hospitalitat, atenció i preocupació. En especial, dono gràcies al Maurizio Artoni, qui va supervisar directament i amb un gran interès la meva feina, al Giuseppe La Rocca, amb qui vam poder discutir d una manera sumament enriquidora alguns dels temes relacionats amb la meva Tèsi, a l Alessandro Zavatta, qui ha mostrat en tot moment un especial interès per la meva evolució, i a l Alejandra Valencia, amb qui vaig tenir la sort de treballar durant i després de la meva estada. Tots ells unes bellíssimes persones de qui he après molt durant tot el temps que hem estat col·laborant.

Deixant de banda l entorn professional, vull donar les gràcies als meus pares, per tot el que han fet i segueixen fent per mi. Ells són amb tota seguretat els primers que em van inculcar un interès científic, i van potenciar la meva innata i incansable curiositat (als amics que us queixeu de que pregunto massa per què? , aneu a reclamar a ells). I també als meus germans, el Victor i la Irene, per ser una família tan fantàstica. També agraeixo a la resta de la meva família tiets, cosins i avis de Saragossa i Tordera així com a la de l Anita, la seva preocupació, interès, i estima.

Vull agrair també el costat que m han fet i els ànims que m han donat els meus amics, l Ana tio-sóc-un-desastre Rodríguez, el Roger òstia-quin-tio Rovira, la Marta em-sembla-que m estic-adormint Suau, la Laura catastrophe Moli, l Estel aprovarem-tots Pérez, el Ferran us-havia-de-trucar Lahoz i la Mercè simpàtica-i-riallera Gotsens, en el procés de realització d aquesta Tèsi, així com els bons moments que he passat amb ells durant els anys que fa que ens coneixem (amb alguns d ells massa i tot...! És que ens fem grans!). No m oblido tampoc de Las dos Torres , *i.e.*, la Núria Torre i la Irene Torres, per l interès que han mostrat en els moments en què ens hem anat trobant.

Per últim, però no per això menys important, i de manera molt especial, vull donar-li les gràcies a l Anita. Per haver-me fet costat tot aquest temps, per ajudar-me (tant en temes directa o indirectament relacionats amb la Tesi, com en la resta de coses necessàries per a que un desastrito com jo sobrevisqui), estimar-me i

cuidar-me com ho ha fet fins ara. Gràcies.

Finalment, cal dir que la dedicació que he posat en aquest treball ha estat possible gràcies a una beca del projecte Quantum Optical Information Technology (QOIT, Consolider Ingenio 2010) atorgada pel MEC.

Contents

Preface

Quantum information science, which emerges from the combination of information theory and quantum physics, has experienced an enormous progress during the last decades, leading to revolutionary advances in a wide range of interdisciplinary fields, such as quantum computation, quantum communication, high precision measurements, and fundamental quantum science. However, the ambitious goals at which the scientific community aim, *e.g.*, quantum criptography, quantum simulators, or even quantum computation, have only started to stand out.

In most quantum information applications, atomic ensembles are normally used to store and process the information, while light is used as a tool to manipulate and perform logical operations, as well as to transmit the quantum bits between distant nodes of a quantum network. Thus, the realization of a suitable quantum interface between light and atomic ensembles is essential in quantum information science. Regarding light-matter interaction, one of the most relevant systems are three-level atoms in interaction with a pair of electromagnetic fields. Three-level systems exhibit a rich variety of phenomena due to quantum interferences between the two absorption paths for the light. These quantum interferences lead, for instance, to coherent population trapping, electromagnetically induced transparency, or stimulated Raman adiabatic passage, which have found applications in many areas of quantum information.

This thesis, which collects the research work that I have performed during my PhD under the guidance and support of my supervisors and collaborators, is mainly focused in quantum information applications using three level atoms in interaction with electromagnetic fields both at the semiclassical and fully quantum levels. The first three chapters of the work are focused on the theoretical study of novel methods to implement quantum memories for single photon qubits in superposition of two components, either polarization or frequency. Quantum memories

are devices capable of storing and retrieving on demand quantum states of light with high efficiency and fidelity, and are essential components in many quantum information applications, such as quantum repeaters or single photon sources. In Chapter 1 a general overview of quantum memories is presented. Since this is the main subject of the thesis, we dedicate a chapter to introduce the concept of quantum memories and to point out their relevance in the context of quantum information science. Moreover, we enumerate their applications and review the main figures of merit that characterize the performance of a quantum memory. Finally, we present a classification according to the different underlying physical processes or techniques on which they are based, focusing on those which will be of our interest along the following chapters.

In Chapter 2, we present two proposals for photon echo based quantum memories for polarization single photon qubits in three level systems, both in V and Λ configurations. First, for the V scheme we show the possibility of storing and retrieving a single photon pulse with two polarization components interacting with the two optical transitions of the system. This scheme implements a quantum memory for a polarization qubit without the need of two spatially separated two-level media, thus offering the advantage of experimental compactness and overcoming the limitations due to mismatching and unequal efficiencies that can arise in spatially separated memories. Moreover, we analyze the efficiency and the fidelity of the memory considering both a relative phase between the atomic levels and a phase noise due to, for instance, the presence of spurious electric and magnetic fields. Next, for the Λ configuration, we address the propagation of a single photon qubit with two polarization components in a medium prepared in a phaseonium state, *i.e.*, a coherent superposition of the ground states. We combine some of the nontrivial propagation effects that exhibit this kind of systems with photon echo techniques to propose different quantum information processing applications, such as a protocol for polarization qubit filtering and sieving as well as a tunable polarization beam splitter. Moreover, we show that by imposing a particular spatial variation of the atomic coherence phase, an efficient quantum memory for the incident polarization qubit can be also implemented in Λ-type three level systems.

In Chapter 3 we propose a quantum memory for a single photon wavepacket in a superposition of two different colors, *i.e.*, two different frequency components, in a double-Λ system using the electromagnetically induced transparency technique. Under the two photon resonance condition with the coupling fields, the

two frequency components are able to exchange energy through a four-wave mixing process as they propagate, so the state of the incident photon is recovered periodically at certain positions in the medium. We investigate the propagation dynamics as a function of both the relative phase between the coupling beams and the particular superposition state of the single photon at the input. Moreover, by considering time dependent coupling beams, we numerically simulate the storage and retrieval of a single photon qubit in a superposition of two frequency components.

Additional work in quantum information processing done during my PhD is collected in Chapters 4 and 5. In Chapter 4 we focus on the problem of single site addressing of ultracold neutral atoms in optical lattices with one atom per site. Optical lattices with one atom per site systems constitute an ideal physical system to investigate strongly correlated quantum phases which, in turn, have interesting applications in quantum optics, quantum simulation and quantum information processing, among others. However, in this kind of systems typical lattice spacings below 1 μm are needed, thus the diffraction limit restricts the addressability of individual lattice sites. In this context, we propose a single atom/single site addressing implementation based on the position dependent adiabatic passage technique considering the ultracold atoms in the lattice modeled by Λ-type three level systems coupled with a pump and a Stokes pulse. Assuming that all the atoms are initially in one of the ground states, by using a pump field with a sharp node in its spatial profile, all the atoms are transferred to the other ground state of the system via stimulated Raman adiabatic passage except those at the position of the node. Compared with coherent population trapping based techniques, our proposal allows for a higher addressing resolution and has additional advantages as robustness against parameter variations, coherence of the transfer process, and the absence of photon induced recoil. Moreover, in comparison with the recent adiabatic spin flip technique, the SLAP based SSA technique allows to reduce the interaction time with the pulses, and provides comparable or higher addressing resolutions for similar focusing requirements. Analytical expressions for the attainable addressing resolution and efficiency have been derived and compared with numerical simulations for ^{87}Rb atoms in state-of-the-art optical lattices. In Chapter 5 we extend a theoretical model capable of providing reliable predictions for the production of controlled bandwidth and pure single photon pairs experiment, using a spontaneous parametric down-conversion setup. Using the spatial-to-spectral mapping technique, which allows to transfer the spatial properties of

the pump beam to the spectral features of the down-converted photons, we obtain the optimal parameter values for the production of spectrally uncorrelated photon pairs. Different experimental configurations are analyzed, and expressions for the purity are obtained.

Finally, in Chapter 6, we summarize the main results and the conclusions are presented.

1

Overview of quantum memories

Research in the field of quantum information science, which deals with communication and computation incorporating the laws of quantum mechanics, has lead to outstanding and promising discoveries. For instance, it has been shown that quantum cryptography can allow for secure communication using public channels [1], and that quantum computing could be used to efficiently solve several problems that are prohibitively hard in classical computing [2]. The basic elements that quantum information deals with are qubits (contraction of quantum bits), which mathematically correspond to elements of a two-dimensional Hilbert space, and can be expressed as a superposition of two states, namely $|0\rangle$ and $|1\rangle$. Thus, the most general states of quantum information are superpositions of strings of qubits. Physically, a qubit corresponds to a single quantum system with two possible orthogonal states in one of its properties, and the choice of the specific physical system depends on the particular application. Specifically, in quantum computation, static, scalable, and robust quantum systems are desired, such as cold atoms, solid state systems, trapped ions, or quantum dots. In these systems, quantum information is encoded, for instance, in the internal energy, in the vibrational states, in the position, in the angular momentum or in the spin state. On the other hand, in quantum communication, photons are the preferred information carriers (flying qubits) because they propagate fast and can preserve their coherence over long distances [3]. When using photons for communication, quantum information can be encoded in several ways, such as polarization, path, photon-number, frequency, or time-bin. From such distinction between the physical systems needed to perform different quantum information tasks, it is clear that a quantum interface between light and matter is crucial for the development of quantum information processing and quantum communication.

In the context of light-matter interfaces, a quantum memory is an essential

ingredient for quantum information science, since it allows to map the quantum state of light into a storage medium and retrieve it on demand. Moreover, the use of quantum memories is not restricted to the transfer of quantum information between nodes of a quantum network, but they are necessary in a wide range of quantum information applications, as will be discussed in the following Section 1.1.

1.1 Applications

One of the main areas of application of quantum memories is found in quantum communication over long distances. The distribution of quantum states of light is affected by losses associated to the transmission channels, which limit the distance over which quantum information can be properly transmitted. For example, typical telecommunication optical fibers have losses of 0.2 dB/km at wavelengths around 1.5 μm, which for distances of the order or larger than hundreds of kilometers are very important (for a distance of 100 km the transmission efficiency is $\sim 0\ 01$). In classical communication this problem is overcome by using signal repeaters or amplifiers. However, in quantum mechanics any measurement on a transmitted qubit will destroy, in general, its quantum state, and in addition the no-cloning theorem forbids its amplification. Thus, the use of a quantum repeater [4, 5] has been proposed to overcome this difficulty, allowing for quantum communication over arbitrarily long distances. The idea of a quantum repeater is to divide the long quantum channel into shorter segments, create and store entanglement independently for each node between segments, and then distribute entanglement between those nodes via entanglement swapping [6], *i.e.*, quantum teleportation of entanglement. In this protocol, quantum memories are essential since they allow to store the entanglement distributed over adjacent sections of the transmission link.

A more fundamental application for quantum memories is the implementation of a reliable Bell s inequalities [7, 8] test, which allows to explore the basic concepts of quantum mechanics, or to prove the quantum character of a system under investigation. To test Bell s inequalities, one needs to perform measurements in an entangled bipartite system, avoiding both locality and detection loopholes simultaneously. The first aspect, the locality loophole, is related to the fact that the settings of the detection apparatus of two distant observers have to be changed randomly fast enough that no information about them can travel from one observer to the other during the course of each measurement. Secondly, to avoid the

detection loophole, the detection efficiency must be high enough to ensure that the results of the experiment can not be due to missing detection events. Therefore, a loophole-free test needs at the same time the creation of long distance entanglement, to accomplish the locality condition, and detecting the entangled systems with a high efficiency, in order to avoid the detection loophole. An interesting proposal to realize this test consists in entangling two separated ions through the interaction with photons [9]. This kind of setup can be seen as a node of a quantum repeater, in which the ions act as quantum memories. Loophole-free violations of Bell s inequalities are also important for communication complexity theory, which studies the number of qubits that two distant computers need to exchange to carry out a given task [10].

Another practical use of a quantum memory is as an on-demand single-photon source. Spontaneous parametric down-conversion (SPDC) is a common source of heralded single photons [11]. However, since it is a probabilistic process, its use is restricted for many applications. In particular, deterministic single-photon sources are important ingredients for quantum computation [12, 13] and certain quantum repeater protocols [5, 14]. A non-deterministic source of photon pairs, *e.g.*, SPDC, can be turned into a deterministic source of single photons by storing one of the photons of the pair in a high efficiency memory [15, 16]. The other photon is used to herald the presence of its partner inside the memory, *i.e.*, detection of the heralding photon indicates that the memory is loaded and the stored photon can be released on demand.

Finally, another important application of quantum memories is related to precision measurements in magnetometry, clocks and spectroscopy. By creating long-lived entanglement between two atomic ensembles it is possible to reduce the projection noise, caused by the uncertainty relation, and obtain measurements with precision beyond the quantum limit [17 19]. In this context, the entanglement between atomic ensembles can be created by storing squeezed states of light [20, 21] or by squeezing the collective atomic spin [22 24].

1.2 Performance criteria

Since different applications demand quantum memories fulfilling different requirements it is difficult to establish a general figure of merit to evaluate the performance of a quantum memory set up. For instance, Sangouard *et al.* [5] exposed the stringent requirements for a practical quantum memory in the context of quan-

tum repeaters, *e.g.*, multimode storage on the timescale of seconds with efficiencies larger than 90% and bandwidths greater than 1 GHz. In the following, we provide an overview of the figures of merit usually considered in the literature. Note that, in some cases, important performance benchmarks for some techniques or quantum memory protocols will be mentioned in order to give an idea about the state of the art. The mentioned protocols will be discussed in more detail in Section 1.3.

1.2.1 Fidelity

A quantum memory stores, in general, a quantum state of light which can be represented by a density matrix $\varphi =$, where is the state vector. After the recalling process, the output state φ should be as close as possible to the input one. The fidelity gives a measure of the distance between the two quantum states in a Hilbert space, and is defined as [25]

$$F(\varphi\ \varphi) = \left(\mathrm{Tr}\quad \overline{\overline{\varphi}\varphi\quad\overline{\varphi}}\right)^2 \tag{1.1}$$

For normalized states it takes values in the range [0 1] being one if and only if the two quantum states are equal, $\varphi = \varphi$. Therefore, the fidelity is related to the overlap between the input and retrieved quantum states. Note that if the input state φ is pure, Eq. (1.1) turns into $F =$ φ . The way to asses the fidelity of a quantum memory may depend on the scheme considered. For instance, depending on the conservation of the number of photons in the retrieval process, conditional or unconditional fidelities can be considered. The conditional fidelity is calculated assuming that all the input photons have been retrieved, *i.e.*, it is conditioned on the reemission of the photons, while the unconditional fidelity is an absolute quantity and thus will take lower values than the former. In addition, in experiments where several measurements are needed to reconstruct the state of the reemitted photons an average fidelity has to be defined.

Notice that, depending on the application of the quantum memory, the fidelity may not be the most important figure of merit. A given quantum memory with a high fidelity may present errors which are hard to correct, while protocols with a poor fidelity and particular kinds of errors can be appropriate for a specific application.

1.2.2 Efficiency

Another performance criterion that is usually considered is the efficiency η of the quantum memory. From a classical point of view, the efficiency is the ratio between the stored and the recalled light pulse energies. In the case of memories for single photons, the efficiency definition can be reformulated in terms of the write (P_{write}) and read (P_{read}) probabilities, $\eta = P_{\text{write}} P_{\text{read}}$. The former corresponds to the probability of storing the input photon while the latter is the probability of retrieving it, provided it has been successfully stored previously. This distinction between storage and reemission probabilities is important because, depending on the quantum memory implementation, one can find situations in which a poor storage efficiency is obtained although presenting a very efficient reemission process, or *vice versa*. For example, photon echo type quantum memories [26], which will be discussed in Subsection 1.3.6, exhibit a high reemission efficiency when the photons are recalled in the backward direction, albeit the absorption efficiency is limited by the optical depth of the storage medium. However, if the photons emerge in the forward direction the reemission efficiency is very limited even at large optical depths [27], *i.e.*, for high absorption probability.

Clearly, the efficiency that can be achieved in a quantum memory depends not only on the technique used to perform the storage but also on the medium itself. For example, in atomic ensembles, where the collective interference of all the atoms may enhance the macroscopic coherence, the efficiency can be in general close to one [28], and it is mainly limited by decoherence losses. In particular, quantum memories with efficiencies around 70% have been achieved on solid state materials [29] and in cold atomic ensembles [30]. On the contrary, for single atomic systems the limited interaction probability implies a small efficiency, which can be increased by using optical cavities to enhance the weak atom-light coupling [30, 31].

1.2.3 Storage time

The time that a memory is able to store a quantum state is another important feature, since it has to be long enough to carry out a given task. For instance, in quantum communication, the transmission time between distant nodes of a network imposes a limit for the storage time of the quantum memory [5, 32]. Specifically, the characteristic timescale for the storage during entanglement distribution, required for the quantum repeater implementation, is the light travel

time $t_L = L\ v$, where v is the speed of light in the medium and L the distance between two nodes. Then, for $L = 1000$ km, t_L ranges from several milliseconds to few seconds depending on the network architecture [4, 33]. The main limitation in the storage time comes from losses and decoherence of the storing medium. Thus, the system used for the storage plays an essential role, and it should present long coherence times, small spontaneous decay rates, and reduced losses. For example, the current record of storage time in a quantum memory (> 1 s) has been achieved using solid state systems (rare-earth ion doped solids) [34], which present long spin coherence lifetimes at low temperatures. Even though the decoherence mechanisms can be reduced by choosing a suitable material, they are always present. Thus, long storage times are typically accompanied by poor retrieval efficiencies, and one needs to look for a compromise between these two quantities.

1.2.4 Multimode capacity

The number of modes that a quantum memory is able to store while maintaining the performance requirements depends on the memory mechanism [35, 36]. A high multimode capacity is not an essential feature, but it allows to increase the repetition rate in quantum communication [37, 38]. To quantify the number of modes that a quantum memory can store one needs to focus on the particular setup. For instance, the number of temporal modes that can be stored in photon echo and in electromagnetically induced tranparency (EIT) based quantum memories depends on the optical depth [39, 40]. The exception is the approach based on atomic frequency combs, in which the multimode capacity depends on the number of peaks in the comb [36], and has been shown to be capable of storing ~ 64 temporal modes [41]. Recently, a train of 1060 weak pulses has been stored by using frequency modulation, though with a very limited retrieval efficiency [42]. Note that, in general, most of the approaches that consider storage of multiple modes are in the time-domain. However, one interesting perspective in atomic ensembles is the possibility to store multiple spatial modes to generate quantum holograms [43 45].

1.2.5 Bandwidth and wavelength

The bandwidth in which a quantum memory can operate is another interesting aspect to consider, and is closely related to the temporal multimode capacity. A large

bandwidth allows to store short pulses and thus to increase the repetition rate. Moreover, it has a direct influence in the multiplexing capability of the memory, *i.e.*, the number of channels in which qubits can be stored. Large bandwidths are also required to match the spectral range of the memory with entangled photons sources as SPDC [46]. The group of techniques that offer an intrinsic larger bandwidth are those based on photon echo [26], due to their inherent broad absorption spectrum caused by the inhomogeneous broadening, allowing also for bandwidth conversion [40]. However, recently, unprecedent storage bandwidths around 1.5 GHz have been demonstrated in Raman type memories [47] (see Subsection 1.3.4) using strong broadband control pulses.

Regarding wavelength requirements, for long distance transmission of qubits it is necessary that the quantum states of light have the appropriate characteristics to be transmitted within the range of small attenuation of a given channel, *e.g.*, $\lambda \sim 1\ 5\,\mu$m in telecommunication optical fibers. Recently, storage of single photons in the telecommunication wavelength domain has been realized [46, 48, 49] using photon echo techniques in solid state systems.

1.3 Classification

Due to the vast research carried out on the field of quantum memories, it is difficult to establish a proper classification. Different criteria could be used depending on, *e.g.*, the technique or physical process on which the quantum memory is based, the kind of quantum states that it stores, or the medium used for the storage [50]. In this Section we will present a classification based on the different techniques that are used to implement quantum memories. In addition, a short review of each technique will be performed, giving a special emphasis to those that will be used along this Thesis, namely electromagnetically induced transparency (EIT) and photon-echo based techniques.

1.3.1 Optical delay lines and cavities

One of the simplest and intuitive ways to store light is to use a delay line, for instance a coiled optical fiber, in which a light pulse travels a long path before exiting the line, thus increasing its flying time. However, this approach has important drawbacks such as fixed and relatively short storage times (for a 15 km fiber operating at the telecommunication range the storage time at which half of the photons are lost is $\sim 70\,\mu$s). To overcome these limitations, a setup consisting

in a delay line loop with an electro-optical switch has been proposed [51]. In this scheme, the electro-optical switch closes the loop when the detection of a signal photon, coming from SPDC, heralds the presence of an idler photon inside the fiber. However, the storage time is still fixed to a multiple of the round trip time. Another option is to use a high-quality cavity, in which the photons bounce back and forth between high reflectance mirrors. In this case, the injection and retrieval of photons can be done using an electro-optical switch [52] (similarly as in [51]), a pair of narrow cavities with a variable transmission probability [53], interaction with single atoms passing through the cavity [54], or by controlling the quality factor of the cavity [55, 56]. The main issue regarding the storage of light in cavities is the fact that long storage times require large round trip of the photons, but this implies a limited on-demand capability. On the contrary, short cycle times increase the losses of the cavity and diminishes the efficiency of the memory for long storage times.

1.3.2 Quantum non-demolition (QND) measurement and feedback

The first demonstration of storage of a quantum state of light into an atomic ensemble was done by Julsgaard *et al.* in 2004 [57] applying techniques used to entangle two separated atomic ensembles via interaction with off resonant light pulses [23].

When a far detuned light field passes through an ensemble of two-level atoms it produces no population excitation, but the off resonant interaction may produce a phase variation both in the atoms and in the light field. This interaction causes an entanglement between the atomic angular momentum and the polarization of light, which can be used to implement a quantum memory via a feedback protocol. In particular, the quantum storage of the light pulse is performed in three steps: (i) optical pumping to initialize the atoms, (ii) interaction of the light pulse, propagating in the z direction, with the atoms, (iii) measurement of the transmitted light, and (iv) feedback onto the atoms conditioned on the measurement result. In step (i) the atoms are prepared in a coherent spin state in which the total angular momentum is oriented in the x direction, J_x J_x. However, due to the uncertainty principle, the atomic transverse components of the angular momentum J_y and J_z have a certain spreading along the y and z directions. On the other hand, any polarization state of light can be described

using the Stokes operators

$$S_x = \frac{1}{2}\left(a_x a_x - a_y a_y\right) \tag{1.2}$$

$$S_y = \frac{1}{2}\left(a_x a_y + a_y a_x\right) \tag{1.3}$$

$$S_z = \frac{1}{2i}\left(a_x a_y - a_y a_x\right) \tag{1.4}$$

where a_ξ and a_ξ ($\epsilon = x\ y$) are the photon creation and anihilation operators for photons polarized in the ϵ direction. In the experiment, the input state is encoded in a y-polarized pulse. Thus, during step (ii), J_z causes a Faraday rotation, which changes S_y. In turn, the J_y component of the atomic angular momentum is affected by the angular momentum of the photons S_z. Therefore, the light pulse and the atomic ensemble become entangled. In the next step, (iii), a measurement on the polarization of the emerging light pulse is performed which determines S_y. The result of this measurement determines the characteristics of a magnetic field pulse that is sent back to the atomic ensemble, in step (iv). The feedback magnetic field produces a change in the angular momentum of the atoms in such a way that the initial Stokes operator S_y of the photons is mapped into J_z. This results in both components of the optical polarization being transferred to the atomic angular momentum. In the experiment [57] fidelities around 70% where obtained for storage times of $\sim 0\ 7$ ms.

Later, a variation of this technique, consisting in the teleportation of a quantum state of light into the atomic memory was implemented [58]. This was achieved by mixing in a beam splitter the weak field to teleport with a strong off resonant pulse emerging from the atomic ensemble, and feeding-back the result of an homodyne measurement into the atoms.

1.3.3 Electromagnetically induced transparency (EIT)

One of the most usual methods to implement a quantum memory relies on the technique known as electromagnetically induced transparency (EIT) [59 61]. This technique consists in rendering a three-level medium transparent for a probe light beam by means of quantum interference effects induced by the presence of a strong control field. Specifically, the control field creates two absorption paths for the probe that interfere destructively. Besides the suppression of the absorption, the control field induces also a variation of the refraction index of the medium, which allows to slow down a probe pulse, and even stop and map it into the atomic

coherence.

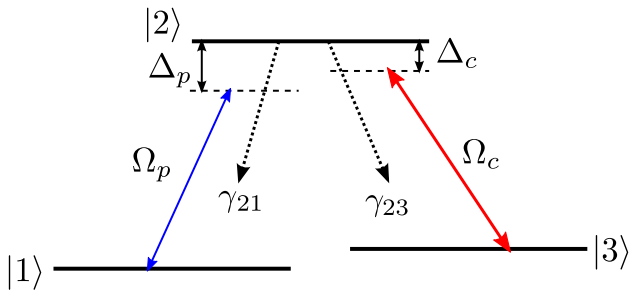

Figure 1.1: Three-level atom in a Λ-type configuration interacting with probe and control fields of Rabi frequencies Ω_p and Ω_c, respectively. The probe field couples transition $1 - 2$ with detuning $\Delta_p = {}_p - {}_{21}$, being ${}_p$ and ${}_{21}$ the frequencies of the probe and $1 - 2$ transition, respectively, while the control drives transition $3 - 2$ with detuning $\Delta_c = {}_c - {}_{23}$, with ${}_c$ and ${}_{23}$ the frequencies of the control and $3 - 2$ transition, respectively. γ_{21} and γ_{23} are the spontaneous decay rates from the excited state 2 to the ground states 1 and 3, respectively.

Although EIT can be implemented in various three-level atomic schemes, such as the V or the cascade configurations, for protocols concerning light storage the most used level configuration is the Λ type because allows to store the light into the long living ground state coherence. Thus, in what follows we focus on this atomic level scheme, which is depicted in Fig. 1.1. In this configuration, the probe and control fields, with respective Rabi frequencies Ω_p and Ω_c, are coupled to each of the two optical allowed transitions, $1 - 2$ and $3 - 2$, respectively, with detunings Δ_p and Δ_c (see the caption of the figure for the definition). The spontaneous emission decay rate from 2 to 1 (3) is γ_{21} (γ_{23}).

Many of the interesting features of the EIT technique can be understood by considering the linear susceptibility $\gamma^{(1)}$, which determines the optical response of the medium to a probe field. In particular, the real and imaginary parts of $\gamma^{(1)}$ are related to the dispersion and absorption properties of the medium, respectively. For the three-level system presented in Fig. 1.1 the linear susceptibility reads [61]:

$$\gamma^{(1)}(\ {}_p) \quad \frac{\gamma_{12}\,(\Delta_p - \Delta_c)}{\Omega_c^2\ 2 - (2\Delta_p + i\gamma_{12})\,(\Delta_p - \Delta_c)} \tag{1.5}$$

The imaginary and real parts of Eq. (1.5) are plotted in Fig. 1.2(a) with solid and dotted lines, respectively, as a function of the probe laser frequency ${}_p$, for $\gamma_{21} = 5\gamma_{23}$, $\Delta_c = 0$, and $\Omega_c = 10\gamma_{23}$. Fig. 1.2(b) shows the case with $\Omega_c = 0$, *i.e.*, the probe response in a two-level system. As we see, the presence of the control

field modifies the absorption and dispersion curves in such a way that the typical absorption profile for a two-level system [Fig. 1.2(b)] split into two absorption peaks located at $_p = \ _{21} \pm \Omega_c$ 2. Therefore, while the separation of the two resonance lines is determined by Ω_c, its width is given by the decay rate γ_{21}, and the condition $\Omega_c > \gamma_{21}$ must be satisfied in order to produce an appreciable splitting. From Fig. 1.2(a) it is clear that the absorption of the probe beam is suppressed at resonance $_p = \ _{21}$. The spectral range without absorption is the so called transparency window, or EIT window, and it is proportional to $\Omega_c^2 \ \gamma_{21}$. As pointed out, the non-absorption at resonance, *i.e.*, the transparency window, is due to a destructive interference between, neglecting higher order contributions, two possible absorption paths for the probe light: (i) a direct transition to the excited state by absorbing a probe photon, and (ii) the absorption of one photon of the probe field with a subsequent reemission and absorption of two photons of the control field.

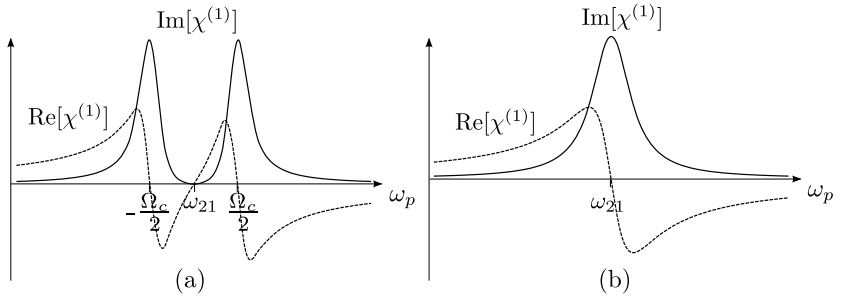

Figure 1.2: Real (dashed lines) and imaginary (solid lines) parts of the linear susceptibility, Eq. (1.5), for a three-level atomic system as a function of the probe frequency, for $\gamma_{21} = 5\gamma_{23}$, $\Delta_c = 0$, (a) $\Omega_c = 10\gamma_{23}$ and (b) $\Omega_c = 0$.

Slow and stopped light

Due to the Kramers-Kronig relations, a change in the absorption properties of the medium is accompanied by a change in the dispersion, and thus in the index of refraction n since $n(\ _p) \equiv \ \overline{1 + \mathrm{Re}[\gamma^{(1)}(\ _p)]}$. For a monochromatic wave, the propagation velocity, or phase velocity v_{ph}, depends on the index of refraction as $v_{ph}(\ _p) \equiv \ _p \ k_p = c \ n(\ _p)$, being k_p the wavenumber of the probe and c the speed of light in vacuum. If we consider a non-monochromatic wave, *e.g.*, a pulse wavepacket, each Fourier component of the pulse will travel at a different phase velocity. In this situation the group velocity at which the pulse envelope

propagates is defined as [61]

$$v_g \equiv \frac{d\ _p}{dk_p} = \frac{c}{n + \ _p(dn\ d\ _p)} \tag{1.6}$$

The term $dn\ d\ _p$ implies that a steep variation in the refractive index with the frequency produces a significant variation in the group velocity. In a two-level system, the region with a large slope in the real part of the susceptibility coincides with the maximum of absorption of the medium, as is shown in Fig. 1.2(b). However, when the control field is present the steep dispersion region around $_{21}$ corresponds to a range of $_p$ with no absorption [62] [see Fig. 1.2(a)]. This allows the propagation of light pulses with extremely small group velocities under EIT conditions [63].

Light storage using this technique can be achieved by dynamical variation of the group velocity [64], *e.g.*, by changing in time the strength of the control field. The first demonstrations of light storage were done by Liu *et al.* [65] and Phillips *et al.* [66] in cold and hot atomic vapors, respectively (for a general review see [61, 67]). The procedure to achieve stopped light consists in first slowing down a light pulse in such a way that it fits inside the storage medium. Note that the reduction in the group velocity implies a spatial compression of the light pulse by a factor $v_g\ c$, because its front end entering the medium propagates much slower than its back end. Therefore, once the pulse has completely entered in the medium the control field is adiabatically turned off. This decrease in the control field amplitude leads to a reduction of the group velocity, as well as to a narrowing of the transparency window (see Fig. 1.2). This means that the medium turns opaque for the probe pulse, which it is totally absorbed, and hence mapped into the ground state coherence of the atomic ensemble. Assuming an atomic medium fomed by Λ-type atoms initially prepared in state 1 , if the probe field corresponds to a single photon wavepacket, the state describing the atoms of the medium after the absorption has the form

$$= \frac{1}{\overline{N}} \sum_{i=1}^{N} 1_1 \quad 3_i \quad 1_N \tag{1.7}$$

which is a collective superposition state, where all the N atoms of the medium are in the ground state 1 except one being in state 3 . This coherent mapping implies that the information carried by the light is stored in the atomic coherence, preserving its quantum properties. The process can be reversed, after a time lim-

ited by the decoherence between the ground states, by turning on again the control field. This leads to the reemission of a probe pulse with the same properties as the original one, propagating transparently in the medium, provided the incoherent processes are negligible and the variation of the control field is adiabatic, thus reducing the losses.

One interpretation of the slow light and the light storage phenomena based on EIT can be obtained using the dark-state polaritons picture [64, 68], where dark (Ψ) and bright (Φ) quantum fields are defined as linear combinations of atomic and photonic excitations propagating inside the medium:

$$\Psi(z\ t) = \cos\theta(t) E_p(z\ t) - \sin\theta(t)\quad \overline{\varphi}\phi_{13}(z\ t) \tag{1.8a}$$

$$\Phi(z\ t) = \sin\theta(t) E_p(z\ t) + \cos\theta(t)\quad \overline{\varphi}\phi_{13}(z\ t) \tag{1.8b}$$

with E_p the electric field operator of the probe single photon, ϕ_{13} the atomic coherence between the ground states 1 and 3 and φ the atomic density of the medium. In this picture, the mixing angle θ is defined in terms of $\cos\theta(t) = \Omega_c(t) \quad \overline{\Omega_c^2(t) + g^2\varphi}$ and $\sin\theta(t) = g\ \ \overline{\varphi} \quad \overline{\Omega_c^2(t) + g^2\varphi}$, being $g = \mu \quad \overline{{}_0\ 2\ \epsilon_0 V}$, μ the dipole moment of the 1 - 2 transition, the reduced Planck s constant, ϵ_0 the electric permittivity in vacuum, and V the quantization volume. Under EIT conditions, *i.e.*, in the absence of absorption, only the dark polariton Ψ plays a role ($\Phi = 0$) and satisfies the propagation equation:

$$\left[\frac{}{t} + c\cos^2\theta(t)\frac{}{z}\right]\Psi(z\ t) = 0 \tag{1.9}$$

which describes a shape-preserving propagation with velocity $v_g(t) = c\cos^2\theta(t)$. Therefore, it is easy to see that by adiabatically turning off and on the control field [61], *i.e.*, varying $\theta(t)$ from 0 to ν 2 and from ν 2 to 0, respectively, the polariton can be decelerated, stopped, and accelerated, which corresponds to the mapping of light into the spin coherence [$\theta = \nu$ 2 in Eq. (1.8a)], and back to the photonic modes [$\theta = 0$ in Eq. (1.8a)]. The adiabaticity conditions for the turning off and on of the control field are rather weak [68, 69] in such a way that for an already weak control field, and thus a small group velocity, even an instantaneous switch off of the control field would lead to small losses [65, 69].

Since the first demonstrations of light storage using the EIT technique [65, 66], a lot of research has been done. In particular, the technique has been extended to solid state media [34, 70], and coherence properties of the memory have been

investigated both in classical [71] and in quantum [72] regimes. Moreover, optimal conditions for storage and retrieval have been analyzed [73, 74], leading to efficiencies of 41%. More recently, storage of entangled and superposition states of light have been proposed [75], and experimentally reported [76 78]. In Ref. [76], storage of a polarization superposition state in cold cesium atoms is demonstrated, while in Ref. [77] two-frequency modes of a weak light pulse are stored in cold rubidium vapor, paving the ground to two-color quantum memories. Moreover, in Ref. [78] a four-partite entangled state is stored and retrieved using four different laser cooled atomic ensembles.

One of the main limitations to implement quantum memories using the EIT approach is that the transparency window restricts the bandwidth of the pulses to a few MHz. Nevertheless, EIT can be used in inhomogeneously broadened systems, provided the two-photon resonance condition is satisfied, though in this case the transparency window is significantly narrowed [79] due to the reduced power broadening for the off-resonant atoms. In addition, storage and retrieval of light pulses is possible with relatively high two photon detunings $\Delta_p - \Delta_c$, for large enough optical depths [80].However, although a high optical depth is also important for a high retrieval efficiency, it produces a growth of the amount of fluorescence noise, which has been shown that could severely limit the application of EIT for truly quantum state storage in warm vapors [81]. Moreover, four-wave mixing effects that degrade the fidelity of the light storage process can also appear as a consequence of a strong coupling and high optical depths [82, 83]. Finally, as previously mentioned, the storage time is limited by the spin decoherence and atomic motion, *i.e.*, collisions, in the case of atomic gases. This limitation is overcome by using solid state systems, where the atoms are `frozen and the spin decoherence times can be of the order of seconds. Indeed, in Ref. [34] a record storage time of 2.3 s was achieved using the EIT approach in a $Pr : Y_2SiO_5$ crystal.

1.3.4 Raman memory

Closely related to the EIT-based quantum memory is the Raman memory [47, 84 86]. In this approach, off resonant Raman interaction of a weak and a strong control pulse with a Λ-type medium gives access to the long-lived ground state coherence of the system. The coupling of the two ground states of the system is made by means of a two-photon process through a virtual transition, thus avoiding fluorescence losses. This technique is similar to the EIT-based storage, except that, usually, the optical fields are detuned far away from the optical transition, while

keeping the two photon resonance. Whereas in EIT the dispersion associated with the quantum interference of two absorption paths is used to slow down a signal pulse inside an atomic ensemble, in the Raman memory the large detuning destroys this interference. This means that the signal is mapped into the ground state coherence without implying reduction in the signal group velocity, by a stimulated Raman scattering process [87], *i.e.*, absorption and subsequent stimulated emission of photon via a non-resonant intermediate quantum state of the atoms.

Usually this approach requires that the condition $\Delta_p \gg |\Omega_c|$ is satisfied. Thus, an adiabatic elimination of the excited state $|2\rangle$ can be performed.This approximation allows to treat most of the cases [84, 88, 89] and clearly differentiates the Raman from the EIT memories. However, in Ref. [90] a detailed comparison between EIT and Raman process demonstrated that actually, both the EIT and the stimulated Raman processes occur at the same time. The difference between them is that, depending on the ratio between the probe pulse spectral width and the transparency window, one of the processes predominates over the other, independently of the Δ_p parameter. Thus, far from compete between them, they complement each other: while EIT is more suitable to store pulses with time durations larger than the lifetime of the excited state, the Raman memory is useful to store short pulses.

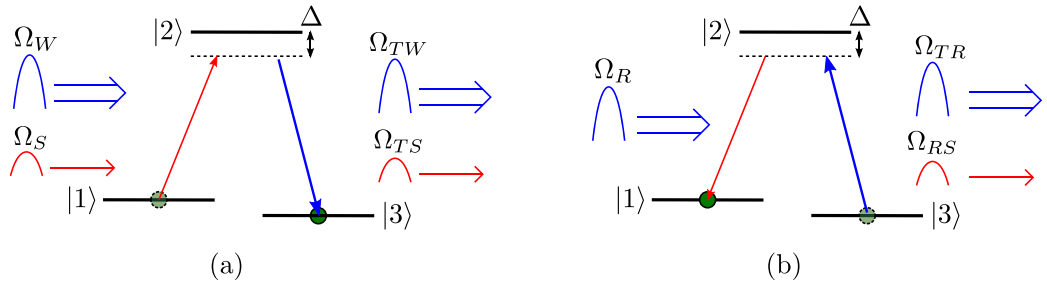

Figure 1.3: Performance of the Raman memory. (a) The off-resonant strong write field with Rabi frequency Ω_W, drive the $|2\rangle - |3\rangle$ transition of the three-level Λ atoms of an ensemble with all the population in state $|1\rangle$. A weak signal field, with Rabi frequency Ω_S and coupling the $|1\rangle - |2\rangle$ transition, is sent together with the write pulse and, for an optimal temporal overlap between them and a high enough intensity of the write field, a stimulated Raman process occurs, which transfer the atomic population from state $|1\rangle$ to $|3\rangle$. The transmitted parts of the signal and write pulses are denoted by the Rabi frequencies Ω_{TS} and Ω_{TW}, respectively. (b) After a temporal delay a strong read pulse is sent, with Rabi frequency Ω_R, and the stored excitation is recovered and mapped into a read-out signal (Ω_{RS}) which is transmitted with the strong read pulse (Ω_{TR}).

The first proposals of Raman memories focused in the mapping of light, either squeezed states [84] or broadband signals [88], into the spin coherence, but several difficulties for the read-out of the memory were pointed out. In particular, intense read control fields and a proper overlapping conditions between the control and the stored signal were necessary. Although Raman storage has been studied during last decade [84, 88, 90], it has been only experimentally realized recently, demonstrating storage of broadband signals [47], implementation of the technique at room temperature [85], and efficient retrieval of the stored light by using multiple read pulses [86]. The underlying physical process of those experiments is depicted in Fig. 1.3, where an off-resonant strong control and a weak signal pulses, with Rabi frequencies Ω_W and Ω_S, respectively, are sent into an ensemble of Λ-type atoms under the two photon resonance condition, coupling transitions $2 - 3$ and $2 - 1$, respectively [Fig. 1.3 (a)]. By stimulated Raman scattering some of the atoms can change its energy sate from 1 to 3 . In the figure, we denote the transmitted write and signal pulses with Rabi frequencies Ω_{TW} and Ω_{TS}, respectively. Note that the transmitted part of the signal is entangled with the atomic ensemble. Next, a strong enough read pulse with Rabi frequency Ω_R (the transmitted part is denoted by Ω_{TR}), coupled to $2 - 3$ transition, reverses the mapping of the spin coherence into a read-out of the previously stored signal photons, with Rabi frequency Ω_{RS} [Fig. 1.3 (b)]. As mentioned, this scheme allows for a broadband pulse storage, because the short control pulse creates a broad virtual state to which the signal pulse is coupled under two-photon resonance. In particular, an unprecedent storage bandwidth of $\sim 1\,5$ GHz was achieved in Ref. [47], that was limited only by the detector response time. The main drawback for this approach is the requirement of strong control fields needed for writing and reading the signal, which are the limiting factors for a high efficiency. However, it has been shown recently that the low efficiency can be significantly improved by sending multiple pulse readings [86], which transforms the stored signal into a multi time bin with a nearly perfect overall efficiency.

1.3.5 DLCZ protocol

A variation of the Raman memory technique uses spontaneous Raman scattering instead of stimulated, so the atomic excitation is not produced by an external photon entering the ensemble, but by the ensemble itself. This is the basis of the Duan-Lukin-Cirac-Zoller (DLCZ) protocol [91], to create long-lived, long-distance entanglement between atomic ensembles, which is sketched in Fig 1.4. In the

DLCZ protocol, a classical (write) optical field, coupled with one optical transition of the Λ-type atoms, creates a collective excitation which is heralded by the emission of an idler photon [see Fig. 1.4(a)]. Next, after a desired storage time, that can be larger than 5 ms [92], this excitation is recovered in the form of a signal photon, which is correlated to the idler [93], by applying a control (read) field to the other optical transition of the system [see Fig. 1.4(b)]. Note that this technique relies on spontaneous Raman scattering, so it is a probabilistic process, and depends on the control field power.

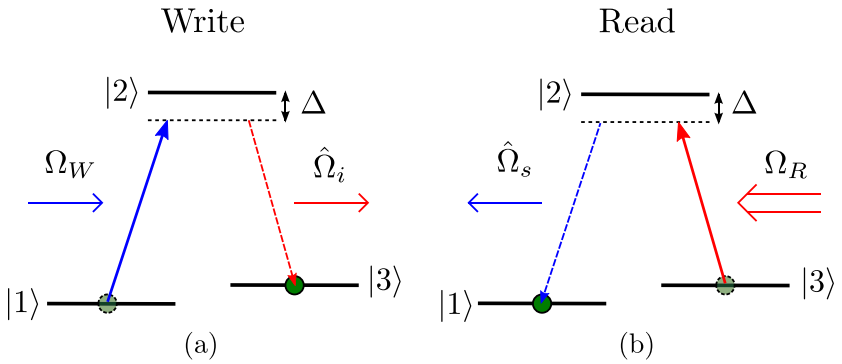

Figure 1.4: Steps of the DLCZ protocol. (a) Ensemble of Λ-type three-level atoms interacting with a weak off-resonant write pulse, with Rabi frequency Ω_W and coupled to the $|1\rangle - |2\rangle$ transition. With a small probability, one of the atoms of the ensemble converts, by means of a spontaneous Raman scattering process, a single photon of the write pulse into an idler photon, of Rabi frequency $\hat{\Omega}_i$, corresponding to the $|2\rangle - |3\rangle$ transition. The idler photon heralds the preparation of the memory with one of the atoms of the ensemble in state $|3\rangle$. (b) For the read-out a strong read pulse, of Rabi frequency Ω_R and coupled with the $|3\rangle - |2\rangle$ transition, is sent to the atomic ensemble. This may produce a Raman transition of the excited atom to state $|1\rangle$, with the subsequent emission of a signal photon $\hat{\Omega}_s$ in the $|2\rangle - |1\rangle$ transition.

To perform long-distance entanglement between two remote atomic ensembles using this technique [94, 95], the two ensembles are simultaneously illuminated with write pulses, and a beam splitter placed between the emission channels of the idler photons mixes the two paths. Therefore, if a photon is detected at one of the outputs of the beam splitter it is impossible to know which ensemble has emitted the photon, and the two ensembles must be described by an entangled superposition state. The DLCZ protocol has shown quantum state transfer between light and matter [96–99], thus it is suitable for applications in quantum repeaters. However, it does not allow for a direct storage of qubits coming from

outside the system. To deal with this limitation, teleportation of an arbitrary photonic state to an atomic ensemble, which also serves as a memory, has been shown using the DLCZ protocol [100]. Note that, since the generation of entanglement is performed through spontaneous Raman scattering, the memory works only in a post-selected way. To cope with this, one possibility is to boost the power of the control beam, in order to increase the Raman transfer probability. Alternatively, several proposals have addressed this problem by enhancing the coupling between the ensemble and the light through optical resonators [30, 101]. Moreover, in Ref. [30] an unprecedent combination of efficiency (73%) and storage time (3.2 ms) has been achieved using cold ^{87}Rb atoms in a ring cavity as storage medium.

1.3.6 Photon echo

There are several schemes for quantum memories based on the photon echo effect [102]. All of them rely on transferring the quantum state of a light pulse to a collective atomic excitation taking advantage of the inhomogeneous broadening of the storage medium (for a review see Ref. [26]). The inhomogeneous broadening allows for the absorption of the different frequencies of the incident pulse by different groups of atoms, and just after the absorption, a dephasing appears between them. The key point of the photon echo techniques is to force the rephasing of the atoms in order to induce a collective reemission of the stored information. As an example, consider an inhomogeneously broadened ensemble of N two-level atoms interacting with a light pulse. After the absorption of the pulse, the state of the atomic system can be described as a coherent superposition of one of the atoms excited and the rest in the ground state:

$$= \sum_{j}^{N} c_j e^{-i\delta_j t} e^{ikz_j} \; 0_1 \quad 1_j \quad 0_N \tag{1.10}$$

where c_j is the probability amplitude that the atom j absorbs the photon, z_j and δ_j are, respectively, the position of the atom j and its detuning with respect to the carrier frequency of the pulse, k is the wavevector of the light field, and $0_1 \quad 1_j \quad 0_N$ denote the collective state of all the atoms being in the ground state and j in the excited state. Initially $\delta_j t = 0$, so all the atoms at position z_j are in phase, but immediately after the absorption the atoms start to dephase due to the different detunings δ_j. Therefore, to achieve a collective rephasing one needs to control or modify this detuning, for instance by means of external fields, in such

a way that at a later time the phases of all the atoms become equal again. Once the atoms are in phase a collective atomic coherence is created and this triggers the reemission of the absorbed pulse. Depending on the detuning distribution of atoms considered, one can divide the photon echo techniques into two groups: the controlled reversible inhomogeneous broadening (CRIB) and atomic frequency comb (AFC) techniques.

Controlled reversible inhomogeneous broadening (CRIB)

One possibility to achieve the collective rephasing is to invert the sign of the detuning once the incident photon has been absorbed, in such a way that the temporal evolution of each atom is `reversed . This idea of reversing the evolution of the system was already present in the original spin [103] and photon echo [102] proposals. Although the original photon echo technique presents serious drawbacks regarding the implementation of a quantum memory, such as poor fidelity associated with an inevitable amplification process [104], it motivated the work by Moiseev *et al.* [105] for storage of a single photon in an inhomogeneously broadened two-level atomic vapor.

In this proposal, depicted in Fig. 1.5, the authors considered a single photon entering a Doppler broadened gas, composed by two level atoms, represented in the figure by states $|1\rangle$ and $|2\rangle$. Due to the inhomogeneous broadening (IB) each frequency component of the single photon pulse is resonant with a different group of atoms with a given velocity, so the photon is collectively absorbed by all the atoms of the medium [Fig. 1.5(a)]. This implies that after the absorption, the state of the atomic system can be described as a superposition of the form given in Eq. (1.10), with all the atoms in the ground state except one in the excited. Before the single photon enters the medium all the atoms are in phase, but just after the absorption, because of the IB, each atom evolves differently due to the different detunings, and they start to dephase. This dephasing prevents a reemission of the photon, and implies that, in the Bloch sphere, the Bloch vector of each atom precesses with a different velocity depending on its detuning. The key idea of the photon echo, is to restore the initial conditions, *i.e.*, the phase, to trigger the reemission of the absorbed pulse at will. With this purpose, a ν-area pulse [Fig. 1.5(b)] is used to transfer the population to a long lived auxiliary level, *e.g.*, an hyperfine metastable state, and after a desired time, another ν pulse, counterpropagating with respect to the first one, transfers back the population to the excited state [see Fig. 1.5(c)]. Note that during the time in which the

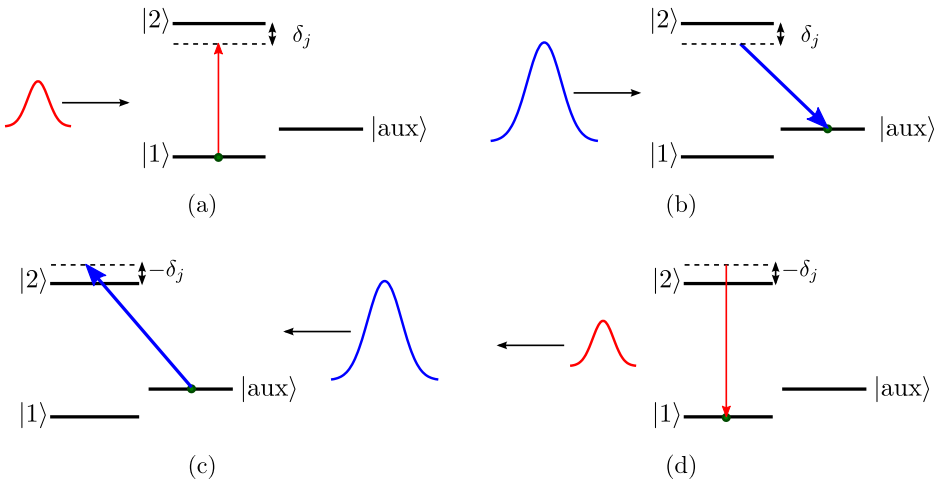

Figure 1.5: Scheme of Moiseev *et al.* [105] proposal. (a) Single photon entering the Doppler broadened gas and interacting with the $1 - 2$ transition of the atoms with a detuning depending on the atomic velocity. The inhomogeneous broadening produces a collective absorption and a dephasing between the atoms. (b) A ν pulse transfers the population to an auxiliary state aux which pauses the inhomogeneous dephasing and, after a time, another ν pulse (c) transfers back the population to the excited state 2 , with the opposite detuning. (d) The different sign of the detunings implies that the atoms start to rephase and eventually a collective reemission is produced.

population is in the auxiliary state, which can be many orders of magnitude longer than the lifetime of the excited level, the inhomogeneous dephasing is stopped. Due to the Doppler effect, the pair of ν pulses effectively change the sign of the detuning with which each atom is evolving, and additionally set the phase matching condition necessary for the reemission of the single photon. The effective change in the sign of the detuning implies that the different phases of the atoms start to evolve in the opposite way, *i.e.*, the Bloch vectors rotate in the opposite direction, and eventually they will be in phase again. When this rephasing is achieved, the reemission of a time reversed copy of the initial single photon, which propagates in the backward direction, is produced [Fig. 1.5(d)].

This process can be understood as a time reversal symmetry in the evolution equations of the system. Considering a single weak pulse interacting with a Doppler broadened gas of two level atoms, the evolution equations that describe the forward and backward propagating modes of the optical coherence $\phi_{\mathrm{b\,f}}^{(j)}$ of each

atom j and the field amplitude $\Omega_{\mathrm{b\,f}}$ read:

$$\frac{\partial}{\partial t}\phi_{\mathrm{b\,f}}^{(j)} = i\delta_j \phi_{\mathrm{b\,f}}^{(j)} - i\Omega_{\mathrm{b\,f}} \tag{1.11a}$$

$$\left(\frac{\partial}{\partial t} \pm c\frac{\partial}{\partial z}\right)\Omega_{\mathrm{b\,f}} = i\eta \int_{-}^{+} \phi_{\mathrm{b\,f}}^{(j)} G(\delta_j) d\delta_j \tag{1.11b}$$

where the subindex b (f) and the sign $-$ $(+)$ in Eqs. (1.11), refer to the backward (forward) mode, δ_j is the detuning, $G(\delta_j)$ is the detuning distribution of the atoms, c is the speed of light in the vacuum, $\eta = g^2 N d$ with $g^2 = \ _0\ 2\ _0 V$ being the coupling constant, $\ _0$ the atomic transition frequency, $\ _0$ the vacuum permittivity, N the number of atoms in the quantization volume V, and d the electric dipole moment. Moreover, we have used the weak field approximation, *i.e.*, that the population, initially in level 1 , does not evolve in time. We note from these equations that the backward propagating modes are identical to the time reversed form of the forward propagating ones, provided a sign change in the detuning and field amplitudes is applied. This time reversal symmetry ensures that the backwards emerging photon is a perfect time reversed copy of the incident one, provided the optical depth is large enough to completely absorb the initial photon. This sign change in the field amplitudes corresponds to performing a phase matching operation, for instance via the two counterpropagating ν pulses, or more generally by applying a phase shift e^{-2ikz_j} to all the atoms. Later on, the idea reported in Ref. [105] was extended to solid state materials, allowing for large storage times [106, 107] and for the artificial creation of controlled reversible inhomogeneous broadening (CRIB) [108, 109]. The creation of this artificial broadening is sketched in Fig. 1.6. First, (a) consider a material with an intrinsic inhomogeneously broadened spectrum. (b) Next, a single absorption spectral line is isolated using optical pumping techniques, and then (c) it is artificially broadened with external electric or magnetic field gradients. (d) The change of sign of the detuning can be performed by changing the polarity of the device that generates the fields.

As pointed out in Eqs. (1.11), the time reversal symmetry arising from the phase matching and the sign change of the detuning provides, for large enough optical depths, a reemission in the backward direction with a 100% efficiency. In this context, several proposals have analyzed the performance of the memory for situations in which the phase matching operation is not applied and for limited optical depths [27, 110]. In this case, the absence of phase matching leads to the

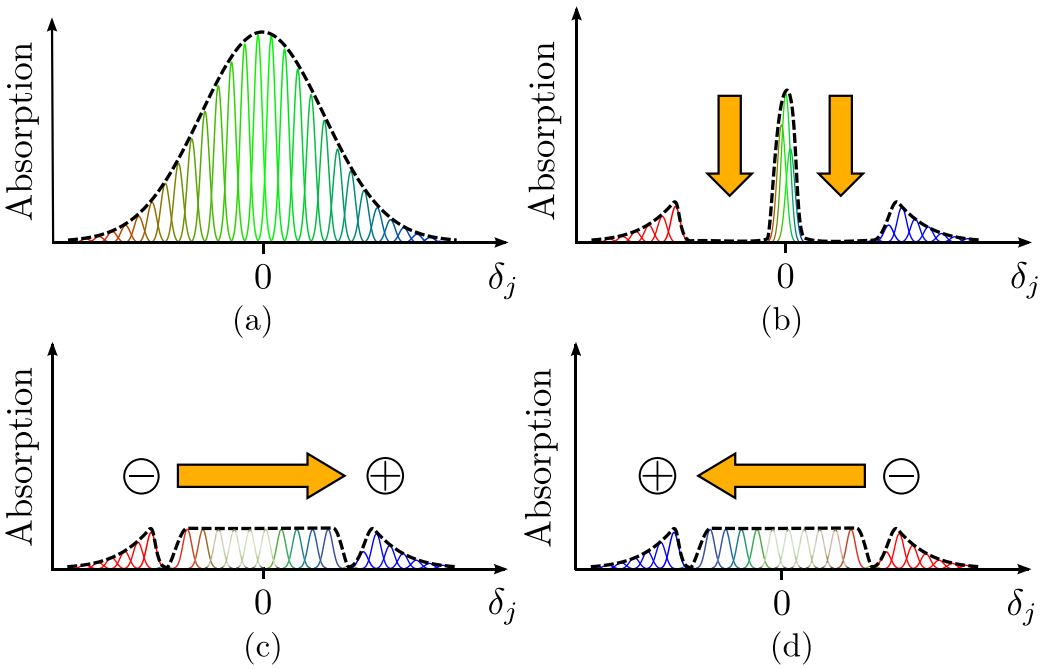

Figure 1.6: Protocol to artificially create a controlled reversible inhomogeneous broadening (CRIB). (a) Take a material with a large natural inhomogeneous linewidth. (b) Isolate a narrow absorption line with optical pumping techniques. (c) Broaden the single line by using external field gradients. (d) Change the polarity of the fields to reverse the detuning.

reemission in the forward direction, instead of in the backward. Moreover, if the inhomogeneous broadening is created transversal to the light propagation direction, the reabsorption of the light limits the memory efficiency to a 54% [27, 110]. Alternatively, if the broadening is distributed in the same direction as the light propagation, the reabsorption of the emmited light is avoided, and the efficiency can be ideally 100%, for large optical depths. The later configuration is usually refered as longitudinal CRIB or gradient echo memory (GEM) [39] and has been experimentally demonstrated in solid state systems [111, 112], allowing the possibility to create highly efficient quantum memories [29] and to store single photons in the telecommunications domain [48, 113]. In addition, the CRIB technique has been considered recently for the storage of orthogonal polarization components of weak light pulses [114–116].

The CRIB techniques have been combined with direct Raman transfer to an extra metastable state of a Λ configuration [40, 117–120]. This approach is known as Raman echo quantum memory (REQM) or Λ-GEM, for the longitudinal in-

homogeneous broadening case. The first experiments of Λ-GEM were performed using warm atomic vapors [117, 118], and efficiencies up to 41% were demonstrated. Also, the possibility to work as a sequencer of multiple stored pulses [40], and the implementation of this technique in cold atomic ensembles [119] has been proposed.

Atomic frequency combs (AFC)

Instead of inverting the sign of the detunings, the other possibility to induce the atomic rephasing required in Eq. (1.10) to reemit the light pulse, is to use a detuning distribution with a comb profile, as the one shown in Fig. 1.7. In this approach, the atomic frequency distribution has absorption lines of width given by the homogeneous decay rate γ, spaced by multiples of a fixed peak separation Δ. This kind of distribution can be created for instance by frequency selective optical pumping [121, 122] by modulating the amplitude or the frequency of the pump field. With such a structure, the phase of all the atoms in the comb-like distribution, $e^{i\delta_j t}$ in Eq. (1.10), will be equal at times multiples of $T = 2\pi/\Delta$ [123]. At those times, an automatic reemission of the stored light will occur in the backward or forward direction, depending on whether the phase matching condition is applied or not, respectively. As in the CRIB proposal, the forward reemission efficiency will be limited by the reabsorption of the medium to 54%.

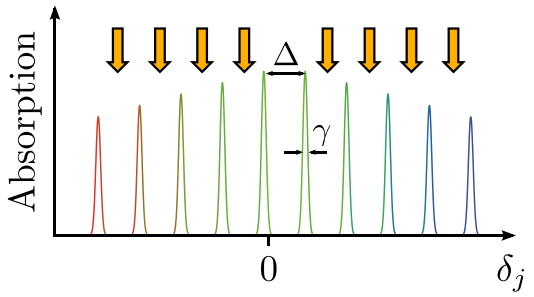

Figure 1.7: Profile of an atomic frequency comb with peak separation Δ and peak width γ created by optical pumping (represented with vertical orange arrows) at certain frequencies.

This approach comes from the idea that a photon echo can be stimulated from accumulated frequency gratings [121, 124], and compared to CRIB, it has the advantage of making better use of the available optical depth because fewer atoms are needed to be removed from the spectral absorption profile through optical pumping (see differences between Fig. 1.6 and Fig. 1.7). Moreover, while

the CRIB multimode capacity increases linearly with the absorption depth, in the AFC protocol it depends only on the number of peaks in the comb [36, 41, 42] leading to an almost unlimited number of possible modes to store [41, 42]. An essential feature of the spectral profile for the performance of the memory is the finesse of the comb, defined as $\mathcal{F} = \Delta\ \gamma$. The higher the finesse, the narrower the peaks of the comb compared to their separation. To avoid having atoms with non-desired frequencies, and hence to have a perfect rephasing, one needs a high finesse of the comb (the ideal case would be having Dirac delta-like peaks). However, a high finesse implies that more atoms need to be removed from the original spectrum profile and therefore the optical depth is dramatically reduced, limiting the absorption efficiency. Therefore, a compromise between the finesse of the comb and the optical depth is needed [36]. One of the main disadvantages of this scheme is that the emission time is fixed by the peak separation, limiting its on-demand possibilities. However, this drawback has been surpassed recently using a pair of ν pulses to transfer back and forth the excited optical coherence to the long-lived ground-state coherence of a Λ system [125]. Later, an improvement of the transfer technique, using chirped control fields, has been also proposed [126], and optimal comb structures investigated [127, 128]. Recent advances in quantum memories based on AFC include storage of photons at the telecommunication wavelengths [113], the possibility to entangle a single photon with a collective atomic excitation [49, 129] at record bandwidths [46], to entangle two separate crystals [130], and to store polarization encoded qubits [131 133].

1.3.7 Single atom in a cavity

Most of the previously discussed quantum memory proposals rely on information storage in collective excitations. However, very recently, a novel approach consisting in a quantum memory formed by a single atom in a cavity was proposed [31]. This scheme is a first step towards a light-matter interface at the truly quantum level, *i.e.*, mapping quantum information between flying and stationary single qubits. This single particle approach allows to herald the successful storage of a photon [134], and the in situ manipulation of the stored qubit. However, the interchange of quantum information between single photons and single atoms is a task difficult to accomplish, due to the weak interaction strength. A possible approach to achieve strong enough couplings is to use an optical cavity with a single atom trapped inside. In this context, the mapping of quantum information from a single atom onto a photon has been achieved [135], whereas the inverse process

has been addressed by controlling the pulse transmission through the cavity either using EIT [136, 137] or storing part of the pulse in the atom and releasing it [138].

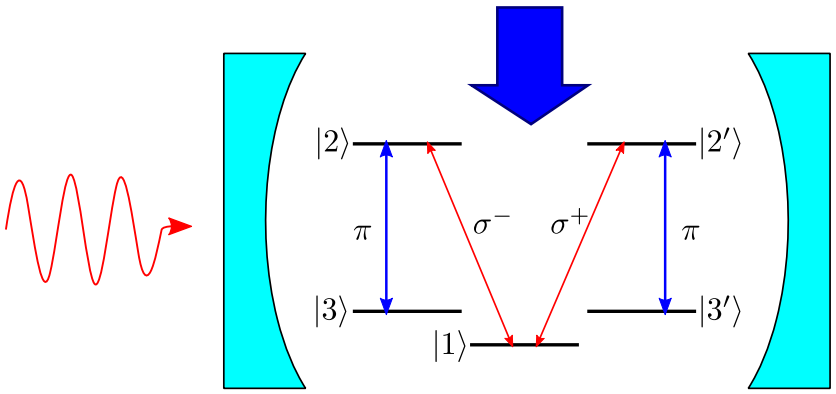

Figure 1.8: Scheme of the single atom quantum memory [31] proposal. A single atom in a cavity interacts with a strong control ν-polarized field and a weak coherent pulse, in an arbitrary polarization state, entering the cavity. The polarization components of the weak pulse ϕ^- and ϕ^+ (in red) couple the transitions $1 - 2$ and $1 - 2$, respectively, while the control field (in blue) couple simultaneously the transitions $2 - 3$ and $2 - 3$. When the weak pulse arrives the control field is turned off, producing a STIRAP transfer to levels 3 and 3 . After a time, the turning on of the control field transfers back the population to level 1 and a single photon with the same polarization as the input pulse is emitted.

One step further, the coherent mapping of polarization encoded quantum information from light into a single atom in a cavity and back to light has been achieved by Specht *et al.* [31]. In this proposal, sketched in Fig. 1.8, a single ^{87}Rb atom with five relevant energy levels in a M-configuration is trapped into a high finesse optical cavity. The atomic population is prepared initially in the ground state 1 , and a control ν polarized laser, perpendicular to the cavity, couples to the outer transitions, $2 - 3$ and $2 - 3$, of the M configuration. Then, a weak coherent pulse in an arbitrary polarization state (defined by a superposition of ϕ^+ and ϕ^-) is sent to the atom through one of the mirrors of the cavity, which has high transmission. Each of the two circular polarizations of the probe pulse is coupled with one of the inner transitions of the atom, $1 - 2$ and $1 - 2$, thus forming a V-type scheme. Simultaneously with the arrival of the probe, the control laser is turned off. This produces a cavity-mediated stimulated Raman adiabatic passage (STIRAP) which transfers the population from the state 1 to the next ground states 3 and 3 , and creates a spin coherence between them. After a certain storage time, turning on the control field converts the spin coher-

ence into a single photon with ideally the same polarization state as the initial weak pulse. This approach for polarization qubit quantum memory was tested using quantum state tomography, which resulted in fidelities of 93%, efficiencies around 10%, and storage times close to 200 μs.

1.3.8 Summary

To conclude, we present here a summary of the main approaches to perform quantum memories (Table 1.1), enumerating both the technique (1st column) and the physical system (2nd column), as well as the values for the figures of merit achieved using the different methods (columns 3rd to 7th).

We observe that each quantum memory approach has its own advantages. For instance, while the EIT technique offers the record storage time (2.3 s [34]), the group of photon echo techniques present in general larger storage bandwidths and efficiencies, and have been demonstrated in the telecommunications range. Within photon echo, the GEM approach presents acceptable efficiencies and bandwidths ($\sim$ 70% [29]), while the multimode capacity is the strong point of the AFC proposal (up to 1060 modes in Ref. [42]). Moreover, a record bandwidth of 5 GHz has been reported recently [46] using a rare-earth ion doped waveguide as a storage medium. Concerning the Raman memory, the bandwidth available is only limited by the spectral characteristics of the strong pump field, thus considerably broadband photons have been stored used this technique [47]. Also recently, the Raman memory has been used to store a single photon in a cold atomic ensamble, placed in a cavity, with high fidelity and efficiency, during a relatively long time [30]. Regarding the recent proposal based on a single atom in a cavity [31], acceptable values for the main figures of merit have been obtained, which serves as a proof of principle for this promising approach.

We conclude from this table that, although important benchmarks have been achieved, each technique provides satisfactory values of only one or two figures of merit. Note for instance that in most cases the memory efficiency is compromised with short storage times. In this line, an important step towards a versatile quantum memory is the experiment reported in Ref. [30], in which suitable values for both the efficiency and the storage time have been achieved.

QM	Material	Fidelity (%)	Efficiency (%)	Bandwidth (MHz)	Storage Time (μs)	Number of modes	Observations	Ref.
EIT	Dopped solid	-	1	2.5×10^{-3}	2.3×10^{6}	-	Record storage time	[34]
	Warm vapour	-	-	$\sim 0.4 - 0.6$	50-200	-	First demonstration	[66]
		-	40	~ 0.1	400	-	Record EIT efficiency	[73]
	Cold atoms	-	-	~ 1	1×10^{3}	-	First demonstration	[65]
		High	17	~ 35	~ 1	-	Polarization qubit	[76]
		> 90	38	-	0.2	-	4 memories entanglement	[78]
		98	~ 15	-	1	4	Biphoton storage	[44]
GEM	Dopped solid	-	69	~ 10	1.3	-	Record GEM efficiency	[29]
		-	1	2	6	-	First GEM demonstration	[111]
		-	~ 0.2	~ 60	0.3	-	Telecomm. range	[48]
	Warm vapour	-	~ 5	1	10 - 80	7	Pulse sequencerΛ-GEM	[40]
		-	~ 1	-	2.5	-	First demonstration Λ-GEM	[117]
AFC	Dopped solid	97.5	0.5	~ 200	0.25	4	First demonstration	[123]
		95	0.2	5000	7×10^{-3}	-	Record bandwidth	[46]
		-	$\sim 5.5 - 0.25$	100	$\sim 0.25 - 2.5$	64	High temporal multimode	[41]
		-	35	~ 30	0.8	-	Record AFC efficiency	[139]
		-	1	930	1.6	1060	Record temporal multimode	[42]
		> 99	< 14	350	0.5	-	Polarization qubit storage	[131–133]
Raman	Warm vapour	-	15	~ 1500	12.5×10^{-3}	-	Record Raman bandwidth	[47]
	Cold atoms	-	1.1	-	$> 6 \times 10^{3}$	-	Record Raman storage time	[92]
		High	73	-	3.2×10^{3}	-	High efficiency-storage time	[30]
Single atom		93	9.3	Several	180	-	First demonstration	[31]

Table 1.1: Summary of the main figures of merit and techniques to perform a quantum memory.

2

Quantum memory for polarization single photon qubits in three-level atoms

In this Chapter, based on the works published in Refs. [115, 116], we propose two different approaches to implement quantum memories for single photon polarization qubits, *i.e.*, single photons in an arbitrary superposition of two orthogonal polarizations, using both in V- and in Λ-type three-level atoms. First, in Section 2.1 we review the state-of-the-art of polarization qubit quantum memories and discuss their interest. Next, in Section 2.2, we introduce the physical system under investigation, consisting of an ensemble of inhomogeneously broadened three-level atoms (either in a V or in a Λ configuration) interacting with two-polarization components of a single weak pulse coupled to each of the optical transitions, and we derive the evolution equations that govern its dynamics. Under the weak-field approximation, the equations for the forward and backward propagating modes of the atomic polarization and the field components are linear, which means that they can be used to describe the single photon case. Moreover, the time reversal symmetry of the evolution equations allow to use the controlled reversible inhomogeneous broadening technique (CRIB) [108, 109, 111], discussed in Subsection 1.3.6, to implement a quantum memory.

On the one hand, in Section 2.3, we focus into the V-type configuration for the three-level atoms, and we theoretically show the possibility to store and retrieve the weak light (or the single photon) pulse interacting with the two optical transitions of the system. In most approaches the storage of the polarization qubit is achieved by using two spatially separated two-level media quantum memories. In contrast, this scheme implements a quantum memory for polarization qubits with-

out the need of spatially splitting the path for the light. For this reason our scheme offers the advantage of experimental compactness and allows to overcome the limitations due to mismatching and unequal efficiencies that can arise in spatially separated memories. We also analyze different phase noise mechanisms affecting the atomic transitions due to, for instance, the transfer of the stored excitation back and forth from the excited state to a metastable one to enlarge and control the storage time, or an imperfect isolation of the atomic ensemble from external electric or magnetic fields.

On the other hand, in Section 2.4, we consider Λ-type three-level atoms, prepared in a coherent superposition of the two ground states, *i.e.*, the so called phaseonium preparation [140]. Then, we address the propagation of a single photon pulse with two polarization components, *i.e.*, a polarization qubit, in this three-level medium, and combine some of the non-trivial propagation effects characteristic for this kind of coherently prepared systems with the controlled reversible inhomogeneous broadening technique. As a result of our investigation, we propose different quantum information processing applications, such as a protocol for polarization qubit filtering and sieving, as well as a tunable polarization beam splitter. Moreover, we show that, by imposing a spatial variation of the atomic coherence phase, an efficient quantum memory for the incident polarization qubit can be also implemented in Λ-type three-level systems.

Finally, in Section 2.5 we briefly discuss the feasibility of the two proposed methods to implement polarization qubits in real systems, while in Section 2.6 we summarize the results and present the conclusions.

2.1 Introduction

The realization of high efficientand high fidelity quantum memories is an ambitious goal that has motivated a considerable worldwide activity [30, 31, 44, 46, 47, 49, 85, 86, 92, 129, 131 133, 141 143]. In particular, optical quantum memories are essential for quantum information processing: they play a central role in quantum computation with linear optics [12, 13] and, more generally, in quantum networks [144]. Specifically, optical quantum communication suffers from degradation of information along transmission at large distances. To cope with this, advanced strategies have been proposed requiring the use of quantum repeaters of which quantum memories are the core ingredient [4, 5, 14, 33, 72, 98]. In quantum communication with photons, logical qubits can be encoded in several ways,

for example via polarization, time-bin, path, phase, or photon-number encodings. Concerning polarization, the logical 0 and 1 quantum states correspond to two orthogonal polarization degrees of freedom, for example, left- and right- circular polarizations. Many quantum information processes and sources of photon states are based on the polarization degree of freedom, showing a high degree of interferometric stability and experimental compactness. Thus, it is on the storage and retrieval of polarization qubits that we will focus on this chapter.

Up to now, polarization-qubit memories have been experimentally realized mainly in cold atomic ensembles and atomic vapors [75, 76, 78, 96, 99, 100], though storage of polarization states of light has also been reported recently in solid-state crystals [131 133]. In these experiments, polarization encoding is first transformed into path encoding[1] and then stored into two spatially distinguishable ensembles (actually, two different memories). Retrieval is eventually performed by mixing again the output pulses, thus transforming back to the original polarization encoding. Those realizations are attractive, however are susceptible from several practical drawbacks due to the storing of each polarization component in a different region. As a matter of fact, in order to preserve the original input quantum state, the two retrieved beams must be indistinguishable when mixed back again, apart from what concerns their polarization. In particular, they must occupy the same spatial and temporal mode, implying perfect matching at the mixing stage. In addition, the efficiency of the two memories and their environmental conditions must be the same, otherwise the two polarization components of the original beam would be retrieved in an unbalanced fashion. Such necessary conditions require extra efforts from the experimental point of view [145]. Recently, the storage of polarization qubits without spatially splitting the input photon has been addressed [31, 114]. In Ref. [31] the qubit is stored in a single atom, with five relevant energy levels in an M-type configuration[2], trapped in a high finesse cavity, whereas in Ref. [114] a dense ensemble of four-level atoms in a tripod configuration is investigated for storage and retrieval of polarization qubits.

We show here that a quantum memory for polarization qubits can be implemented also in a three-level system without the extra step of splitting spatially the input state and, therefore, storing both polarization components in the same spatial region. In particular, we base our analysis in the controlled reversible inho-

[1]Strictly speaking, in Refs. [131, 133] there is no path separation, but the two memories are placed one behind the other, thus each crystal absorbs a different polarization component.

[2]Note that the use of this scheme was previously pointed out in Ref. [146]

mogeneous broadening (CRIB) technique [108, 109], discussed in Subsection 1.3.6. CRIB has been developed especially for the storage of time-bin qubits, being particularly suited for broad-band pulses. However, we will show in this Chapter that photon echo quantum memories could also offer a compact resource to store and retrieve polarization qubits. Specifically, we will consider the transverse CRIB technique (see Subsection 1.3.6), although most of the results shown here could be easily extended to the longitudinal CRIB, or gradient echo memory, case [111].

2.2 Controlled reversible inhomogeneous broadening (CRIB) in three-level systems

In most of the previous works concerning CRIB, two-level systems have been considered, apart from the mentioned auxiliary third level used only to perform the phase-matching operation and increase the storage time. Here we extend the CRIB approach to media composed of three-level atoms interacting with a weak pulse with two orthogonal polarization components.

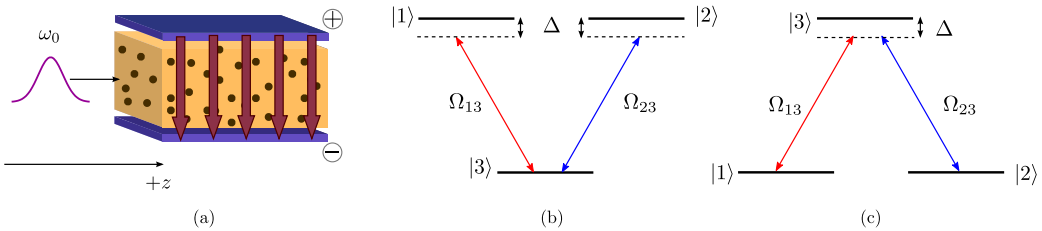

Figure 2.1: (a) Physical system under investigation: a single pulse with central frequency $_0$ and two circular polarization components enters a medium with transverse inhomogeneous broadening. The three-level atoms of the medium are in a (b) V-type or (c) Λ-type configuration. The left- (right-) circularly polarized component of the incident pulse couples to transition $3 - 2$ ($3 - 1$) in the V-scheme and to $3 - 1$ ($3 - 2$) in the Λ-scheme, Ω_{13} and Ω_{23} denote the Rabi frequencies of the components coupled to the corresponding transitions and Δ is the one photon detuning. We assume degenerate 1 and 2 levels, so the polarization components are in two-photon resonance.

The physical system under investigation is sketched in Fig. 2.1(a), and consists of a single pulse, with central frequency $_0$ and two orthogonal polarization components (for definiteness we assume left and right circular polarizations) propagating in the $+z$ direction, and interacting with a medium in which an artificial transverse inhomogeneous broadening, much wider than the spectral width of the

pulse, has been created. This artificial broadening can be implemented, for instance, via Stark shift of the atom levels by an externally applied electric field. For the atoms of the medium, we consider two possible energy level configurations, either V [Fig. 2.1(b)] or Λ [Fig. 2.1(c)] schemes. Since the evolution equations for both configurations are formally the same, we present in what follows a common derivation for the two of them. In the two configurations, the each polarization component of the field interacts with on of the optical allowed transitions, for which we assume the same nominal frequencies, and that the two-photon resonance condition is fulfilled for all atoms within the inhomogeneously broadened profile. In this situation, the evolution of a single Λ-type three level atom can be described, in the rotating wave and electric dipole approximations, by the following density matrix equations:

$$\frac{}{t}\phi_{11}(z\ t) = i\phi_{13}(z\ t)\Omega^{*}_{13}(z\ t) + \text{c c} \tag{2.1a}$$

$$\frac{}{t}\phi_{22}(z\ t) = i\phi_{23}(z\ t)\Omega^{*}_{23}(z\ t) + \text{c c} \tag{2.1b}$$

$$\frac{}{t}\phi_{12}(z\ t) = i\phi_{13}(z\ t \quad {}_{31})\Omega^{*}_{23}(z\ t) - i\phi_{32}(z\ t)\Omega_{13}(z\ t) \tag{2.1c}$$

$$\begin{aligned}\frac{}{t}\phi_{13}(z\ t) =& i\phi_{12}(z\ t)\Omega_{23}(z\ t) - i\ {}_{31}\phi_{13}(z\ t) \\ & - i\left[\phi_{33}(z\ t) - \phi_{11}(z\ t)\right]\Omega_{13}(z\ t)\end{aligned} \tag{2.1d}$$

$$\begin{aligned}\frac{}{t}\phi_{23}(z\ t) =& i\phi_{21}(z\ t)\Omega_{13}(z\ t) - i\ {}_{32}\phi_{23}(z\ t) \\ & - i\left[\phi_{33}(z\ t) - \phi_{22}(z\ t)\right]\Omega_{23}(z\ t)\end{aligned} \tag{2.1e}$$

where ϕ_{ii} is the population of level i , ϕ_{ij} is the atomic coherence between levels i and j , $\Omega_{ij} = \left(d_{ij}\cdot E_{ij}\right)$ is the Rabi frequency with E_{ij} being the slowly varying electric field amplitude of the light component coupled with transition $i - j$, d_{ij} is the dipole moment of the corresponding transition, is the reduced Planck constant, and ${}_{ji} = {}_{j} - {}_{i}$ is the transition frequency between levels j and i . The evolution equations for the V-type configuration can be obtained from Eqs. (2.1) by substituting the Rabi frequencies by their complex conjugates. Note that we consider a closed atomic system satisfying $\phi_{11} + \phi_{22} + \phi_{33} = 1$. Moreover, for simplicity, we have not included any incoherent decay term into Eqs. (2.1), since we assume that the lifetimes of the excited level and of the ground state coherence are much larger than the whole duration of the interaction process [27].

In order to solve analytically the evolution equations of the system we gen-

eralize the treatment done in Ref. [27], where the transition operators and the field amplitudes associated to each dipole transition are split into the forward and backward modes, denoted by the superscripts f and b, respectively:

$$\phi_{\mu\rho}(z\ t) = \phi^{\mathrm{f}}_{\mu\rho}(z\ t)e^{\pm i(\ _0 t - k_0 z)} + \phi^{\mathrm{b}}_{\mu\rho}(z\ t)e^{\pm i(\ _0 t + k_0 z)} \tag{2.2a}$$

$$\Omega_{\mu\rho}(z\ t) = \Omega^{\mathrm{f}}_{\mu\rho}(z\ t)e^{\pm i(\ _0 t - k_0 z)} + \Omega^{\mathrm{b}}_{\mu\rho}(z\ t)e^{\pm i(\ _0 t + k_0 z)} \tag{2.2b}$$

where, from now on, we set $\varphi = 3$, $\mu\ \nu = 1\ 2$ and $\mu = \nu$. The signs + and − in the exponents correspond to the case of V- and Λ-schemes, respectively, $\ _0$ is the central frequency of the pulse and k_0 the corresponding wavenumber. Since the interaction involves weak pulses, one can neglect [108, 109, 111] the temporal variations in the level populations as well as in the coherence ϕ_{12}. The validity of these approximations is checked and confirmed in Subsections 2.3.5 and 2.4.4 via numerical analysis of the full set of Bloch Eqs. (2.1). Using the forward/backward mode decomposition [Eqs. (2.2)] and the weak field approximation, outlined just above, Eqs. (2.1) are simplified as follows:

$$\frac{}{t}\phi^{\mathrm{b\,f}}_{\mu\rho}(z\ t\ \Delta) = i\Delta\phi^{\mathrm{b\,f}}_{\mu\rho}(z\ t\ \Delta) - i(\phi_{\rho\rho} - \phi_{\mu\mu})\Omega^{\mathrm{b\,f}}_{\mu\rho}(z\ t) + i\phi_{\mu\nu}\Omega^{\mathrm{b\,f}}_{\nu\rho}(z\ t) \tag{2.3}$$

where we have made explicit the dependence of the optical coherence on the detuning Δ, defined as $\Delta = \ _0 - \ _{\rho\mu}$ for the Λ-scheme and $\Delta = \ _{\mu\rho} - \ _0$ for the V-scheme. Note that the evolution equations for each optical transition are in general coupled through the two-photon coherence $\phi_{\mu\nu}$.

On the other hand, the propagation of the forward and backward modes of the light, in a reference frame moving with the pulses ($z \quad z$ and $t \quad t \mp z\ c$), can be described by the following equations:

$$\frac{}{z}\Omega^{\mathrm{b\,f}}_{\mu\rho}(z\ t) = \mp i\eta_{\mu\rho}\int_{-} \quad G_{\rho\mu}(\Delta)\,\phi^{\mathrm{b\,f}}_{\mu\rho}(z\ t\ \Delta)d\Delta \tag{2.4}$$

where + (−) refers to backward (forward) modes, $G_{\rho\mu}(\Delta)$ is the inhomogeneous frequency distribution of atoms of the corresponding transition; $\eta_{\mu\rho} = g^2 N d^2_{\mu\rho} \quad c$ with $g^2 = \ _0\ 2\ _0 V$ being the coupling constant; $\ _0$ is the vacuum electric permittivity, N is the number of atoms in the quantization volume V, and c is the speed of light in vacuum. It is worth noting that, although the treatment is performed in the semiclassical formalism, the linearity of the equations ensure the validity of this model also at the single photon level. Thus, in what follows, both the

atomic coherences and the fields can be interpreted as classical amplitudes as well as quantum operators.

From Eqs. (2.3)-(2.4), we note that the time reversed ($t \quad -t$) equations for the forward propagating modes are equal to the backward ones under a sign change in the detunings and in the field amplitudes. As we have discussed after Eqs. (1.11), this symmetry in the optical-Bloch equations is indeed the basis for the CRIB technique. Therefore, as described in Subsection 1.3.6, once the forward propagating input light pulse has been completely absorbed, in order to retrieve the pulse as a time reversed copy of itself, we need to reverse the detuning ($\Delta \quad -\Delta$). This reversing operation can be achieved, for instance, by changing the polarity of the device that creates the inhomogeneous broadening. At the same time, one has to apply a position dependent phase matching operation to transform the forward components of the atomic excitations into backward components, so that the retrieved pulse propagates in the backward direction. This phase change can be performed by transferring the atomic coherences back and forth to an auxiliary metastable state [108, 111, 126] which also allows for longer storage times [34, 106, 107]. If the phase matching is not performed, the atoms will reemit in the forward direction, process that is described by the forward modes of Eqs. (2.3) and (2.4).

2.3 Optical quantum memory for polarization qubits with V-type three-level atoms

In this Section, we consider the case in which the atoms of the memory have a V-type energy level configuration [see Fig. 2.1(b)]. For this situation, we analytically solve Eqs. (2.3) and (2.4), obtained under the weak input pulse approximation, considering that the atomic population is initially in the ground state, 3 . Moreover, we will consider the effect, in the efficiency and the fidelity of the memory, of a phase change in the atomic coherence after the input pulse has been absorbed, as well as the influence of an inhomogeneous phase noise in the rephasing of the atoms at the retrieval stage. For each of the two field components involved in the process, the efficiency is defined as:

$$\mathrm{Eff}_{\mu\rho}^{\mathrm{b\,f}} = \frac{\int_{-} \left| \Omega_{\mu\rho}^{\mathrm{b\,f}}(z = z_{\mathrm{out}} \quad) \right|^2 d}{\int_{-} \left| \Omega_{\mu\rho}^{\mathrm{in}}(z = 0 \quad) \right|^2 d} \tag{2.5}$$

where the superscripts f and b refer to the forward and backward protocols, and $\Omega^{\rm in}_{\mu\rho}(0\quad)$ and $\Omega^{\rm b\,f}_{\mu\rho}(z_{\rm out}\quad)$ denote the temporal Fourier transforms of the input and output field components, respectively. For the backward and forward retrieval schemes in a medium with length L, the output components are evaluated at the medium surfaces $z_{\rm out} = 0$ and $z_{\rm out} = L$, respectively. Eq. (2.5) addresses the energetic balance of the storage and retrieval processes, that is to say, the storage and retrieval of each component of the field independently from the other one. However, when considering the storage of quantum fields, it is of relevance to focus on the phase between the two polarization components of the retrieved qubit by comparing it with the phase of the input qubit. Since we are interested in the case of initial pure states, the fidelity is defined as the overlap between the initial state $_{\rm in}$ and the retrieved state, which in general, could be pure or mixed:

$$\mathrm{F}^{\rm b\,f} = \quad {}_{\rm in} \quad {}^{\rm b\,f}_{\rm out} \quad {}_{\rm in} \tag{2.6}$$

where $^{\rm b\,f}_{\rm out}$ is the density matrix of the backward or forward retrieved qubits. Note that for those cases in which the quantum memory is perfectly efficient the retrieved state is pure. This is due to the unitarity of the dynamics and the fact that the medium and the fields end up in a factorized state. On the contrary, for a non-unit efficiency, for instance for finite optical depths, where part of the incident light is lost, the output state will be mixed.

2.3.1 Polarization qubit storage

As said in the discussion before Eqs. (2.3), for a weak input pulse the dynamical evolution of the level populations can be neglected, and therefore, since the initial population is assumed to be in the ground level 3 , $\phi_{33} = 1$, one can assume that the population of the excited levels as well as the coherence between them remains negligible during the whole storage and retrieval process, *i.e.*, $\phi_{11} = \phi_{22} = \phi_{12} \quad 0$. In such case the evolution of the two components of the pulse are uncoupled from each other and Eqs. (2.3) can be solved for each field component separately:

$$\frac{}{t}\phi^{\rm b\,f}_{\mu\rho}(z\ t\ \Delta) = i\Delta\phi^{\rm b\,f}_{\mu\rho}(z\ t\ \Delta) - i\Omega^{\rm b\,f}_{\mu\rho}(z\ t) \tag{2.7}$$

In other words, the system turns out to be equivalent to two independent two-level media. Thus, the standard treatment of CRIB in two-level media can be applied: each pulse component is absorbed by the transition it is coupled with, and

the information is stored in the respective optical atomic coherence. Afterwards, each pulse can be retrieved as in standard CRIB, either in the backward or in the forward direction. Thus, this protocol avoids the need of any active spatial separation of the pulse components to store them. Therefore, the use of CRIB in V-type three level atoms does not suffer from detrimental effects due to the mismatch in spatially separated memories. For later purposes, let us now present the analytical solution for the field components in all the stages of the CRIB protocol following the lines of Ref. [27].

2.3.2 Absorption of the field components

The solution for the propagation of the incident field components can be analytically obtained by inserting the solutions of Eqs. (2.7) (for the forward modes `f), with the initial conditions $\phi^{\mathrm{f}}_{\mu\rho}(z\ t = -\quad \Delta) = 0$, into Eqs. (2.4). Using the notation introduced in Eq. (2.5) and Fourier transforming the result, one obtains:

$$\frac{}{z}\Omega^{\mathrm{in}}_{\mu\rho}(z\quad) = -\eta_{\mu\rho}H_{\mu\rho}(\ \ )\Omega^{\mathrm{in}}_{\mu\rho}(z\quad) \tag{2.8}$$

where is the Fourier variable, and we have defined

$$H_{\mu\rho}(\ \ ) = \int_{-}\quad G_{\mu\rho}(\Delta)\int_{0}\quad e^{i\ \ \tau}e^{i\Delta\tau}d\vec{\ }d\Delta \tag{2.9}$$

To get analytical insight, we consider symmetric transitions, that is to say, equal electric dipoles, $\left|d_{13}\right| = \left|d_{23}\right| = d$, and inhomogeneous broadening distributions, $G_{13}(\Delta) = G_{23}(\Delta) = G(\Delta)$. Under these assumptions it follows that $H_{13}(\ \ ) = H_{23}(\ \ ) = H(\ \ )$ and $\eta_{13} = \eta_{23} = \eta$. Therefore the solutions of Eqs. (2.8) read:

$$\Omega^{\mathrm{in}}_{\mu\rho}(z\quad) = \Omega^{\mathrm{in}}_{\mu\rho}(0\quad)\exp\left[-\frac{\alpha(\ \ )z}{2}\right] \tag{2.10}$$

with $\Omega^{\mathrm{in}}_{\mu\rho}(0\quad)$ the Fourier transformed Rabi frequency of the incident polarization components at $z = 0$, and $\alpha(\ \ ) = \eta H(\ \ )$ the absorption coefficient, which determines the optical depth of the atomic ensemble: $\alpha(\ \ )L$, with L the length of the medium. This equation describes the absorption of each frequency component of the incoming field, and it shows that, for large enough optical depths, complete absorption of the two field components can be obtained.

2.3.3 Backward and forward retrieval

We study now the propagation of the retrieved light pulse in backward and forward directions caused by the sign change of the detunings, after the absorption stage, at time $t = 0$. Note that for the backward propagating case, a phase matching operation is also needed for the retrieval, which corresponds to a sign change in the field amplitudes. Therefore, by changing $\Delta \quad -\Delta$ and $\Omega^{\mathrm{b\,f}}_{\mu\rho} \quad -\Omega^{\mathrm{b\,f}}_{\mu\rho}$ in Eqs. (2.7), for the backward case, and only $\Delta \quad -\Delta$ for the forward retrieval, Eqs. (2.4) and (2.7) can be solved following the same method as in the absorption stage. Here, we use the boundary conditions $\Omega^{\mathrm{f}}_{\mu\rho}(0 \quad) = 0$ and $\Omega^{\mathrm{b}}_{\mu\rho}(L \quad) = 0$ for the forward and backward reemission processes, respectively, and the initial condition $\phi^{\mathrm{b\,f}}_{\mu\rho}(z \;\; t = 0 \;\; -\Delta) = \phi^{\mathrm{in}}_{\mu\rho}(z \;\; t = 0 \;\; \Delta)$. By defining

$$F_{\mu\rho}(\;\;) = \int_{-}^{+} \;\; G_{\mu\rho}(-\Delta) \int_{0} \;\; e^{i \;\; \tau} e^{-i\Delta\tau} d\vec{\tau} d\Delta \tag{2.11a}$$

$$J_{\mu\rho}(\;\;) = \int_{-}^{+} \;\; G_{\mu\rho}(-\Delta) \int_{-}^{+} \;\; e^{i \;\; \tau} e^{-i\Delta\tau} d\vec{\tau} d\Delta \tag{2.11b}$$

the equations for the field components associated with each transition are:

$$\frac{}{z}\Omega^{\mathrm{b\,f}}_{\mu\rho}(z \quad) = \pm\eta_{\mu\rho} \;\; F_{\mu\rho}(\;\;)\Omega^{\mathrm{b\,f}}_{\mu\rho}(z \quad) + J_{\mu\rho}(\;\;)\Omega^{\mathrm{in}}_{\mu\rho}(z \;\; - \;\;) \tag{2.12}$$

with $+$ $(-)$ for the backward (forward) configuration. The analytical solutions for the output field components read:

$$\Omega^{\mathrm{b\,f}}_{\mu\rho}(z \quad) = -\gamma^{\mathrm{b\,f}}(\;\;)\Omega^{\mathrm{in}}_{\mu\rho}(0 \;\; - \;\;) \tag{2.13}$$

where we have assumed symmetric transitions and we have defined the backward and forward retrieval coefficients as

$$\gamma^{\mathrm{b}}(\;\;) = \frac{J(\;\;)}{F(\;\;) + H(-\;\;)} \left(1 - e^{-L\eta(F(\;\;)+H(-\;\;))}\right) \tag{2.14a}$$

$$\gamma^{\mathrm{f}}(\;\;) = z\eta J(\;\;) e^{-z\eta\frac{F(\omega)+H(-\omega)}{2}} \mathrm{sinhc}\left(z\eta\frac{F(\;\;) - H(-\;\;)}{2}\right) \tag{2.14b}$$

with $\mathrm{sinhc}(x) = \sinh(x) \;\; x$ denoting the hyperbolic sinus cardinal function. When the spectral bandwidth of the pulse is smaller than the one of the inhomogeneously broadened transitions, the functions defined in Eqs. (2.9) and (2.11) can be approximated as $F(\;\;) \quad H(-\;\;) \quad J(\;\;) \; 2 \quad \nu \; 2$. Therefore, the absorption

coefficient becomes $\alpha(\ ) = \eta J(\ )\quad \eta\nu$ and $\gamma^{\mathrm{b\,f}}(\ )$ simplify to:

$$\gamma^{\mathrm{b}}\quad (1 - e^{-\alpha L}) \tag{2.15a}$$

$$\gamma^{\mathrm{f}}\quad \alpha L e^{-\alpha L\ 2} \tag{2.15b}$$

with αL being the optical depth. Eqs. (2.13) show that for the backward scheme both field components are recovered up to the factor γ^{b}, which approaches unity for a large enough medium optical length. This result confirms that ideally both polarization components can be stored and recovered perfectly in the backward direction, thus permitting to build up a quantum memory for a polarization qubit. On the other hand, in the forward retrieval case the quantum memory yields a forward retrieval with a maximum achievable efficiency around 54% as expected from Ref. [27].

2.3.4 Effects of Phase noise

We consider now the effects of a specific variation in the phase of the atomic coherences, and its influence in the efficiency and fidelity of the memory. This is propaedeutic to the analysis of the role of the phase noise in the quantum memory, which will be the main goal of this Subsection.

Let us consider that, after the complete absorption of the field and before the reversing of the detuning, the phase difference between the atomic levels can be artificially engineered, for instance, by means of external electric or magnetic fields. The phase variation of the atomic coherences can be written, in the most general case, as:

$$\phi_{ij}\quad e^{i(\omega_i - \omega_j)}\phi_{ij} \tag{2.16}$$

with $i\ j = 1\ 2\ 3$. This phase variation affects the quantum memory protocol yielding an additional phase to the initial conditions used in the retrieval stage of the protocol. As a consequence, Eqs. (2.12) transform as follows:

$$\frac{}{z}\Omega^{\mathrm{b\,f}}_{\mu\rho}(z\quad) = \pm\eta_{\mu\rho}\ \ F_{\mu\rho}(\ )\Omega^{\mathrm{b\,f}}_{\mu\rho}(z\quad) + J_{\mu\rho}(\ )e^{i(\omega_\mu - \omega_\rho)}\Omega^{\mathrm{in}}_{\mu\rho}(z\ -\ ) \tag{2.17}$$

with $+$ $(-)$ corresponding to the backward (forward) retrieval protocol. The solutions of Eqs. (2.17) read:

$$\Omega^{\mathrm{b\,f}}_{\mu\rho}(z\quad) = -e^{i(\omega_\mu - \omega_\rho)}\gamma^{\mathrm{b\,f}}(\ )\Omega^{\mathrm{in}}_{\mu\rho}(0\ -\ ) \tag{2.18}$$

The above expression is identical to Eq. (2.13), apart from a phase factor. As a consequence, the retrieval efficiency for each field is the same as in the standard CRIB protocol. However the additional phase change introduced here affects the fidelity, defined in Eq. (2.6). Let us focus on the most interesting case corresponding to the backward retrieval, for which each component of the pulse can be recovered with unit efficiency for large optical depth media, *i.e.*, $\gamma^{\mathrm{b}}(\ ) \quad 1$. Consider a generic polarization qubit at the input:

$$_{\mathrm{in}} = a_L \ L \ + a_R \ R \tag{2.19}$$

where L and R denote a left- and right- circularly polarization states of a single photon, respectively. In the case of unit efficiency, the output backward field, Eqs. (2.18), would be:

$$^{\mathrm{b}}_{\mathrm{out}} = a_L e^{i\omega_L} \ L \ + a_R e^{i\omega_R} \ R \tag{2.20}$$

being $\pi_L = \pi_3 - \pi_1$ and $\pi_R = \pi_3 - \pi_2$. From Eq. (2.6), the corresponding input-output fidelity reads

$$\mathrm{F} = \left| \ a_L \ ^2 + e^{i\omega} \ a_R \ ^2 \right|^2 \tag{2.21}$$

with $\pi = \pi_1 - \pi_2$. Clearly, even if each component of the initial qubit is completely recovered, the additional phase accumulated in levels 1 and 2 degrades the fidelity. The latter is instead unaffected by a phase change in the lower level since, in this case, no phase difference is accumulated between the coherences ϕ_{13} and ϕ_{23}.

The analysis performed up to here has been referred to a system evolving in the absence of any kind of decoherence. Let us consider now the presence of noise in the phase of the atomic transitions. Two mechanisms can be foreseen that yield random phase variations in the atomic transitions during the storage time. First, consider that after the pulse is absorbed, each atom, apart from evolving according to its free Hamiltonian, is affected by spurious magnetic and electric fields. This would lead to a non-ideal rephasing after the reversing of the detuning. Second, as it has been discussed in Section 2.2 and in Subsection 1.3.6 , in order to increase the storage time it is customary to temporally transfer the population from the excited unstable level to an auxiliary level endowed with larger coherence time. This procedure is performed via the coupling with light pulses of area ν [105, 108, 109, 147]. Ideally, these pulses should couple to the system without introducing any

uncontrolled phase shift to the original atomic transition. However, in any realistic situation, the intensity and phase fluctuations of the light pulses will result in a phase shift, probably different for each atom, when the population is transferred back to the original excited level. Both aforementioned noise mechanisms can be modeled by adding a phase noise to each atomic transition. In practice each atomic coherence of each atom is subjected to phase transformations as those given by Eq. (2.16). Since the additional phase is random and centered in zero, we consider the von Mises phase distribution (circular normal distribution) that is to say, a continuous probability distribution on a circle, represented in Fig. 2.2:

$$M_j(\pi_j) = \frac{e^{k_j \cos \omega_j}}{2\nu I_0(k_j)} \tag{2.22}$$

In the definition above j refers to the level j affected by the noise, π_j is the phase acquired by this level, $I_0(k_j)$ denotes the modified Bessel function of zero order, and k_j is the inverse width of the phase noise distribution, that is assumed to be centered at zero phase value. For $k_j = 0$, the distribution is uniform along the interval $[-\nu\ \ \nu]$, while the larger the k_j, the narrower the noise distribution, and vice versa [see Fig. 2.2]. Notice that the actual form of the chosen distribution is however not relevant for our purposes.

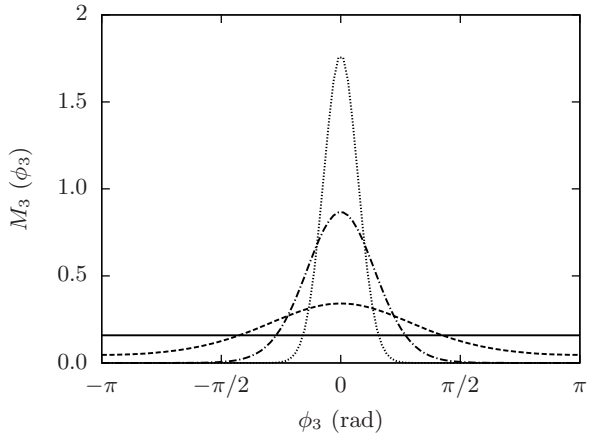

Figure 2.2: von Mises distribution of the phase of the lower level 3 , for different values of the inverse width distribution: $k_3 = 0$ (solid line), $k_3 = 1$ (dashed line), $k_3 = 5$ (dot-dashed line), $k_3 = 20$ (dotted line).

In order to introduce the effects of phase noise in Eqs. (2.4) and (2.7), one can proceed as in Eq. (2.16), but now an additional averaging over all the possible

phases must be performed in the equations for the field components:

$$\frac{}{z}\Omega^{\mathrm{b\,f}}_{\mu\rho}(z\ t) = \mp i\eta_{\mu\rho}\int_{-\pi}^{\pi} M_T d\pi_1 d\pi_2 d\pi_3 \int_{-} \quad G_{\mu\rho}(\Delta)\,\phi^{\mathrm{b\,f}}_{\mu\nu}(z\ t\ \Delta\ \pi_1\ \pi_2\ \pi_3)d\Delta \tag{2.23}$$

where $M_T \equiv M_1(\pi_1)\,M_2(\pi_2)\,M_3(\pi_3)$. For a generic noise acting upon all the atomic levels, the expressions for the retrieved fields, both in the forward and backward configurations, read as in Eqs. (2.18) except for a multiplying factor:

$$\Omega^{\mathrm{b\,f}}_{\mu\rho}(z\quad) = -K_\rho K_\mu \gamma^{\mathrm{b\,f}}(\ \ )\Omega^{\mathrm{in}}_{\mu\rho}(0\ -\ ) \tag{2.24}$$

where $K_\mu = \int_{-\pi}^{\pi} e^{\pm i\omega_\mu} M_\mu(\pi_\mu)d\pi_\mu = I_1(k_\mu)\ \ I_0(k_\mu)$ that increases, monotonously with k_μ, from zero to one.

Consider, for instance, that the phase noise acts upon level 3 only (the case of noise acting on the other levels being similar). From Eqs. (2.24), the retrieval efficiencies for the backward and forward modes can be obtained:

$$\mathrm{Eff}^{\mathrm{b\,f}}_{\mu\rho} = \left(K_3\gamma^{\mathrm{b\,f}}\right)^2 \tag{2.25}$$

where γ^{b} and γ^{f} are defined in Eqs. (2.15a) and (2.15b), respectively. Notice that the efficiency does not depend on the amplitude components of the initial field, so it is independent of the particular superposition state we are considering. Focusing in the backward scheme, we plot in Fig. 2.3(a) the retrieval efficiency as a function of the optical depth for different values of the inverse width of the distribution k_3. We see that for large k_3, *i.e.*, narrow phase noise distribution, the efficiency is unaffected by the presence of noise, and a perfect recovery of the input light pulse can be reached for a large enough optical depth. However, as k_3 becomes smaller, *i.e.*, a wider noise distribution, the efficiency suffers from relevant detrimental effects. In this case, the input pulse cannot be recovered completely, even for a large optical depth. For the forward retrieval scheme, similar results are obtained [see Fig. 2.3(b)] with the obvious difference that in this case the recovery efficiency is limited to $\sim 54\%$. These results do not contradict the above mentioned fact that both the efficiency and fidelity are unaffected by a single specific phase change π_3 of the ground state [see Eqs. (2.18) and (2.21)]. In fact, when the inhomogeneous phase noise is present, the situation is different: since each atom accumulates a different phase during the storage time, the rephasing process, which is a collective phenomenon, can not be achieved properly.

In order to have a compact assessment of the effect of the phase noise, we plot

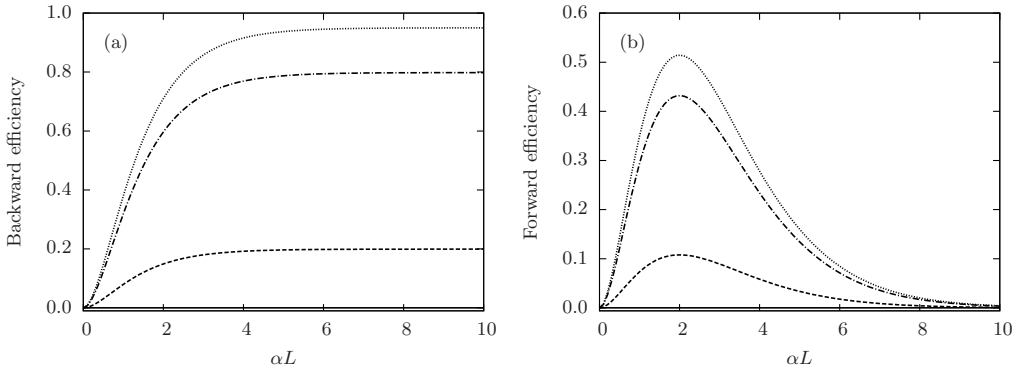

Figure 2.3: Memory efficiency for the (a) backward and (b) forward retrieval schemes as a function of the optical depth for different amounts of phase noise affecting the ground level after the absorption of the pulse. The different lines correspond to $k_3 = 0$ (solid line), $k_3 = 1$ (dashed line), $k_3 = 5$ (dot-dashed line), $k_3 = 20$ (dotted line).

in Fig. 2.4 the maximum value of the backward (solid line) and forward (dashed line) efficiency as a function of the noise parameter k_3, for the case where the phase noise is only included in level 3 . We can see that the memory efficiency in both backward and forward schemes degrades substantially as the phase noise distribution becomes wider. Note that the actual values of the noise depend on the chosen model, however the qualitative behavior is a general feature.

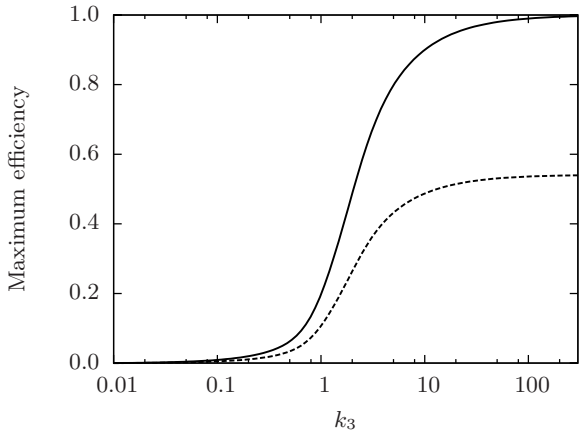

Figure 2.4: Maximum memory efficiency for the backward (solid line) and the forward (dashed line) retrieval schemes as a function of the inverse width of the phase noise distribution k_3.

In addition, to obtain a complete picture of the retrieval process in the presence

of noise, the input-output fidelity has to be considered too. As indicated, whenever noise is present the retrieval efficiency is reduced with respect to the ideal case, being below the unity also in the backward scheme. This implies that the output state $\overset{\mathrm{b\,f}}{\underset{\mathrm{out}}{}}$ is not pure any more. The expression of $\overset{\mathrm{b\,f}}{\underset{\mathrm{out}}{}}$ can be obtained, however, simply by modeling the non-ideal memory with an ideal one preceded by a beam-splitter with transmittivity equal to the efficiency of the memory. The reflected beam is then traced out. In this way, one obtains that the fidelity is equal to the retrieval efficiency.

2.3.5 Numerical Results

The analytical results reported in the previous Subsections 2.3.1-2.3.4 are based on the weak field approximation in which the temporal dynamics of the atomic populations and the two-photon coherence ϕ_{12} was neglected. In this Section we verify the validity of the analytical approach by performing numerical integration of the full optical-Bloch equations, Eqs. (2.3) and (2.4), with a finite difference method beyond this approximation. Atoms with closely spaced frequencies are grouped in equidistantly spaced frequency classes (labeled by an integer number n) with central frequencies $\overset{(n)}{}_{13} = \overset{(n)}{}_{23}$. At each spatial point z the inhomogeneous spectral distribution, provided by the transverse broadening, of the frequency classes is given by the function $G\left(\Delta^{(n)}\right)$ which, for simplicity, is assumed to be a rectangular distribution of width much larger than the spectral width of the input pulse.

The calculation scheme is performed in the following steps: (i) From the temporal profile of the incident field pulse $\Omega_{\mu\rho}(z\ t)$, we calculate the temporal evolution of the density matrix at each spatial point z and for each frequency class by integration of Eqs. (2.3) with time step Δt. (ii) This temporal evolution given by $\phi_{\mu\rho}\left(z\ t\ \Delta^{(n)}\right)$ is used in Eqs. (2.4) to propagate the components of the light pulse between the spatial points z and $z + \Delta z$. Further, steps (i) and (ii) are iterated. Temporal Δt and spatial Δz steps are chosen small enough and the number of frequency classes large enough to assure the convergence of the calculations.

During the absorption stage, the pulse propagation is initiated at $z = 0$, where the density matrices of all atom frequency classes are known. As in the analytical approach, we assume that initially all atoms are in their ground level, *i.e.*, $\phi_{33}\left(z\ t = -15\ \mu s\right) = 1$. The input field pulses at $z = 0$ are assumed to have Gaussian temporal profiles and we define the normalized intensities of each component

as

$$I_{\mu\rho}(z\ t) = \frac{\Omega_{\mu\rho}(z\ t)^{\ 2}}{\Omega_{13}(0\ t_c)^{\ 2} + \Omega_{23}(0\ t_c)^{\ 2}} \tag{2.26}$$

where $\mu = 1\ 2$, $\varphi = 3$ and t_c is the time corresponding to the peak of the pulse. The spatio-temporal dynamics of $I_{13}(z\ t)$ and $I_{23}(z\ t)$ during the absorption stage of the protocol is shown in Figs. 2.5(a) and (d), respectively. The initial intensities of the components are taken as $I_{13}(0\ t_c) = 0\,6$ and $I_{23}(0\ t_c) = 0\,4$. Note that the absence of field at the output surface, corresponding to an optical depth $\alpha z = \alpha L = 4\,5$ with L being the length of the medium, evidences the efficient absorption of both field components.

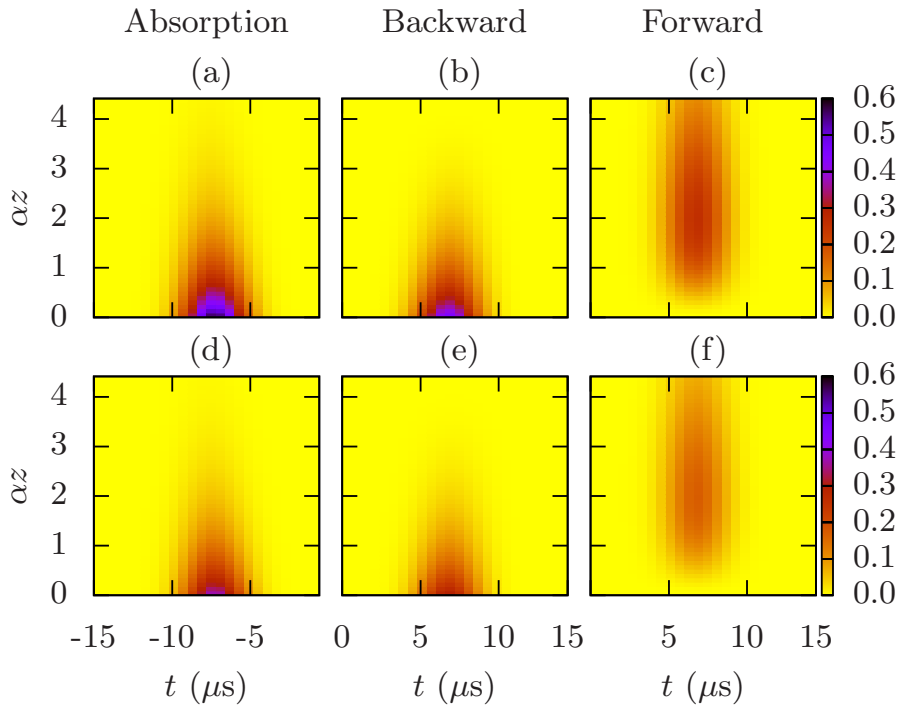

Figure 2.5: Contour plots of the spatio-temporal dynamics of the normalized intensities of the two circular polarization components of the field $I_{13}(z\ t)$ (a)-(c) and $I_{23}(z\ t)$ (d)-(f) in an inhomogeneously broadened V-system with phase noise distribution of width $k_3 = 5$ in the lower level 3. Figures (a),(d) show the absorption stage, while (b),(e), and (c),(f) correspond to the backward and forward retrieval schemes, respectively.

For the simulation of the forward and backward retrieval protocols we reverse the sign of the detuning for each frequency class $\Delta^{(n)} \quad -\Delta^{(n)}$. For the backward protocol, we additionally change the sign of the field to implement the phase

matching operation. After this step, the phase noise is introduced by imposing at each spatial position a phase distribution in the atomic coherences of each frequency class, n, given by Eq. (2.22), *i.e.*, $\phi_{\mu\nu}^{(n)}(z\ t=0) = \left|\phi_{\mu\nu}^{(n)}(z\ t=0)\right| e^{i\omega_{\mu\nu 0}^{(n)}}$, being $\pi_{\mu\nu 0}$ the phase of the class n. The ensemble average $\phi_{\mu\nu}^{(n)} = \phi_{\mu\nu}^{(n)}$ is used as the initial density matrix element for each frequency class at the retrieval stage. During the retrieval, the field propagation is evaluated by means of Eqs. (2.4) and (2.7) from the surface $\alpha z = 0$ ($\alpha z = \alpha L$) to the surface $\alpha z = \alpha L$ ($\alpha z = 0$) for the forward (backward) protocol. The spatio-temporal dynamics of the retrieved field intensities, I_{13} and I_{23}, in the presence of a phase noise distribution in the lower level 3 of inverse width $k_3 = 5$ are shown in Figs. 2.5(b) and (e) for the backward retrieval and in Figs. 2.5(c) and (f) for the forward retrieval protocols.

For the parameters used in our simulations we have numerically observed that the two-photon coherence (ϕ_{12}), the population of the excited levels (ϕ_{11}, ϕ_{22}), and the phase difference between the field components did not exceed 10^{-6} during the whole dynamics, validating the weak field approximation used to derive the analytical solutions in Subsection 2.3.1. By comparing the absorption of the field components of Figs. 2.5(a) and (d), with the corresponding retrieved fields of Figs. 2.5(b),(c) and (e),(f), respectively, we note that, although the efficiency of the reemission is lower than in the ideal case where no phase noise is present, the decrease on the retrieval intensities is the same for both components.

We have checked that beyond this particular case, the propagation dynamics and the maximal retrieval efficiencies acquired from the numerical simulations for both forward and backward protocols are in good agreement with the analytical results, confirming the validity of the approximations that we assumed in the analytical approach. In particular, for the parameter values of Fig. 2.5, the maximum backward and forward numerically evaluated efficiencies are $\mathrm{Eff}^{\mathrm{b}}_{(\mathrm{num})} = 0\ 79$ and $\mathrm{Eff}^{\mathrm{f}}_{(\mathrm{num})} = 0\ 43$, respectively, that match the analytical results shown in Fig. 2.3 for $k_3 = 5$ (dot-dashed line).

2.4 Quantum-state storage and processing for polarization qubits in an inhomogeneously broadened Λ-type three-level medium

In this Section we consider that the atoms of the storage medium are in a Λ-type configuration [see Fig. 2.1(b)], with the population being in a coherent superpo-

sition of the two-ground states 1 and 2 . This coherently prepared medium is called a phaseonium [140], and it leads to a situation dramatically different from the case of atoms in a V-scheme, exposed in the previous Section 2.3. In particular, we will show that the solutions of Eqs. (2.3) and (2.4), in contrast with the ones obtained in the V configuration case, describe stationary propagation of the field polarization components, *i.e.*, the polarization modes are not completely absorbed in general and part of the field propagates transparently. Although those propagation effects prevent a straightforward implementation of a quantum memory in this kind of Λ systems, by combining them with the CRIB technique we propose different quantum information-processing applications, such as a polarization qubit filter and sieve, as well as a tunable polarization beam splitter. Moreover, we show that, by imposing a spatial variation of the atomic coherence phase, the polarization components can be completely absorbed. Therefore, an efficient quantum memory for the incident polarization qubit can be also implemented in the Λ-type three-level system.

As discussed above, the propagation of the two polarization components in the coherently prepared Λ system will be at the basis of the quantum information applications that we propose in this Section. Therefore, in the following Subsection 2.4.1 we give a a brief introduction about the research done in this area.

2.4.1 Propagation of pulses in a phaseoium medium

The propagation of electromagnetic pulses in multilevel media has been widely investigated in the last decades. Three-level atomic media interacting with two optical fields in a Λ-type configuration have been among the most considered systems, leading to the discovery of a large variety of phenomena, such as coherent population trapping (CPT), electromagnetically induced transparency (EIT), and slow light [148]. More recently, the development of quantum technologies for quantum information applications has triggered a renewed attention on the subject. In particular, the propagation of weak or quantum light pulses in a Λ medium in the presence of strong classical driving fields has been considered in detail, giving rise to proposals and implementations for quantum state storage and processing [141].

The non-absorbing propagation of a pair of pulses in coherently prepared Λ-type media has been deeply investigated in relation to pulse matching [149 152], the dark area theorem [153], simultons [154] and adiabatons [155, 156]. In all these investigations, the initial quantum state of the atomic population plays an essential role. The term phaseonium was introduced by Scully [140] to describe

a coherent pure-state superposition between the ground levels of a Λ-medium and methods to prepare this macroscopic superposition state have been put forward for ladder [157] and Λ [158] type configurations. An interesting effect that takes place in these systems is the loss-free propagation of light pulses in otherwise optically thick media. In particular, it has been shown that matched pulses, *i.e.*, pulse pairs with identical envelopes, can propagate without distortion if the atoms are prepared in a suitable phaseonium state [150]. This phenomenon is closely related with the EIT technique, discussed in Section 1.3.

In three-level media it is common to define a new basis of the system in terms of the bright B and dark D states [159, 160] which, under the two-photon resonance condition, are given by

$$B \equiv \frac{1}{\Omega_T}\left(\Omega_{13}\ 1\ + \Omega_{23}\ 2\ \right) \tag{2.27a}$$

$$D \equiv \frac{1}{\Omega_T}\left(\Omega_{23}^{*}\ 1\ - \Omega_{13}^{*}\ 2\ \right) \tag{2.27b}$$

where $\Omega_T = \sqrt{\Omega_{13}{}^2 + \Omega_{23}{}^2}$ is the total Rabi frequency. For continuous wave light fields, it has been shown that the dynamics is restricted to the transition $B\ -\ 3$. In this case, once the system enters the dark state due to, for instance spontaneous emission from the excited level, it becomes trapped. This representation forms the basis for the EIT and CPT techniques. However, for light pulses the dynamics is different. Indeed, Kozlov and Eberly [152, 153] showed that the dark state completely controls the system evolution at large propagation distances when the medium is in a phaseonium preparation [140]. In this situation, the so called dark field [159],

$$\Omega_D(t) = \frac{\Omega_{13}(t)\Omega_{23}(t) - \Omega_{23}(t)\Omega_{13}(t)}{\Omega_T^2(t)} \tag{2.28}$$

which results from the field temporal evolution, couples the dark D and the bright B states. This means that as the pulses propagate, the dark state is inevitably populated, thus affecting to the propagation dynamics itself. Clearly, from Eq. (2.28), the dark state is decoupled from the laser fields if $\Omega_D(t) = 0$, which means that the amplitudes of the pulses can be arbitrary but they need to have the same shape: $\Omega_{13}(t)\ \Omega_{13}(t) = \Omega_{23}(t)\ \Omega_{23}(t)$, *i.e.*, they have to be matched amplitudes.

Particularly relevant for the purposes of the present study is the propagation

of two weak optical pulses through an inhomogeneously broadened phaseonium medium. For this system, it was shown in Ref. [151] that, under the two-photon resonance condition, a certain superposition of the fields, the *antisymmetric* normal mode [150, 156], does not couple to the coherent atomic state. On the contrary, the orthogonal superposition, the *symmetric* normal mode, does interact with the atoms and is completely absorbed. Both the antisymmetric and symmetric modes are determined by the phaseonium state, and can therefore be tuned according to the phase and/or the population of the atomic ground states.

In this Section, we consider the combination of the above mentioned propagation effects occurring in a Λ-type three level medium interacting with two components of a single weak pulse together with the controlled reversible inhomogeneous broadening (CRIB) [108, 109, 111] technique. We will show that the CRIB technique offers also the possibility to store and retrieve polarization qubits in a coherently prepared Λ-type system with ideally perfect efficiency and fidelity. We notice here that the application of the CRIB technique to this kind of systems is not straightforward since, as already mentioned, part of both polarization components of the single photon will propagate with matched envelopes and, therefore, they will not be completely absorbed. Hence, the quantum state of the photon can not be, in general, perfectly stored in a phaseonium Λ-type medium. However, taking profit of the coherent propagation effects, we will show that tunable polarization filters and sieves can be devised, as well as costumizable polarization splitters. Those are devices of clear interest in quantum information processing and, in particular, it will be shown that the polarization basis that determines the filter or the beam splitter action is defined by the phaseonium state. Moreover, we will show that, by forcing the field components to propagate without the possibility of adjusting their amplitudes as matched solitons, an efficient quantum memory can also be implemented in three-level Λ media.

2.4.2 Tunable polarization qubit splitter

In what follows, we consider the atoms of the medium in the Λ configuration, initially prepared in a coherent superposition of the two ground levels 1 and 2. Under the weak field approximation, the atomic population is barely excited to level 3, and Eqs. (2.3) read

$$\frac{}{t}\phi^{\mathrm{b\,f}}_{\mu\rho}(z\ t\ \Delta) = i\Delta\phi^{\mathrm{b\,f}}_{\mu\rho}(z\ t\ \Delta) + i\phi_{\mu\mu}\Omega^{\mathrm{b\,f}}_{\mu\rho}(z\ t) + i\phi_{\mu\nu}(\pi_{\mu\nu})\Omega^{\mathrm{b\,f}}_{\nu\rho}(z\ t) \qquad (2.29)$$

where now $\Delta = \ _0 - \ _{31} = \ _0 - \ _{32}$. Notice that we have included an explicit dependence on the phase $\pi_{\mu\nu} = \pi_\mu - \pi_\nu$ between the two ground levels through the coherence $\phi_{\mu\nu}$. Moreover, note that for atoms prepared initially in an incoherent mixture of the ground states, $\phi_{\mu\nu} \ = 0$, the equations for each transition of the lambda system become decoupled, leading to the same situation as when using V-type three level atoms, discussed in Section 2.3. However, for the situation described by Eqs. (2.29), the equations for the two optical coherences are coupled, thus the dynamics of the field polarization components, given by Eqs. (2.4), are coupled.

A. Quantum filter

Let us first consider the propagation of the incident pulse in the forward direction. Eqs. (2.4) and (2.29) can be analytically solved as in the previous Section 2.3, following the method of Ref. [27], by inserting the solution of Eq. (2.29) into Eq. (2.4), and Fourier transforming the result:

$$\frac{}{z}\Omega^{\text{in}}_{\mu\rho}(z \quad) = -\eta_{\mu\rho}H_{\rho\mu}(\ \ )\ \ \phi_{\mu\mu}\Omega^{\text{in}}_{\mu\rho}(z \quad) + \phi_{\mu\nu}(\pi_{\mu\nu})\Omega^{\text{in}}_{\nu\rho}(z \quad) \tag{2.30}$$

where we have used the initial conditions $\phi_{\mu\rho}(z \ t = - \ ) = 0$ and we have defined $H_{\rho\mu}(\ )$ as in Eqs. (2.9), in the previous Section 2.3. An analytical compact solution of Eqs. (2.30) can be given assuming symmetric transitions, *i.e.*, $d_{13} = d_{23} = d$, $G_{31}(\Delta) = G_{32}(\Delta) = G(\Delta)$, $\eta_{13} = \eta_{23} = \eta$, and $H_{32}(\ ) = H_{31}(\ ) = H(\ )$, which reads:

$$\Omega^{\text{in}}_{\mu\rho}(z \quad) = \Omega^{\text{in}}_{\mu\rho}(0 \quad)\left(e^{-\alpha(\ )z}\phi_{\mu\mu} + \phi_{\nu\nu}\right) + \Omega^{\text{in}}_{\nu\rho}(0 \quad)\ \phi_{\mu\nu}\ e^{i\omega_{\mu\nu}}\left(e^{-\alpha(\ )z} - 1\right) \tag{2.31}$$

where $\alpha(\ ) = \eta H(\ )$ is the absorption coefficient. These equations describe, for each frequency of the pulse, the propagation of the two polarization components of the incoming field along the medium. Each solution depends on both initial polarization components of the weak pulse $\Omega^{\text{in}}_{13}(z = 0 \quad)$ and $\Omega^{\text{in}}_{23}(z = 0 \quad))$, which implies that, in general, the information carried by each component is mixed as the pulse propagates through the Λ-medium, due to the two-photon coherence ϕ_{12}. Moreover, it is easy to see from Eqs. (2.31) that, in general, the field is not completely absorbed, even for large optical depths $\alpha(\ )z$. In particular, for $\alpha(\ )z \qquad$, the two polarization components of the pulse can only be completely

absorbed if the condition

$$\frac{\Omega_{13}^{\text{in}}(0\quad)}{\Omega_{23}^{\text{in}}(0\quad)} = \frac{c_1}{c_2} \tag{2.32}$$

with $c_\mu c_\mu^* = \phi_{\mu\mu}$, is fulfilled. However, for an arbitrary superposition of the input polarizations, both components will change their amplitudes and phases in such a way that the dark state becomes populated as they propagate [152]. If the optical depth of the medium is large enough, eventually the dark state will be fully populated, so the field components will propagate as matched solitons, without any further absorption. Indeed, it can be seen from Eqs. (2.31) that the field amplitudes will evolve until the relation

$$\frac{\Omega_{13}^{\text{in}}(z\quad)}{\Omega_{23}^{\text{in}}(z\quad)} = -\frac{c_2^*}{c_1^*} \tag{2.33}$$

is satisfied. Note that Eqs. (2.32) and (2.33) determine the symmetric and anti-symmetric normal modes, respectively, introduced in Ref. [151]. In fact, the time reversal symmetry of Eqs. (2.4) and (2.29) is not sufficient alone to guarantee the full recovery of the original input state. Clearly, the unabsorbed component of the input pulse exists the medium and cannot be recovered back. Specifically, Eq. (2.33) shows that the field which leaves the medium ends up in a well definite polarization state, which depends only on the phaseonium preparation. Assuming a large optical depth αL , the normalized intensity of each of the polarization components at the output of the medium $z = L$, from Eqs.(2.31), reads:

$$I_{\mu\rho}^{\text{in}}(L\quad) \equiv \frac{\left|\Omega_{\mu\rho}^{\text{in}}(L\quad)\right|^2}{\Omega_T^{\text{in}}(L\quad)^2} = \phi_{\nu\nu} \tag{2.34}$$

where $\Omega_T^{\text{in}}(L\quad)$ is the total Rabi frequency of the output field, as defined in Eqs. (2.27). This result perfectly agrees with Ref. [161], where it was shown that, at the output of the phaseonium medium, the amplitude of the field coupled with an optical transition ($\mu - \varphi$) depends on the ground-state amplitude of the opposite transition (ν). Moreover, one realizes that in this situation the relative phase between the output field components $\pi_{\mu\rho}(L) - \pi_{\nu\rho}(L)$, using the definition $\Omega_{\mu\rho}^{\text{in}} = \left|\Omega_{\mu\rho}^{\text{in}}\right| e^{i\omega_{\mu\rho}}$, is simply the phase $\pi_{\mu\nu}$ of the ϕ_{12} coherence. To clarify this phenomenon, consider the input pulse to be a single photon in the

generic polarization state

$$_{\text{in}} = a_L \ L \ + a_R \ R \tag{2.35}$$

entering a medium prepared in a coherent superposition

$$_{\text{at}} = c_1 \ 1 \ + c_2 \ 2 \tag{2.36}$$

Therefore, at the output, the state obtained is

$$^{\text{f}}_{\text{out}} = (c_2 - c_1)^* \, (c_2 \ L \ - c_1 \ R \ ) \tag{2.37}$$

with probability

$$P^{\text{f}}_{\text{out}} \equiv \left| \ _{\text{in}} \ ^{\text{f}}_{\text{out}} \right|^2 = \left| (\phi_{11} - \phi_{12}) \ a_R \ ^2 + (\phi_{22} - \phi_{21}) \ a_L \ ^2 \right|^2 \tag{2.38}$$

Note that since part of the incident light pulse has been absorbed by the medium, the state in Eq. (2.37) is not normalized. A convenient picture of the process is that the preparation of the phaseonium medium fixes the basis for which the incident field is filtered: after the dark state is filled, only the so called antisymmetric normal mode, Eq. (2.37), propagates without absorption. In turn the latter depends only on the phaseonium state, which ideally can be tuned at will. In other words, the medium acts as a tunable quantum filter.

B. Quantum sieve

As the pulse components propagate through the phaseonium medium, they adjust themselves to fulfill the condition given in Eq. (2.33), which allows absorption-free propagation. However, before the dark state is completely populated, part of the field, *i.e.*, the symmetric normal mode [Eq. (2.32)], is absorbed by the medium. This information stored in the optical coherences can be retrieved back by using the CRIB technique. In the following we study the propagation of the retrieved light pulse in the backward direction, which is caused by the sign change of the detunings and the phase matching operation, performed at time $t = 0$, once the non-absorbed part of the field has left the medium [27]. In this situation, the equations for the optical coherences and the Rabi frequencies of the corresponding

field components are:

$$\frac{\partial}{\partial t}\phi^{\mathrm{b}}_{\mu\rho}(z\ t\ -\Delta) = -i\Delta\phi^{\mathrm{b}}_{\mu\rho}(z\ t\ -\Delta) + i\phi_{\mu\mu}\Omega^{\mathrm{b}}_{\mu\rho}(z\ t) + i\phi_{\mu\nu}(\pi_{\mu\nu})\Omega^{\mathrm{b}}_{\nu\rho}(z\ t) \tag{2.39a}$$

$$\frac{\partial}{\partial z}\Omega^{\mathrm{b}}_{\mu\rho}(z\ t) = -i\eta_{\mu\rho}\int_{-} \quad G_{\rho\mu}\left(-\Delta\right)\phi^{\mathrm{b}}_{\mu\rho}(z\ t\ -\Delta)d\Delta \tag{2.39b}$$

again with $\varphi = 3$, $\mu\ \nu = 1\ 2$ and $\mu = \nu$. The initial and boundary conditions at the time of the detuning change of sign ($t = 0$) read:

$$\phi^{\mathrm{b}}_{\mu\rho}(z\ t = 0\ -\Delta) = i\int_{-}^{0} \ e^{-i\Delta s}\left[\phi_{\mu\mu}\Omega^{\mathrm{in}}_{\mu\rho}(z\ s) + \phi_{\mu\nu}(\pi_{\mu\nu})\Omega^{\mathrm{in}}_{\nu\rho}(z\ s)\right] ds \tag{2.40a}$$

$$\Omega^{\mathrm{b}}_{\mu\rho}(L\quad) = 0 \tag{2.40b}$$

The first initial conditions, Eq. (2.40a), are obtained from the solution of the atomic coherence [Eqs. (2.29)] at time $t = 0$, whereas the boundary condition in Eq. (2.40b) derives from the assumption that, at the time when the detuning is reversed, the non-absorbed field has left the medium. The above equations can be solved, as for the absorption stage, inserting the solution of Eq. (2.39a) into Eq. (2.39b). By Fourier transforming the result, the equations for the backward field components associated with the two transitions are:

$$\begin{aligned}\frac{\partial}{\partial z}\Omega^{\mathrm{b}}_{\mu\rho}(z\quad) =& \eta_{\mu\rho}F_{\rho\mu}(\ \ )\ \ \phi_{\mu\nu}(\pi_{\mu\nu})\Omega^{\mathrm{b}}_{\nu\rho}(z\quad) + \phi_{\mu\mu}\Omega^{\mathrm{b}}_{\mu\rho}(z\quad) \\ &+ \eta_{\mu\rho}J_{\rho\mu}(\ \ )\ \ \phi_{\mu\nu}(\pi_{\mu\nu})\Omega^{\mathrm{in}}_{\nu\rho}(z\ -\ ) + \phi_{\mu\mu}\Omega^{\mathrm{in}}_{\mu\rho}(z\ -\ )\end{aligned} \tag{2.41}$$

where $F_{\rho\mu}(\ \ )$ and $J_{\rho\mu}(\ \ )$ are given in Eqs. (2.11). As for the case of the absorption, an analytic solution for the above equations can be found. In particular, a compact expression can be derived assuming symmetric transitions and inhomogeneous distributions, as done in the derivation of Eqs. (2.31):

$$\begin{aligned}\Omega^{\mathrm{b}}_{\mu\rho}(z\quad) =& \frac{\eta J(\ \ )}{\eta\left[F(\ \ ) + H(-\ \ )\right]}\left(e^{-\eta[F(\ \ )+H(-\ \ )](L-z)} - 1\right)\times \\ &\times\ \ \Omega^{\mathrm{in}}_{\mu\rho}(0\ -\ \ )\phi_{\mu\mu} + \Omega^{\mathrm{in}}_{\nu\rho}(0\ -\ )\ \phi_{\mu\nu}\ e^{i\omega_{\mu\nu}}\end{aligned} \tag{2.42}$$

We note that, as for the forward incident propagating modes, Eqs. (2.31), the backward reemited components of the field are also a combination of the initial amplitudes. From Eqs. (2.42), it is easy to obtain that for a large enough optical

depth the normalized intensity at the output surface of the medium ($z = 0$) reads:

$$I^{\mathrm{b}}_{\mu\rho}(0\quad) \equiv \frac{\left|\Omega^{\mathrm{b}}_{\mu\rho}(0\quad)\right|^2}{\Omega^{\mathrm{b}}_{T}(0\quad)^2} = \phi_{\mu\mu} \tag{2.43}$$

where $\Omega^{\mathrm{b}}_{T}(0\quad)$ is the total Rabi frequency for the backward components at the output. In the last expression, we have considered that the spectral bandwidth of the pulse is smaller than the inhomogeneous broadening, $F(\ )\quad H(-\ )$ $J(\ )\ 2\quad \nu\ 2$, and that the absorption coefficient reduces to $\alpha\quad \eta\nu\ 2$. In this situation, the relative phase between the field components corresponds to the phase difference between the ground levels, $\pi_{\mu\rho}(0) - \pi_{\nu\rho}(0) = \pi_{\mu\nu}$. For the single-photon case, the backward retrieved components exit the medium, with probability

$$P^{\mathrm{b}}_{\mathrm{out}} = 1 - P^{\mathrm{f}}_{\mathrm{out}} \tag{2.44}$$

where $P^{\mathrm{f}}_{\mathrm{out}}$ is given in Eq. (2.38), in a state of the form

$$^{\mathrm{b}}_{\mathrm{out}}\ = -\left(c_1 + c_2\right)\left(c_1^*\ L\ + c_2^*\ R\ \right) \tag{2.45}$$

which is orthogonal to the state in Eq. (2.37) and corresponds to the so called symmetric normal mode. Therefore, the system acts as a tunable quantum sieve that can reemit the sieved state on demand. Note that since part of the field is absorbed by the medium, the sum of the norms of states in Eqs. (2.37) and (2.45) must be one.

To summarize, by applying the CRIB technique the phaseonium medium can act as a tunable polarization qubit splitter: part of the field ends up in the anti-symmetric (unabsorbed) mode, which exits in the forward direction, while the rest is absorbed. Moreover, the stored symmetric mode can be recovered on-demand in the backward direction with ideally arbitrary time delay. Moreover, this system acts as a state filter, since one could properly adjust the phaseonium state to filter out the non desired polarization components of a particular superposition state. The same idea works for the implementation of a quantum sieve, since only a particular desired superposition of the two field components is stored and the rest exits the medium. An example of the tunable polarization splitter performance is shown in Fig. 2.6, where the normalized intensity of each polarization component $\Omega_{13}\ ^2$ (black lines) and $\Omega_{23}\ ^2$ (gray lines) is plotted as a function of the optical distance αz. The solid lines correspond to the propagation of the po-

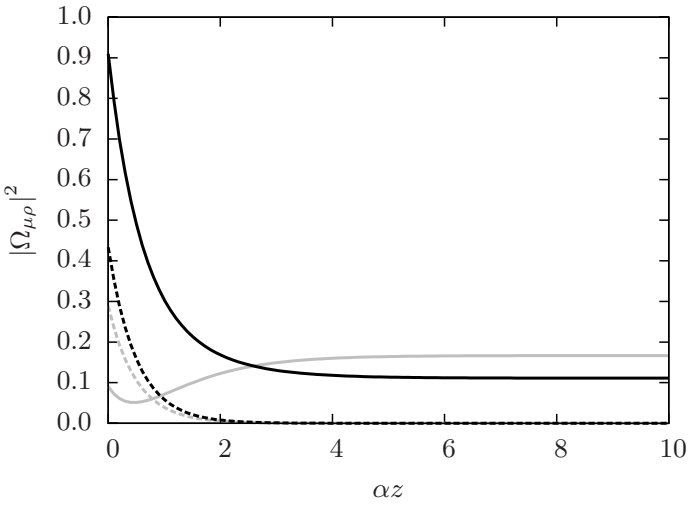

Figure 2.6: Normalized intensities of the single pulse polarization components (see text for definition) coupled with the $1-3$ (black lines) and $2-3$ (gray lines) optical transitions as a function of the optical distance αz. The solid lines correspond to the propagation of the incident field [Eqs. (2.31)] while the dashed lines correspond to the backward retrieved components [Eqs. (2.42)]. The initial prepared state of the phaseonium medium is $\phi_{11} = 0\,6$, $\phi_{22} = 0\,4$, $\pi_{12} = \nu\ 3$, whereas the field components are initially weighed as $I_{13}^{\rm in}(0\ t_c) = 0\,9$ and $I_{23}^{\rm in}(0\ t_c) = 0\,1$ with relative phase between them being $\pi_{13}(0) - \pi_{23}(0) = 0$.

larization components of the incident field, Eqs. (2.31), whereas the dashed lines represent the components of the backward retrieved single photon, Eqs. (2.42). In this particular case, a medium of optical depth $\alpha L = 10$ has been chosen with the atomic population prepared initially in a coherent superposition fulfilling $\phi_{11} = 0\,6$, $\phi_{22} = 0\,4$ and $\pi_{12} = \nu\ 3$. The two components of the input light pulse have been assumed to have the relative phase of $\pi_{13}(0) - \pi_{23}(0) = 0$ and initial weights $I_{13}^{\rm in}(0\ t_c) = 0\,9$ and $I_{23}^{\rm in}(0\ t_c) = 0\,1$, where t_c denotes the time of the pulse peak in the moving frame of the light. In Fig. 2.6, we observe how the incident components (solid lines) change their amplitudes along propagation and that beyond a certain optical distance they propagate as matched solitons. The total intensity at the output is given by Eq. (2.38), whereas Eqs. (2.34) determines which fraction of the total transmitted intensity is in each mode. Since during the transient regime part of the field has been absorbed, the CRIB technique allows to recover (dashed lines) this information stored in the optical coherences. Clearly, since part of the field has left the medium, the retrieved intensity is smaller than the initial one. In this case, the total retrieved intensity is given by Eq. (2.44)

while the distribution of the atomic populations determine which is the fraction of the output intensity associated to each polarization component, as given by Eqs. (2.43).

2.4.3 Quantum memory in a longitudinal phaseonium

The analysis performed up to here, is referred to a system with all the atoms prepared in the same coherent superposition of the ground states. We have seen that the propagation of a pair of pulses through this spatially homogeneous phaseonium leads to an automatic adjusting of the pulse components to fulfill condition given by Eq. (2.33). This prevents complete absorption and, in turn, the straightforward implementation of a quantum memory. In what follows, we will see that the latter can nevertheless be overcome by imposing that the preparation of the Λ-system depends on the position. In particular, we consider that the phase of the two-photon coherence π_{12} varies with the position along the light propagation direction:

$$\pi_{12}(z) = \theta \frac{z}{L} \tag{2.46}$$

with θ being the phase imposed in the medium at $z = L$. This preparation can be implemented, for instance, by applying a linear magnetic field gradient coupling the two ground levels. The magnetic field produces an opposite Zeeman shift of ground energy levels which magnitude depends on the field strength. After a certain time the magnetic field is switched off, yielding a spatial linear phase between the two ground levels. The equations describing the evolution of the system in this situation, are the same as in Eqs. (2.4) and (2.29), but now with the corresponding position dependence of the two-photon coherence phase. Following the same procedure as in Subsection 2.4.2, an analytical solution for the field components propagating in a position dependent phaseonium medium can be obtained:

$$\begin{aligned}\Omega^{\text{in}}_{\mu\rho}(z\quad) = \Bigg\{ \Omega^{\text{in}}_{\mu\rho}(0\quad) \left[\cosh \frac{K_+ z}{2L} - (-1)^\nu \frac{i\theta}{K_+} \sinh \frac{K_+ z}{2L} \right] - \\ \Omega^{\text{in}}_{\nu\rho}(0\quad) \frac{\alpha(\ \ )L}{K_+} \sinh \frac{K_+ z}{2L} \Bigg] e^{(-1)^\nu \frac{i\theta z}{2L} - \frac{\alpha(\omega) z}{2}}\end{aligned} \tag{2.47}$$

where $K_+ \equiv \quad \overline{(\alpha(\ \ )L)^2 - \theta^2}$, and for simplicity we have taken the particular case $\phi_{11} = \phi_{22} = 0$ 5. Analyzing this expression carefully, one realizes that, in general, it decays to zero for large enough optical depths $\alpha(\ \ )L$, and only for $\theta = 0$ the field

components will not be absorbed. The physical reason for this result is that, since the phase of the coherence between the ground states is different at each position of the medium, the field components are not able to adjust their amplitudes and phases to fulfill the condition given by Eq. (2.33) as they propagate. Therefore, the dark state is not populated and consequently each component of the field is absorbed. In particular, if the variation of the phase along the medium is large compared with the optical depth, *i.e.*, $\theta - \alpha(\ )L$, an exponential decay of each component is observed:

$$\Omega^{\text{in}}_{\mu\rho}(z \quad) \quad e^{-\frac{\alpha(\omega)z}{2}}\Omega^{\text{in}}_{\mu\rho}(0 \quad) \tag{2.48}$$

As in the standard CRIB approach, the stored information can be retrieved in the backward direction by reversing the sign of the detuning and applying a phase matching operation. This leads to a backward propagating solution of the field components of the form:

$$\Omega^{\text{b}}_{\mu\rho}(z \quad) = C_{\mu\mu}\Omega^{\text{in}}_{\mu\rho}(0 \ - \ ) + C_{\mu\nu}\Omega^{\text{in}}_{\nu\rho}(0 \ - \ ) \tag{2.49}$$

where

$$\begin{aligned} C_{\mu\mu} \equiv \Bigg[& e^{\frac{z\eta F(\omega)}{2}} e^{-\frac{L\eta[F(\omega)+H(-\omega)]}{2}} \left(K_- \left[(-1)^\nu i\theta \sinh W + Q\cosh W\right] \cosh\frac{K_-}{2} + \right. \\ & \left. \left\{ \left[\theta^2 + L^2\eta^2 F(\ )H(-\ )\right] \sinh W - (-1)^\nu i\theta Q \cosh W \right\} \sinh\frac{K_-}{2} \right) - \\ & e^{-\frac{z\eta H(-\omega)}{2}} Q \left[K_- \cosh\frac{K_- z}{2L} - (-1)^\nu i\theta \sinh\frac{K_- z}{2L} \right] \Bigg] \frac{e^{(-1)^\nu i\frac{\theta z}{2L}} J(\ )}{QK_-\left[F(\ ) + H(-\ )\right]} \end{aligned} \tag{2.50a}$$

$$\begin{aligned} C_{\mu\nu} \equiv \Bigg[& e^{\frac{z\eta F(\omega)}{2}} e^{-\frac{L\eta[F(\omega)+H(-\omega)]}{2}} \left(K_- F(\ ) \sinh W \cosh\frac{K_-}{2} + \right. \\ & \left. QH(-\ ) \cosh W + (-1)^\nu i\theta \left[F(\ ) + H(-\ )\right] \sinh W \ \ \sinh\frac{K_-}{2} \right) - \\ & e^{-\frac{z\eta H(-\omega)}{2}} QH(-\ ) \sinh\frac{K_- z}{2L} \Bigg] \frac{-e^{(-1)^\nu i\frac{\theta z}{2L}} J(\ )\eta L}{QK_-\left[F(\ ) + H(-\ )\right]} \end{aligned} \tag{2.50b}$$

and $K_- \equiv \quad \overline{(\eta H(-\ )L)^2 - \theta^2}$, $W \equiv Q(1 - z \ L) \ 2$ with $Q \equiv \quad \overline{(\eta F(\ )L)^2 - \theta^2}$. These cumbersome expressions can be written in a much simpler form using the assumption $F(\ ) \quad H(-\ ) \quad J(\ ) \ 2 \quad \nu \ 2$, which leads to $K_- \quad K_+ \quad Q$. Moreover, one can realize that for the case of optically thick medium (αL

), *i.e.*, when the incident field is completely absorbed, Eqs. (2.49) simplify to $\Omega^{\rm b}_{\mu\rho}(z\quad) = -\Omega^{\rm in}_{\mu\rho}(z\quad)$. Thus, each component of the field is perfectly retrieved with a global phase change of ν.

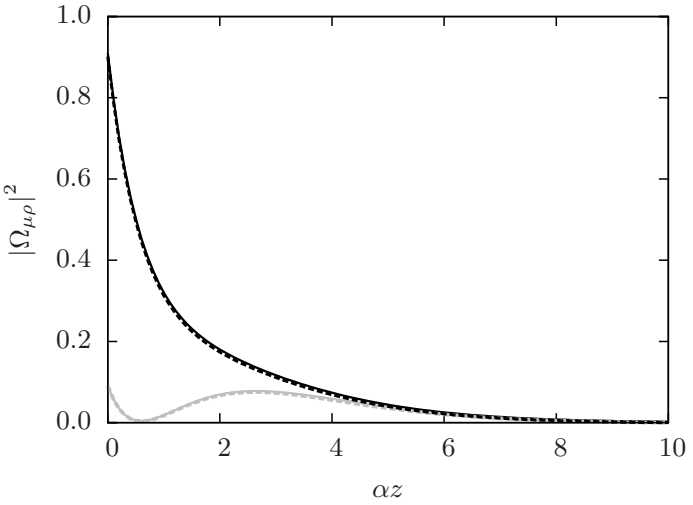

Figure 2.7: Normalized intensities of the single pulse polarization components (see text for definition) $\Omega_{13}{}^2$ (black line) and $\Omega_{23}{}^2$ (gray line) as a function of the optical distance αz. The solid lines correspond to the incident field [Eq. (2.47)] while the dashed lines correspond to the backward retrieved components [Eq. (2.49)]. Initially Λ-type three-level atoms of phaseonium are prepared in state $\phi_{11} = \phi_{22} = 0\,5$ with phase gradient of $\theta = 3\nu$. The field components have initially relative intensities $I^{\rm in}_{13}(0\ t_c) = 0\,9$ and $I^{\rm in}_{23}(0\ t_c) = 0\,1$, and the relative phase between them is $\pi_{13}(0) - \pi_{23}(0) = 0$ both for the forward input and the backward output.

Fig. 2.7 shows an example of the absorbed and retrieved normalized intensity of each polarization component, $\Omega_{13}{}^2$ (black line) and $\Omega_{23}{}^2$ (gray line), as a function of the optical distance αz, for the position dependent phaseonium. The parameter values considered are $\phi_{11} = \phi_{22} = 0\,5$, $\theta = 3\nu$, $\pi_{13}(0) - \pi_{23}(0) = 0$, $I^{\rm in}_{13}(0\ t_c) = 0\,9$ and $I^{\rm in}_{23}(0\ t_c) = 0\,1$. This plot clearly shows that the incident polarization components (solid lines), given by Eqs. (2.47), are completely absorbed for a finite optical distance αz. The dashed lines correspond to the components of the backward retrieved field, Eqs. (2.49), and we observe practically no difference with the incident components. At $z = 0$, the relative phase between the two polarization components, not shown in the figure, is the same for the stored (forward input) and retrieved (backward output) photons. Thus, the system is able to store and retrieve on-demand a single polarization qubit with unit fidelity.

2.4.4 Numerical analysis

The results reported up to now in this Section are based on the assumption, taken under the weak field approximation, that the atomic populations and the two-photon coherence ϕ_{12} do not evolve in time. In order to check the validity of the analytical approach, we have performed exact numerical simulations by integrating the full optical Bloch equations, Eqs. (2.1) and (2.4), with a finite difference method, similar to the one described in Subsection 2.3.5 and assuming Gaussian temporal profiles for the pulse components.

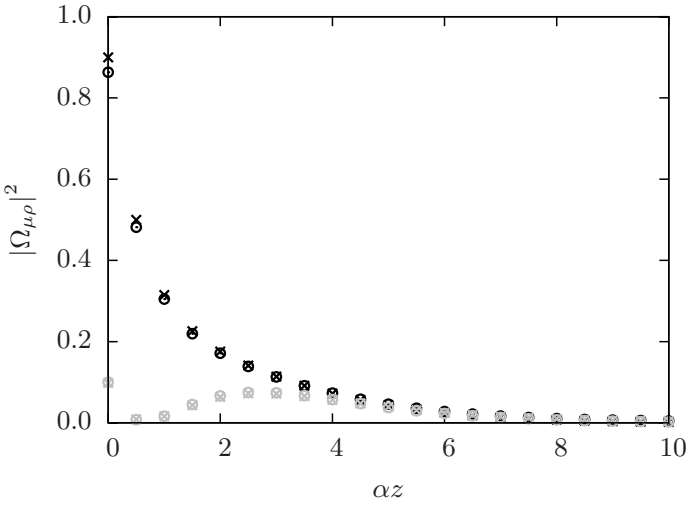

Figure 2.8: Normalized intensities of the single pulse polarization components coupled with the $1-3$ (black symbols) and $2-3$ (grey symbols) transitions as a function of the optical distance αz after numerical integration of the full optical Bloch equations, Eqs. (2.1) and (2.4). The crosses correspond to the propagation of the incident field while the circles correspond to the backward retrieved components. The parameters are the same as in Fig. 2.7.

An example of the numerical results corresponding to the longitudinal phaseonium case is shown in Fig. 2.8. In this figure, the normalized peak intensity of both field components is shown as a function of the optical length with the same parameter values as in Fig. 2.7. Comparing these two figures we conclude that the analytical results are in complete agreement with the numerical simulations. Moreover, we have checked that, as expected, the relative phase between the incident field and the backward reemitted field is preserved, and the populations and the two-photon coherence do not exhibit relevant dynamics. This confirms the validity of the weak field approximations performed in Subections 2.4.2 and 2.4.3.

2.5 Practical considerations

Along this Chapter we have proposed the implementation of a quantum memory for qubits in a superposition state of left and right circular polarizations in V- and Λ-type three-level atoms. In the original CRIB proposal [109] rare-earth-ion-doped (REID) crystals were suggested as possible candidates to implement quantum memories due to its well-known energy level structure and long coherence times at low temperatures [34, 106, 107]. Later, this kind of systems has been one of the best candidates for light storage using the CRIB technique [29, 39, 48, 111, 112]. However, although three-level configurations have been implemented in REID crystals (see for instance [70] for a EIT experiment in $Pr^{3+} : Y_2SiO_5$), the optical transitions in this kind of systems are not polarization selective, so the only way to address them separately is to use a source whose bandwidth is smaller than the ground-state sublevel splitting. Moreover, in general, REID crystals are birefringent, which means that the absorption depends strongly on the polarization of the incident light. Those restrictions are important drawbacks for the implementation of our proposal in REID crystals, since we need a system with specific selection rules to absorb the left and right circular polarization components of the photonic qubit. Nevertheless, atomic vapors do not suffer from these limitations and could be good candidates to implement a polarization qubit three-level memory. In particular, regarding photon echo quantum memories, warm [40] and cold [119] atoms of ^{87}Rb have been shown to be useful for Λ-type GEM implementations, with reasonable high efficiencies and storage times.

2.6 Conclusions

In this Chapter, we have studied the implementation of a quantum memory for polarization qubit storage in three-level atomic ensembles. Our main motivation has been to propose a quantum memory capable of storing the polarization state of light without using two separated storage media, that could lead to a reduction of the efficiency and the fidelity of the memory, and would need extra experimental efforts for its reliable implementation. We have extended the CRIB technique to three level systems, both in the V and in the Λ configurations. The equations to describe the dynamics of the atomic coherences and the field polarization components have been derived, following the procedure of Ref. [27]. Although the derivation has been performed in the semiclassical formalism, the linearity

of the equations, under the weak field approximation, allow for a fully quantum mechanical interpretation of the results.

In Section 2.3, we have shown that optical quantum memories based on V-type three-level atoms can be used to store and retrieve polarization qubits by means of the CRIB technique without the need of two separate quantum memories or spatially splitting the input state, hence presenting experimental compactness. In the weak field regime, the optical-Bloch equations for the three-level atoms decouple into two sets of equations describing the evolution of the two polarization components of the field resulting in two independent two-level quantum memories. In this scenario, we have analytically studied the effect of an extra phase in the atomic coherences. We have shown that when the phase variations affect equally all the atoms of the sample, the fidelity is degraded whereas the efficiency for each polarization component of the pulse is unaffected. In contrast, when we consider an inhomogeneously distributed phase noise for the different levels, the rephasing process during the retrieval stage is not properly achieved and both the efficiency and the fidelity are degraded. In addition, we have numerically checked the assumptions performed in the analytical approach, by numerically integrating the full optical-Bloch equations. The good agreement between the numerical and analytical results demonstrates the validity of the analytical results obtained under the weak field approximation.

Next, in Section 2.4, we have studied the propagation of a weak pulse whose two polarization components are coupled with the two transitions of a coherently prepared Λ-type three-level medium presenting artificial inhomogeneous broadening. The propagation effects that normally exhibit this kind of systems have been used in combination with the CRIB technique to discuss potential quantum information applications. On the one hand, we have proposed the use of the Λ-type system as a quantum filter. This proposal is based on the fact that part of the incident pulse, the antisymmetric normal mode, which is uniquely determined by the preparation of the atoms in the phaseonium state, propagates without distortion. On the other hand, we have shown that the orthogonal component, *i.e.*, the symmetric normal mode, can be efficiently and completely absorbed and retrieved in the backward direction using the CRIB technique. In this case, the system can be used to implement a quantum sieve or, considering both the transmitted and the retrieved orthogonal modes, a tunable polarization qubit splitter. Furthermore, we have seen that, by adding a position-dependent phase coherence in the phaseonium medium, the field components can not populate the dark state allowing for

a complete absorption of both field components. Then, by applying the CRIB technique, both components can be recovered on-demand, thus implementing a quantum memory for polarization qubits. Finally the validity of the analytical approach, which is based on the weak field approximation, has been checked by numerically integrating the full optical Bloch equations. The numerical results obtained are in a very good agreement with the analytical solutions.

3

Two-color quantum memory in double Λ-media

In this Chapter, we propose a quantum memory for a single photon wave packet in a superposition of two different colors, *i.e.*, two different frequency components, an idea that has been recently accepted for publication in Phys. Rev. A. Our proposal is based on the electromagnetically induced transparency (EIT) technique [61], using an ensemble of atoms in a double-Λ configuration. Specifically, we examine a particular configuration in which the two frequency components are able to exchange energy through a four-wave mixing process as they propagate [162, 163], so the state of the incident photon is recovered periodically at certain positions in the medium. We investigate the propagation dynamics as a function of the relative phase between the coupling beams and the input single photon frequency components. Moreover, by considering time dependent coupling beams, we numerically simulate the storage and retrieval of a two frequency component single photon qubit.

The Chapter is organized as follows. First, in Section 3.1 we review some of the research done in the context of EIT in double-Λ media, and the approaches towards the storage of light with two frequency components using this atomic configuration. In Section 3.2, we describe the physical system that we will consider and derive the equations that govern its evolution. Next, in Section 3.3, we solve analytically the propagation equations of the incident single photon frequency components and study several cases using different input superposition states and control fields parameters. In Section 3.4, numerical integration of the evolution equations of the system is performed to check the validity of the analytical approach, and the storage and retrieval of a particular input superposition state is presented. Finally, we summarize the results of this work and present the main conclusions

in Section 3.5.

3.1 Introduction

Among the different methods to implement quantum memories, the approach based on electromagnetically induced transparency (EIT) [34, 61, 64 68], discussed in Subsection 1.3.3, is one of the most used, allowing to store a single photon in solid state systems for times > 1 s [34]. This technique consists in slowing down a weak light pulse coupled to one transition of a Λ-type three-level system in the presence of a control field coupled to the other optical allowed transition. By adiabatically turning-off the control field the light pulse is absorbed and mapped into the coherence between the ground states. Next, after a desired time which should be smaller than the decay time of the ground states coherence, the control field is turned on again and the initial light pulse is recovered.

For the storage of a general photonic qubit, *i.e.*, a single photon in an arbitrary superposition of two different components, more sophisticated schemes are needed [31, 75 78, 83, 96, 99, 100, 114 116, 131 133, 164 168]. For instance, in Chapter 2 we have proposed different ways to store a qubit in a superposition of two polarizations using the CRIB technique. Nonetheless, depending on the physical system used for the storage, the transmission channel of the qubits or the protocol to process the information, other kinds of encoding could be interesting. In particular, several works have focused on the storage of photons with two frequency components using the EIT technique in resonant double-Λ media [77, 83, 166 172], *i.e.*, two weak frequency components propagating under two-photon resonance condition with two strong control beams. Those proposals have been formulated mainly in the semiclassical regime. However, the storage of a two-color quantum entangled state would be interesting because it would have potential applications in quantum information networks, *e.g.*, they could be used to link systems of different nature [173, 174]. One of the main issues regarding two-color memories, both in quantum and classical approaches, is that the existence of a dark state in resonant double-Λ systems [175, 176] together with the presence of four-wave mixing processes lead to a pulse matching effect of the frequency components [177]. This implies that the two input frequency modes can not be independently stored [83]. In particular, only a specific combination of the two modes can be perfectly absorbed and recovered [167, 177, 178], whereas for an arbitrary two frequency mode input, part of the light will propagate transparently

and part will be absorbed [167].

It has been shown that the four-wave mixing processes arising in resonant double-Λ media, which make difficult the implementation of a suitable quantum memory, have interesting applications in frequency conversion of classical probe beams [162, 177], single-photon frequency conversion preserving the quantum coherence [176], and in the possibility to combine or redistribute one or two previously stored frequency modes [166, 168, 178], even with different relative intensities [167]. However, to the best of our knowledge, there are no proposals discussing the storage and retrieval of a single photon in an arbitrary two-color state. Therefore, in this Chapter we combine the usual EIT based storage technique with the four-wave mixing properties of a double-Λ system to implement a quantum memory for single photons in an arbitrary superposition state of two frequencies.

The main difference of our two-color quantum memory proposal with respect other approaches using double-Λ systems, is that we consider one of the two Λ systems of the configuration far detuned from the one photon resonance. This scheme is interesting since it gives rise to significant changes in the propagation behavior of the frequency components respect to the resonant case. In particular, considering the continuous wave regime, it has been shown that, in this configuration, the total light intensity is weakly absorbed during the propagation [162, 179], while the intensity of each mode oscillates sinusoidally with the optical length, being the energy transferred back and forth between the two probe beams. Later, a similar result was obtained in the quantum regime [163], where a single photon coupled initially to one of the transitions of the double-Λ system oscillates during propagation between the two frequency modes, thus creating, with high efficiency, a superposition state at certain positions in the medium.

Here we show, by solving the evolution equations of the single photon frequency components, that an arbitrary input superposition of two frequency modes can be recovered at certain positions of the medium. Moreover, we find that the relative phase between the coupling fields and the particular form of the input state play a crucial role in the propagation dynamics of the frequency components. Finally, we demonstrate the feasibility of the storage and retrieval of the frequency superposition state by the numerical integration of the evolution equations of the system using realistic parameter values.

3.2 Physical model

We consider the physical system sketched in Fig. 3.1, where a single photon wave packet in a superposition of two different frequency modes, of central frequencies ω_{p1}^{0} and ω_{p2}^{0}, and corresponding amplitudes E_{p1}^{+} and E_{p2}^{+}, propagates through a system formed by Λ-type three-level atoms. Both frequency components interact with the left optical transition of the three-level atoms with a different detuning, δ_{p1} or δ_{p2}, being δ_{p2} far from the one photon resonance while δ_{p1} is close to resonance. We assume that the difference between the detunings is much larger than the spectral widths of the frequency components, such that there is no overlap between them. The other optical transition is driven by two strong coupling beams, of frequencies ω_{c1}^{0} and ω_{c2}^{0}, tuned in two photon resonance with the corresponding single photon components, thus forming a double-Λ system. We consider that initially all the atoms are in the ground state $|1\rangle$. The total decay rate by spontaneous emission from the excited to the ground states is γ_2, and the decoherence rate of the ground states is denoted by γ_{13}.

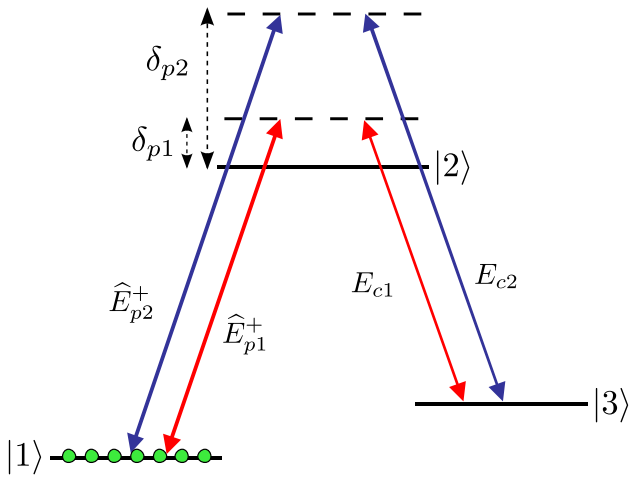

Figure 3.1: (color online). Double-Λ atomic scheme coupled with single photon frequency components, E_{p1}^{+} and E_{p2}^{+}, and classical field amplitudes, E_{c1} and E_{c2}, satisfying the two photon resonance condition. The fields are detuned from the one photon resonance with corresponding detunings δ_{p1} and δ_{p2}, with $\delta_{p1} \ll \delta_{p2}$. All the atoms are initially in state $|1\rangle$.

The total Hamiltonian of the system is given by three contributions, the atomic

(H_A), the field (H_F), and the interaction (H_I) Hamiltonians

$$H_A = \quad (\ {}_1\phi_{11} + \ {}_2\phi_{22} + \ {}_3\phi_{33}) \tag{3.1a}$$

$$H_F = \int \quad {}_p a\ {}_p a\ {}_p d\ \ {}_p \tag{3.1b}$$

$$\begin{aligned} H_I = - \quad & \Big(\mu_{12}\phi_{21}^{(1)} E_{p1}^{+} + \mu_{12}\phi_{21}^{(2)} E_{p2}^{+} \\ & + \phi_{23}^{(1)}\ \ \Omega_{c1}^{0} + \phi_{23}^{(2)}\ \ \Omega_{c2}^{0} + H\ c\ \Big) \end{aligned} \tag{3.1c}$$

where the atomic population and coherence operators are of the form $\phi_{\nu\nu} = \ \nu \quad \nu$ and $\phi_{\nu\rho}^{(j)} = \ \nu \quad \varphi^{(j)}$, respectively, where $\nu = \varphi = \ 1\ 2\ 3$ and $j = \ 1\ 2$ refers to the coherence generated by the mode $\ {}^{0}_{pj}$. The energy of the atomic state $\ \nu$ is given by $\quad {}_\nu$, being $\quad$ the Planck s constant, μ_{12} is the electric dipole moment of the $1 \ - \ 2$ transition, and $a\ {}_p$ and $a\ {}_p$ are the creation and annihilation field operators, respectively, for a frequency mode $\ {}_p$. The Rabi frequencies of the classical beams are denoted by $\Omega_{cj}^{0} = \Omega_{cj} e^{-i\ {}^{0}_{cj}(t - z\ c) + i\omega_j}$, where $\Omega_{cj} = \ \mu_{23}\ \ E_{cj} \quad$, μ_{23} is the dipole moment of the $3 \ - \ 2$ transition and E_{cj} the corresponding electric field amplitude. The amplitudes of the quantum field operators read

$$E_{pj}^{+} = \int \epsilon_{\ {}_p}^{(j)} a\ {}_p e^{+i\frac{\omega_p}{c} z} d\ \ {}_p \tag{3.2}$$

where c is the speed of light in vacuum and $\epsilon_{\ {}_p}^{(j)} = \epsilon \quad (\ {}_p - \ {}^{0}_{pj})\ \Delta\ {}_{pj}$, with $\epsilon = \ \overline{\frac{12}{2\ {}_0 V}}$, ${}_0$ the electric permittivity in vacuum, ${}_{12} = \ {}_1 - \ {}_2$ the transition frequency between states 1 and 2, V the quantization volume, and $(\ )$ a boxcar function of width $\Delta\ {}_{pj}$, centered at ${}^{0}_{pj}$. We assume $\Delta\ {}_{pj}$ much larger than the spectral width of the corresponding frequency component $\delta\ {}_{pj}$, but not enough to overlap with the other one, *i.e.*, $\left|\ {}^{0}_{p2} - \ {}^{0}_{p1}\right| - \ \Delta\ {}_{pj} - \ \delta\ {}_{pj}$.

To find the evolution equations of the single photon frequency components we adopt the procedure and formalism from Ref. [105, 147]. The initial state of the system has the form

$$\ {}_i(t \quad - \quad) \ = \int d\ \ {}_{p1} f_{\ {}_{p1}}^{(1)}(- \quad) a\ {}_{p1}\ 0\ 0\ {}_p\ 1 \ + \int d\ \ {}_{p2} f_{\ {}_{p2}}^{(2)}(- \quad) a\ {}_{p2}\ 0\ 0\ {}_p\ 1 \tag{3.3}$$

where $\quad {}_{pj} \quad [\ {}^{0}_{pj} - \Delta\ {}_{pj}\ \ 2 \quad {}^{0}_{pj} + \Delta\ {}_{pj}\ 2]$. Here we have used the notation $n_1\ n_2\ {}_p\ \nu$, where n_1 and n_2 are the number of photons in modes ${}^{0}_{p1}$ and ${}^{0}_{p2}$,

respectively, and ν denotes the atomic state. Tracing out the atomic part, the first and second terms in the r.h.s of Eq. (3.3) correspond to the initial state of each frequency component of the single photon, and $f^{(j)}_{pj}(-\quad)$ are the envelope functions of the wave packet, which have a narrow peak at $\overset{0}{}_{pj}$. We assume that they are spectrally separated enough such that their overlap is negligible, and therefore satisfy $\int d\ _{p1}\left|f^{(1)}_{p1}(-\quad)\right|^2+\int d\ _{p2}\left|f^{(2)}_{p2}(-\quad)\right|^2=1$. So, the photon is initially in an arbitrary superposition of the two frequency components, and the atoms are all in the ground state $\ 1\ $. Next, we assume that the general form of the state of the system at any time is

$$(t)\ =\ \ {}_1(t)\ +\ \ {}_2(t)\ +\ \ {}_3(t) \tag{3.4}$$

where the first, the second and the third terms correspond to the excitation being either in one of the photonic modes, in the atomic state $\ 2\ $, or in state $\ 3\ $, respectively. Their explicit forms are

$${}_1(t)\ =\int f^{(1)}_{p1}(t)a\ _{p1}\ 0\ 0\ _p\ 1\ \ d\ \ _{p1}+\int f^{(2)}_{p2}(t)a\ _{p2}\ 0\ 0\ _p\ 1\ \ d\ \ _{p2} \tag{3.5a}$$

$${}_2(t)\ =\sum_{i=1}^{N} b_1(t)\phi^{(1)}_{21}\ 0\ 0\ _p\ 1\ +b_2(t)\phi^{(2)}_{21}\ 0\ 0\ _p\ 1 \tag{3.5b}$$

$${}_3(t)\ =\sum_{i=1}^{N} g(t)\phi_{31}\ 0\ 0\ \ 1 \tag{3.5c}$$

where the sums are over all the N atoms of the medium, $b_1(t)$ and $b_2(t)$ are the probability amplitudes of exciting one atom to state $\ 2\ $ through modes $\overset{0}{}_{p1}$ and $\overset{0}{}_{p2}$, respectively, and $g(t)$ is the probability amplitude of transferring the population to state $\ 3\ $ via a two photon process. Those functions together with $f^{(1)}_{p1}(t)$ and $f^{(2)}_{p2}(t)$, give a complete description of the state of the system. In order to find their evolution, we insert the general form of the state of the system Eq. (3.4) into the Schrodinger equation and apply $\ 1\ 0\ _p\ 1\ ,\ \ 0\ 1\ _p\ 1\ ,\ \ 0\ 0\ _p\ 2\ ,$ and $\ 0\ 0\ _p\ 3\ $, obtaining:

$$i\ \ {}_t f^{(j)}_{pj}(t)=\ \ {}_{pj}f^{(j)}_{pj}(t)-\frac{\mu_{12}}{}N\epsilon b_j(t)e^{-i\frac{\omega_{pj}}{c}z} \tag{3.6a}$$

$$i\ \ {}_t b_j(t)=\ \ {}_2b_j(t)-g(t)\Omega^0_{cj}-\frac{\mu_{12}}{}\epsilon\int d\ \ {}_{pj}f^{(j)}_{pj}(t)e^{i\frac{\omega_{pj}}{c}z} \tag{3.6b}$$

$$i\ \ {}_t g(t)=\ \ {}_3g(t)-\ \ \left(\Omega^0_{c1}\right)^* b_1(t)+\left(\Omega^0_{c2}\right)^* b_2(t) \tag{3.6c}$$

Next, multiplying Eqs. (3.6a) by $e^{i\ _{pj}z\ c}$ and integrating over $_{pj}$ we obtain the propagation equation for the quantum field amplitudes

$$\left(\frac{1}{c}\ _t+\ _z\right)\mathcal{E}_j(z\ t)=i\kappa_{12}\beta_j(z\ t) \tag{3.7}$$

where we have defined $\mathcal{E}_j(z\ t)e^{-i\ \overset{0}{}_{pj}(t-z\ c)}=\underline{\mu_{12}}\epsilon\int d\ _{pj}f^{(j)}_{pj}(t)e^{i\ _{pj}z\ c}$, $\beta_j(z\ t)=b_j(t)e^{i\ \overset{0}{}_{pj}(t-z\ c)}$, and $\kappa_{12}=\frac{N\ \mu_{12}\ ^2\epsilon^2}{^2c}$. With these definitions, Eqs. (3.6b) and (3.6c) read

$$_t\beta_j(z\ t)=i\Delta_{pj}\beta_j(z\ t)+i\mathcal{E}_j(z\ t)+ig(z\ t)\overline{\Omega}_{cj} \tag{3.8a}$$

$$_tg(z\ t)=i\ \ \overline{\Omega}^*_{c1}\beta_1(z\ t)+\overline{\Omega}^*_{c2}\beta_2(z\ t)\ \ -\gamma_{13}g(z\ t) \tag{3.8b}$$

where we have added phenomenologically the ground states decoherence γ_{13} in Eq. (3.8b) and the spontaneous emission from the excited level γ_2 in Eqs. (3.8a) through the complex detuning $\Delta_{pj}=\delta_{pj}-i\gamma_2\ \ 2$, being $\delta_{pj}=\ \overset{0}{}_{pj}-\ \ _2$. Moreover, we have defined $\overline{\Omega}_{cj}=\Omega_{cj}e^{i\omega_j}$, we have assumed degenerate ground states, *i.e.*, $_1=\ \ _3$ and $\overset{0}{}_{pj}=\ \overset{0}{}_{cj}$, and we have chosen the energy origin at $\ \ _1=0$.

3.3 Solutions of the evolution equations

The equations describing the propagation of the single photon frequency components in the double-Λ system can be solved by using the adiabatic approximation for Eqs. (3.8a), *i.e.*, $_t\beta_j(z\ t)\ \ \ 0$, and changing from temporal to frequency domain by applying the Fourier transform to our system equations. Next, inserting Eqs. (3.8a) and (3.8b) into the Fourier transformed Eqs. (3.7), a linear system of partial differential equations for the quantum field amplitudes in the frequency domain, $\mathcal{E}_j(z\ \ \ )$, is obtained. This can be solved, leading to

$$\begin{aligned}\mathcal{E}_j(z\ \ \ )=&\mathcal{E}_j(0\ \ \ )\frac{\Omega_{cj}\ ^2}{\Omega\ ^2}\ \ e^{i\ z\ v_a}+\frac{\Omega_{cl}\ ^2}{\Omega_{cj}\ ^2}e^{i\ z\ v_b}e^{i\alpha z}\\&+\mathcal{E}_l(0\ \ \ )\frac{\overline{\Omega}_{cj}\overline{\Omega}^*_{cl}}{\Omega\ ^2}\left(e^{i\ z\ v_a}-e^{i\ z\ v_b}e^{i\alpha z}\right)\end{aligned} \tag{3.9}$$

where $j\ l = \ 1\ 2\ $ and $j = l$, $\mathcal{E}_j(0\ \ )$ is the boundary condition for the spectral envelope of the frequency component centered at $\ {}^{0}_{pj}$, $\alpha = -\kappa_{12}\frac{\Omega^{\ 2}}{D}$ and

$$\frac{1}{v_a} = \frac{1}{c} + \frac{\kappa_{12}}{\Omega^{\ 2}} \tag{3.10a}$$

$$\frac{1}{v_b} = \frac{1}{c} + \frac{\kappa_{12}}{\Omega^{\ 2}} \frac{\Omega_{c1}{}^{\ 2}\ \Omega_{c2}{}^{\ 2}\left(\Delta_{p1} - \Delta_{p2}\right)^2}{D^2} \tag{3.10b}$$

with $D = \Delta_{p1}\ \Omega_{c2}{}^{\ 2} + \Delta_{p2}\ \Omega_{c1}{}^{\ 2}$ and $\Omega^{\ 2} = \ \Omega_{c1}{}^{\ 2} + \ \Omega_{c2}{}^{\ 2}$. In Eqs. (3.9), we have assumed that the decoherence time of the ground states is much larger than the time needed to store and retrieve the single photon, thus $\gamma_{13}\quad 0$. Moreover, we have approximated the exponents as linear functions of by Taylor expansion up to first order, and we have considered the coefficients independent of , as done in Ref. [163]. With these approximations, and assuming a small decay rate from the excited level

$$\gamma_2 \ll \frac{\delta_{p1}\ \Omega_{c2}{}^{\ 2} + \delta_{p2}\ \Omega_{c1}{}^{\ 2}}{\Omega^{\ 2}} \tag{3.11}$$

the inverse Fourier transform of the field can be performed analytically. Then, it can be seen that in general each of the components of the frequency superposition will split in two different parts, each one propagating with a different velocity given by Eqs. (3.10a) and (3.10b).

However, by imposing that Eqs. (3.10a) and (3.10b) must be equal, and taking into account Eq. (3.11), the conditions for having equal propagation velocities for the two components can be obtained:

$$\frac{\delta_{p1}}{\delta_{p2}} = \pm\frac{\Omega_{c1}}{\Omega_{c2}}\left(\frac{\Omega_{c1}\ +\ \Omega_{c2}}{\Omega_{c1}\ -\ \Omega_{c2}}\right)^{\pm 1} \tag{3.12}$$

Any combination of the parameters satisfying either the positive or the negative case will lead to $v_a = v_b \equiv v$. Choosing for the sake of definiteness the negative case, and taking for simplicity $\Omega_{c1}\ =\ \Omega_{c2}$, we must satisfy $\delta_{p1} = 0$ and, from Eq. (3.11), $\delta_{p2} - \ \gamma_2$ to have equal propagation velocities. Therefore, the inverse Fourier transforms of Eqs. (3.9) can be written as

$$\mathcal{E}_j(z\ t) = \frac{1}{2}\ \mathcal{E}_j\left(0\ t - \frac{z}{v}\right)\left(1 + e^{i\alpha z}\right) + \mathcal{E}_l\left(0\ t - \frac{z}{v}\right)e^{i\omega_{jl}}\left(1 - e^{i\alpha z}\right) \tag{3.13}$$

where $\pi_{jl} \equiv \pi_j - \pi_l$ is the phase difference between the coupling fields. Note that

α now reduces to $\alpha \quad -2\frac{\kappa_{12}}{\delta_{p2}} + i\kappa_{12}\frac{2\gamma_2}{\delta_{p2}^2}$[1].

To obtain the intensity of each component of the single photon frequency superposition we calculate $\mathcal{E}_j(z\ t)\mathcal{E}_j^*(z\ t)$ using Eqs. (3.13):

$$\begin{aligned}\mathcal{E}_j(z\ t)\ ^2 =& \frac{1}{4}\Bigg[\left|\mathcal{E}_j^0\left(t-\frac{z}{v}\right)\right|^2 \quad 1+e^{-2\mathrm{Im}(\alpha)z}+2\cos\left[\mathrm{Re}(\alpha)z\right]e^{-\mathrm{Im}(\alpha)z} \\ &+\left|\mathcal{E}_l^0\left(t-\frac{z}{v}\right)\right|^2 \quad 1+e^{-2\mathrm{Im}(\alpha)z}-2\cos\left[\mathrm{Re}(\alpha)z\right]e^{-\mathrm{Im}(\alpha)z} \\ &+2\mathrm{Re}\left(\left|\mathcal{E}_l^0\left(t-\frac{z}{v}\right)\right|\left|\mathcal{E}_j^0\left(t-\frac{z}{v}\right)\right|e^{i\ _{jl}}e^{i\omega_{jl}}\right. \\ &\left.\times \quad 1-e^{-2\mathrm{Im}(\alpha)z}+2i\sin\left[\mathrm{Re}(\alpha)z\right]e^{-\mathrm{Im}(\alpha)z}\ \right)\Bigg] \end{aligned} \tag{3.14}$$

where $_{jl} = \ _j - \ _l$ is the phase difference between the single photon frequency components at the input $z = 0$. In Eqs. (3.14) the time evolution appears only in the boundary conditions $\mathcal{E}_j^0\left(t-\frac{z}{v}\right) \equiv \mathcal{E}_j(0\ t-\frac{z}{v})$. This means that the single photon wave packet keeps its shape but it is drifted in time a quantity $t_c = z\ v$, which depends on the velocity v defined in Eq. (3.10a). Moreover, it can be seen that, while the single photon propagates, the intensities of the two frequency components exhibit complementary oscillations with a rate that depends on $\mathrm{Re}(\alpha)$. Note that the decaying terms $\mathrm{Im}(\alpha)$ in Eqs. (3.14) are due to spontaneous emission from the excited level. An interesting case is found when one considers a symmetric superposition state at the input, *i.e.*, $\left|\mathcal{E}_j^0(t)\right| = \left|\mathcal{E}_l^0(t)\right|$. In this situation, Eqs. (3.14) takes the form

$$\begin{aligned}\mathcal{E}_j(z\ t)\ ^2 =& \left|\mathcal{E}_j^0\left(t-\frac{z}{v}\right)\right|^2 \quad \frac{1+e^{-2\mathrm{Im}(\alpha)z}}{2}+\quad \cos\left(\pi_{jl}+\ _{jl}\right) \quad \frac{1-e^{-2\mathrm{Im}(\alpha)z}}{2} \\ &-\sin\left(\pi_{jl}+\ _{jl}\right)\sin\left[\mathrm{Re}(\alpha)z\right]e^{-\mathrm{Im}(\alpha)z}\ \Bigg)\end{aligned} \tag{3.15}$$

In this case, when $\pi_{jl}+\ _{jl} = 0$, there is no oscillation between the frequency components during the propagation and the intensity of each single photon frequency component is perfectly transmitted, *i.e.*, $\mathcal{E}_j(z\ t)\ ^2 = \left|\mathcal{E}_j^0\left(t-\frac{z}{v}\right)\right|^2$. This can be interpreted by considering that, through a four-wave mixing process mediated by the coupling beams, the energy going from the first to the second component is compensated by the energy transfer from the second component to the first one.

Analogously, we find the relative phase between the two frequency components

[1]It is worth noting that within this approximation the pulse loosely couples to the atomic transitions at variance with what occurs in a standard EIT configuration. The numerical analysis in Sec. 3.4 is carried out within this limit.

using

$$\begin{aligned}\mathcal{E}_j(z\ t)\mathcal{E}_l^*(z\ t) = &\left|\mathcal{E}_j^0\left(t-\frac{z}{v}\right)\right|\left|\mathcal{E}_l^0\left(t-\frac{z}{v}\right)\right| \quad \cos(\ _{jl}-\pi_{jl})\,\frac{1+e^{-2\mathrm{Im}(\alpha)z}}{2}\\ &+i\sin(\ _{jl}-\pi_{jl})\,e^{-\mathrm{Im}(\alpha)z}\cos\left[\mathrm{Re}(\alpha)z\right]\\ &+i\sin\left[\mathrm{Re}(\alpha)z\right]e^{-\mathrm{Im}(\alpha)z}\frac{\left|\mathcal{E}_j^0\left(t-\frac{z}{v}\right)\right|^2-\left|\mathcal{E}_l^0\left(t-\frac{z}{v}\right)\right|^2}{2}\\ &+\frac{1-e^{-2\mathrm{Im}(\alpha)z}}{2}\frac{\left|\mathcal{E}_j^0\left(t-\frac{z}{v}\right)\right|^2+\left|\mathcal{E}_l^0\left(t-\frac{z}{v}\right)\right|^2}{2} \quad e^{i\omega_{jl}}\end{aligned} \tag{3.16}$$

From this expression, we observe that in general the phase between the two components, $\arg\left[\mathcal{E}_j(z\ t)\mathcal{E}_l^*(z\ t)\right]$, will oscillate in a more involved way than the intensity, Eqs. (3.14). In particular, we observe that only when the imaginary part of the outermost parenthesis in Eq. (3.16) vanishes the phase will be independent of z.

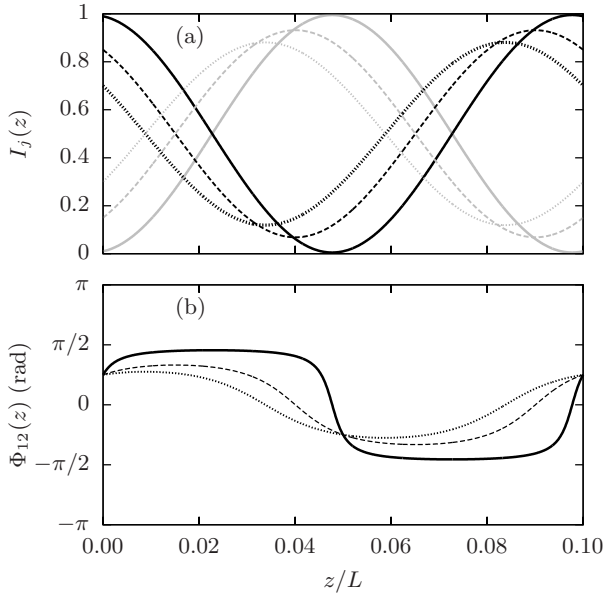

Figure 3.2: (a) Normalized intensities of the single photon frequency components I_1 (black) and I_2 (gray), and (b) the relative phase between them for $\mathrm{Re}(\alpha) = 2\nu\ L$, with $L = 0\ 1$ (a.u.) being the length of the medium, and $\mathrm{Im}(\alpha) = 0$. Solid lines: $I_1(0) = 0\ 99$, $\pi_{12} = 0$, $_{12} = \nu\ 4$; Dashed lines: $I_1(0) = 0\ 85$, $\pi_{12} = 0$, $_{12} = \nu\ 4$; Dotted lines: $I_1(0) = 0\ 70$, $\pi_{12} = 0$, $_{12} = \nu\ 4$.

In what follows, by evaluating the analytical expressions obtained in Eqs. (3.14)

and (3.16), we discuss different propagation examples of the two frequency components, see Figs. 3.2 and 3.3. We change to a reference frame fixed at the peak of the single photon pulse ($t_c = z\ v$), so we need only to show the variation on the spatial dimension z. In Figs. 3.2(a) and 3.3(a) we plot the normalized intensity of each of the two frequency components,

$$I_j(z) = \frac{\mathcal{E}_j(z\ t_c)^{\,2}}{\left|\mathcal{E}_1^0(t_c)\right|^2 + \left|\mathcal{E}_2^0(t_c)\right|^2} \tag{3.17}$$

whereas in Figs. 3.2(b) and 3.3(b), the relative phase between them,

$$\Phi_{jl}(z) = \arg\left[\mathcal{E}_j(z\ t_c)\mathcal{E}_l^*(z\ t_c)\right] \tag{3.18}$$

is shown. In all the figures the different line styles correspond to different sets of parameters (see the caption), while the black and gray lines both in Figs. 3.2(a) and 3.3(a) correspond to the intensity of the frequency components $\overset{0}{}_{p1}$ and $\overset{0}{}_{p2}$, respectively. We have taken $\mathrm{Im}(\alpha) = 0$, fact that is well justified from the assumption $\delta_{p2} - \gamma_2$ made in Eqs. (3.13). These figures are useful to show that the behavior of the two components during the propagation depends completely on the specific state at the entrance of the medium and the phase difference of the coupling beams. For example, the different line styles in Fig. 3.2 correspond to different initial intensities of the frequency components, while the relative phases between the frequency components and coupling beams are fixed. We observe that the different initial superposition states lead to intensity oscillations with different amplitudes and shifted by different amounts. Further examples are shown in Fig. 3.3, where the input intensities are equal for the two frequency modes, and the relative phases between them and between the coupling beams are changed. We observe in Fig. 3.3(a) that opposite behaviors for the intensity of a given mode are obtained just by properly changing the relative phase of the coupling beams (solid and dashed lines). Moreover, note that the case shown with dotted lines, *i.e.*, $I_{p1}(0) = I_{p2}(0)$ and $\pi_{12} = \ _{12} = 0$, corresponds to the situation discussed after Eqs. (3.15), in which the photon state does not evolve during propagation.

As a general conclusion from Figs. 3.2 and 3.3, we observe that the more different the intensities of the frequency components, the largest the variation in their relative phase, and vice versa. We also observe that the relative phase oscillates around the value π_{ij}. The coherent evolution of the two frequency components allow for a certain degree of engineering of the single photon state. For instance,

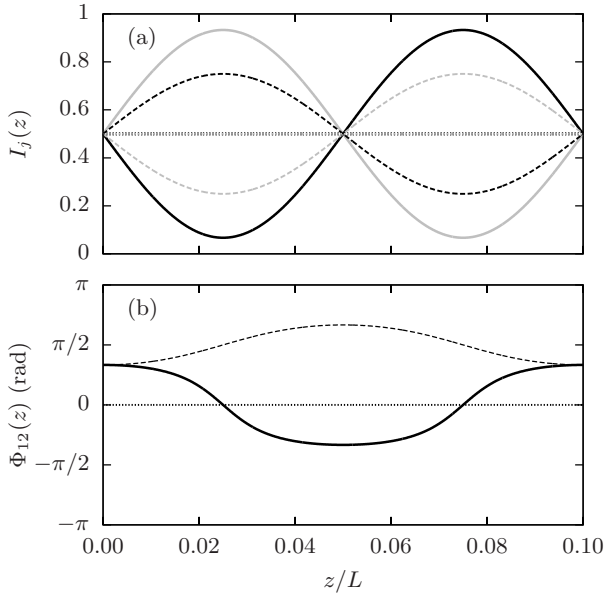

Figure 3.3: (a) Normalized intensities of the single photon frequency components I_1 (black) and I_2 (gray), and (b) the relative phase between them for $\mathrm{Re}(\alpha) = 2\nu\ L$, with $L = 0\ 1$ (a.u.) being the length of the medium, and $\mathrm{Im}(\alpha) = 0$. Solid lines: $I_1(0) = 0\ 5$, $\pi_{12} = 0$, $_{12} = \nu\ 3$; Dashed lines: $I_1(0) = 0\ 5$, $\pi_{12} = \nu\ 2$, $_{12} = \nu\ 3$; Dotted lines: $I_1(0) = 0\ 5$, $\pi_{12} = 0$, $_{12} = 0$.

by choosing $\mathrm{Re}(\alpha)L$ being even multiples of ν and $\pi_{12} = 0$, the frequency components of the superposition state can be swapped, or by choosing a different π_{12}, a desired phase between them can be added. Moreover, the most remarkable fact is that the frequency of the oscillation, both in the intensites, Eqs. (3.17), and in the phase, Eqs. (3.18), is determined only by $\mathrm{Re}(\alpha)\quad -2\kappa_{12}\ \delta_{p2}$. This means that by properly choosing the coupling parameter κ_{12} and the detuning δ_{p2}, one can recover at the output of the medium, $z = L$, the initially injected state with an ideally perfect fidelity, *i.e.*, $\mathcal{E}_j(L\ t) = \mathcal{E}_j^0(t - t_c)$ for $\mathrm{Re}(\alpha)L = 2\nu n$, with $n\quad \mathbb{Z}$.

3.4 Numerical analysis

In this Section, we demonstrate the validity of the approximations made in the analytical approach by numerically integrating Eqs. (3.7)-(3.8). Moreover, we show the possibility of storing and retrieving a single photon in an arbitrary superposition state of two frequency components using time dependent coupling fields. To simulate the pulse propagation in time and space, a bidimensional grid for each

variable is created with a spacing in the z dimension small enough to ensure the convergence of the results. The steps for the numerical protocol are the following: First, the temporal evolution of the medium variables is obtained from the incident ($z = 0$) field components, which are assumed to have Gaussian profiles of temporal width $^{\rightarrow} = 25$ ns and centered at $t_c = 3\ 5^{\rightarrow}$, using a Runge-Kutta integrating method. Next, the field at the adjacent spatial point is determined with a finite difference method, using the preceding obtained values. Finally the previous steps are repeatedly performed until the whole grid is filled. For the medium we take a length of $L = 0\ 1$ m, $\gamma_2{}^{\rightarrow} = 0\ 16$, $\gamma_{13}{}^{\rightarrow} = 1\ 6 \times 10^{-5}$, and $\kappa_{12}{}^{\rightarrow} L \quad 500$, while the detunings are $\delta_{p1}{}^{\rightarrow} = 0$ and $\delta_{p2}{}^{\rightarrow} = 160$.

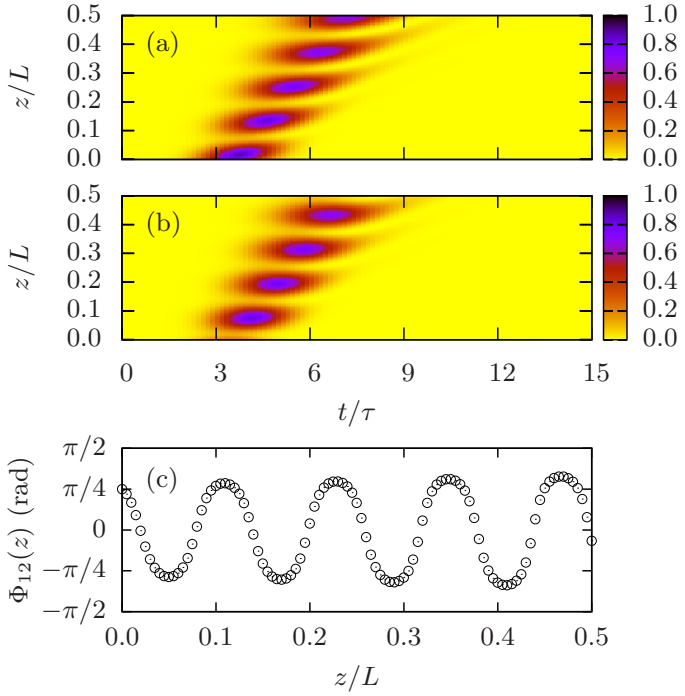

Figure 3.4: Normalized intensities of the single pulse frequency components, I_1 (a) and I_2 (b), as a function of normalized position and time, and (c) the phase between the frequency components at the pulse peak as a function of normalized position. The parameters correspond to the case represented with dotted lines in Fig. 3.2.

On the one hand, an example of the propagation of the two single photon frequency components is shown in Fig. 3.4, where the normalized intensity of both components, I_1 (a) and I_2 (b), is shown as a function of position and time for constant coupling Rabi frequencies $\left|\overline{\Omega}_{cj}\right|^{\rightarrow} = \left|\overline{\Omega}_{cl}\right|^{\rightarrow} = 18$, and a phase between

them of $\pi_{12} = 0$. The peak amplitudes of the frequency components for the injected single photon are $\left|\mathcal{E}_1^0(t_c)\right|^{\rightarrow} = 1\,3\times10^{-3}$ and $\left|\mathcal{E}_2^0(t_c)\right| = \overline{0\,3\;\;0\,7}\left|\mathcal{E}_1^0(t_c)\right|$, with a relative phase $_{12} = \nu\;4$ between them. Note that those parameters correspond to the case represented in Fig. 3.2 with dotted lines. As we observe, the intensities for the two frequency components exhibit complementary oscillations with a spatial period of $\sim 0\,125L$. Moreover, the displacement of the peak allows to estimate a propagation velocity of $\sim 10^6$ m/s. Using the model derived in the previous Section 3.3, the values obtained for the oscillation period and the velocity are $\sim 0\,1L$ and $\sim 4\,5\times10^6$ m/s, respectively. Thus, the numerical simulations are in good agreement with the analytical results. The phase between the components at the peak of the pulse, $\Phi_{jl}(z)$, is plotted in Fig. 3.4(c) as a function of z. We observe that the behavior of the phase is also in good agreement with the analytical result [see dotted line in Fig. 3.2(b)].

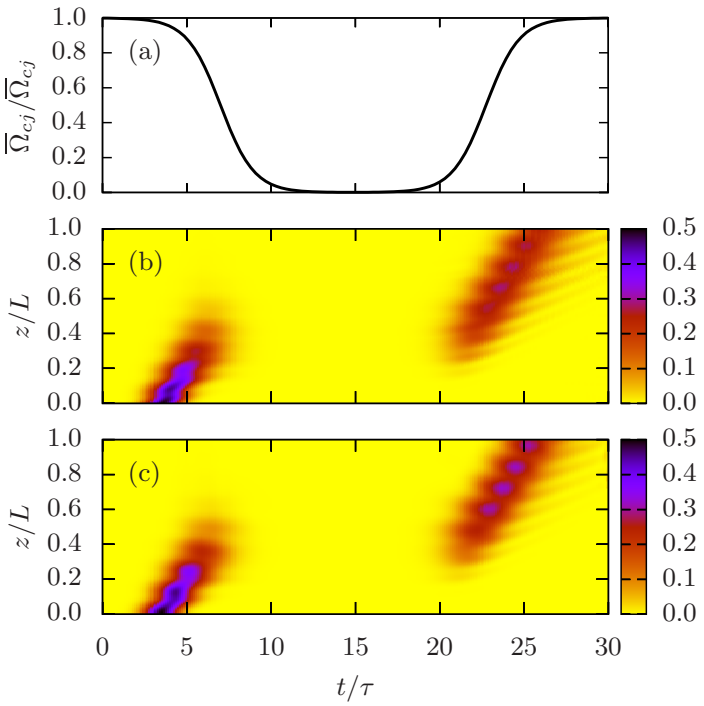

Figure 3.5: Temporal profile of the coupling beams (a) and normalized intensities of the single pulse frequency components, I_1 (b) and I_2 (c), as a function of normalized position and time. The parameters correspond to the case represented with dotted lines in Fig. 3.3.

On the other hand, Fig. 3.5 shows a particular example of the storage and

retrieval process, using temporal profiles of the coupling beams of the form

$$\overline{\Omega}_{cj}(t) = \frac{\overline{\Omega}_{cj}}{2} \; 2 - \tanh\left[\phi(t-t_1)\right] + \tanh\left[\phi(t-t_2)\right] \tag{3.19}$$

with $\left|\overline{\Omega}_{c1}\right| \rightarrow = \left|\overline{\Omega}_{c2}\right| \rightarrow = 18$, $\phi = 0\ 5 \rightarrow^{-1}$, $t_1 = 2t_c$ and $t_2 = 6t_c$ [see Fig. 3.5(a)], and a phase difference between the coupling fields of $\pi_{12} = 0$. In Figs. 3.5(b) and (c) the normalized intensity of frequency components I_1 and I_2, respectively, is shown as a function of position and time. In the example, we have taken equal amplitudes for the two components of the input state, $\left|\mathcal{E}_1^0(t_c)\right| \rightarrow = \left|\mathcal{E}_2^0(t_c)\right| \rightarrow = 1\ 3\times10^{-3}$, and an initial phase difference $_{12} = 0$ between them, in such a way that the chosen parameters correspond to the situation with constant coupling fields represented with dotted lines in Fig. 3.3. Fig. 3.5 shows an example on how the superposition state can be stored and recovered by appropriately varying in time the coupling fields. Here, the storage time corresponds approximately to $t_2 - t_1 = 0\ 35\,\mu$s, and it could be extended in principle to times of the order of $1\ \gamma_{13}$ ($\sim 1\ 5$ ms for the parameters considered). The behavior of the intensities for each component coincides with the predictions of the theoretical model. We have checked that the total pulse area is almost conserved although the pulse spreads during propagation. The phase between the frequency components (not shown in the figure) keeps an approximately constant value of $\Phi_{jl}(z) = 0$ during the whole storage and retrieval process, as expected from the dotted line in Fig. 3.3(b). To characterize the memory performance, the efficiency of the storage and the retrieval processes, and the fidelity of the recovered superposition state have been calculated. On the one hand, we define the performance efficiency as $\eta = \eta_{\rm Abs}\eta_{\rm Ret}$, with the absorption $\eta_{\rm Abs}$ and retrieval $\eta_{\rm Ret}$ efficiencies being

$$\eta_{\rm Abs} = 1 - \frac{\int_{t_0}^{t_f\ 2}\left(\ \mathcal{E}_1(L\ t)\ ^2 + \ \mathcal{E}_2(L\ t)\ ^2\right)dt}{\int_{t_0}^{t_f\ 2}\left(\left|\mathcal{E}_1^0(t)\right|^2 + \left|\mathcal{E}_2^0(t)\right|^2\right)dt} \tag{3.20a}$$

$$\eta_{\rm Ret} = \frac{\int_{t_f}^{t_f\ 2}\left(\ \mathcal{E}_1(L\ t)\ ^2 + \ \mathcal{E}_2(L\ t)\ ^2\right)dt}{\int_{t_0}^{t_f\ 2}\left(\left|\mathcal{E}_1^0(t)\right|^2 + \left|\mathcal{E}_2^0(t)\right|^2\right)dt} \tag{3.20b}$$

where the interval $t_0 = 0$, $t_f = 30 \rightarrow$ is the integration time. Computing these expressions with the data obtained in the simulation shown in Fig. 3.5, the absorption and retrieval efficiencies are $\eta_{\rm Abs} = 99\ 78\%$ and $\eta_{\rm Ret} = 91\ 21\%$, respectively. Thus, the total efficiency is $\eta = 91\ 01\%$. On the other hand, the conditional fidelity is

defined as $F_c = \quad _{\text{in}} \quad _{\text{out}}^{\ 2}$, where we take as input and output states

$$
\begin{aligned}
_{\text{in}} =& \frac{\int_{t_0}^{t_f\ 2} \left|\mathcal{E}_1^0(t)\right|^2 dt}{\int_{t_0}^{t_f\ 2} \left(\left|\mathcal{E}_1^0(t)\right|^2 + \left|\mathcal{E}_2^0(t)\right|^2\right) dt}\ 1\ 0\ _p\ 1 \\
&+ e^{i\ \ _{12}^{\text{in}}} \frac{\int_{t_0}^{t_f\ 2} \left|\mathcal{E}_2^0(t)\right|^2 dt}{\int_{t_0}^{t_f\ 2} \left(\left|\mathcal{E}_1^0(t)\right|^2 + \left|\mathcal{E}_2^0(t)\right|^2\right) dt}\ 0\ 1\ _p\ 1 \qquad (3.21a) \\
_{\text{out}} =& \frac{\int_{t_f\ 2}^{t_f} \mathcal{E}_1(L\ t)^{\ 2} dt}{\int_{t_f\ 2}^{t_f} \left(\mathcal{E}_1(L\ t)^{\ 2} + \mathcal{E}_2(L\ t)^{\ 2}\right) dt}\ 1\ 0\ _p\ 1 \\
&+ e^{i\ \ _{12}^{\text{out}}} \frac{\int_{t_f\ 2}^{t_f} \mathcal{E}_2(L\ t)^{\ 2} dt}{\int_{t_f\ 2}^{t_f} \left(\mathcal{E}_1(L\ t)^{\ 2} + \mathcal{E}_2(L\ t)^{\ 2}\right) dt}\ 0\ 1\ _p\ 1 \qquad (3.21b)
\end{aligned}
$$

respectively, with

$$
\left\langle\ _{12}^{\text{in}}\right\rangle \equiv \int_{t_0}^{t_f} \arg\left[\mathcal{E}_1(0\ t)\mathcal{E}_2^*(0\ t)\right] dt \qquad (3.22a)
$$

$$
\left\langle\ _{12}^{\text{out}}\right\rangle \equiv \int_{t_f\ 2}^{t_f} \arg\left[\mathcal{E}_1(L\ t)\mathcal{E}_2^*(L\ t)\right] dt \qquad (3.22b)
$$

Therefore, the calculated conditional fidelity for the case shown in Fig. 3.5 is $F_c = 99\ 69\%$.

3.5 Conclusions

In this Chapter we have studied the propagation of a single photon, in an arbitrary superposition of two different frequency components, through a double-Λ medium. We have considered a configuration in which the strong control fields do not couple the populated ground state, and one of them is detuned far from the one photon resonance. This configuration has the peculiarity that the intensities of the two frequency components exhibit complementary periodic oscillations as they propagate. These propagation effects have been used in combination with the light storage technique based on EIT to implement a quantum memory for frequency encoded single photon qubits. We have derived the parameter conditions under which the two components propagate with the same velocity, and we have analytically studied the dependence of the relative phase between the coupling fields and the input qubit state in the propagation dynamics. Moreover, we have shown that

the initial state of the single photon, which can be any desired frequency superposition of the two frequency components, is recovered at certain positions in the medium The results obtained by numerically integrating the evolution equations of the system are in good agreement with the analytical solutions and thus the validity of the analytical approach has been confirmed. Finally, the storage and retrieval of a single photon state in an arbitrary superposition of two frequency components has been shown numerically by turning off and on the coupling fields during the propagation of the single photon. For the parameters used, the results demonstrate an efficient quantum memory for arbitrary frequency encoded single photon qubit with high fidelity.

4

Single-site addressing of ultracold atoms beyond the diffraction limit via position dependent adiabatic passage

The present Chapter is devoted to the study of a new proposal to perform single atom/single site addressing of ultracold atoms in an optical lattice. The proposal is based on the sub-wavelength localization via adiabatic passage (SLAP) technique [180], and has been accepted for publication recently in Phys. Rev. A. This subject offers a complementary aspect to the previous Chapters, based on quantum memories, within the context of quantum information with three-level atoms. While the first Chapters 2 and 3 are more focused in the transmission and storage of quantum information encoded in the state of light, the present Chapter deals with the manipulation of stationary qubits. In particular, we consider a sample of ultracold neutral atoms loaded into a two-dimensional optical lattice with one atom per site, each one modeled by a three-level Λ system in interaction with a pump and a Stokes laser pulse. Using a pump field with a node in its spatial profile and a proper overlap between the pump and Stokes fields, we show that the population of the atoms at all sites is transferred from one ground state of the system to the other via stimulated Raman adiabatic passage (STIRAP) [181], except the one at the position of the node, that remains in the initial ground state. This technique allows for the preparation, manipulation, and detection of atoms with a spatial resolution better than the diffraction limit, which either relaxes the requirements on the optical setup used or extends the achievable spatial resolution

to lattice spacings smaller than accessible to date. In comparison to techniques based on coherent population trapping [59, 160, 182, 183], SLAP gives a higher addressing resolution and has additional advantages such as robustness against parameter variations, coherence of the transfer process, and the absence of photon induced recoil. Additionally, the advantages of our proposal with respect to adiabatic spin-flip techniques [184, 185] are highlighted. Analytic expressions for the achievable addressing resolution and efficiency are derived and compared to numerical simulations for ^{87}Rb atoms in state-of-the-art optical lattices.

In Section 4.1 we provide a motivation for the development of novel single site/single atom addressing techniques and review previous works. Next, in Section 4.2, we introduce the physical system under consideration and describe the physical mechanism used to perform the addressing technique. In Section 4.3, the novel protocol to perform single site addressing is described, and analytical expressions for the spatial resolution and the addressing efficiency of our technique are derived. In addition, a comparison with CPT based techniques is provided. Next, in Section 4.4, we perform a numerical investigation of the proposed technique for a single-occupancy optical lattice loaded with ^{87}Rb atoms by integrating the corresponding atomic density-matrix equations. Finally, in Section 4.5, we summarize the results and present the conclusions.

4.1 Introduction

Ultracold neutral atoms in an optical lattice with single-atom/single-site resolution constitute an ideal physical system to investigate strongly correlated quantum phases [186] which, in turn, has interesting applications in quantum optics [187], quantum simulation [188] and quantum information processing [189 191], among others. The first approaches towards single-site addressing considered the use of lattices with relatively large site separations [192 197]. However, to have access to the regime of strongly correlated systems, typical lattice spacings well below $1\,\mu m$ are needed since the tunneling rate has to be comparable to the on site interactions. In this case, the diffraction limit imposes strong restrictions on the addressability of individual lattice sites. To overcome this limitation different techniques have been investigated. For instance, spatially dependent electric and magnetic fields have been used to induce position dependent energy shifts on the atom [198], allowing for site-selective addressability. Alternatively, a scanning electron microscopy system to remove atoms from individual sites with a focused

electron beam [199, 200] has been reported. However, in this case, atoms need to be reloaded into the emptied sites after each detection event. More recently, high resolution fluorescence imaging techniques, that make use of an optical system with high numerical aperture, have been implemented to perform *in situ* single-atom/single-site imaging for strongly correlated systems [201 205]. In this context, a single-site addressing (SSA) scheme based on focused laser beams inducing position-dependent energy shifts of hyperfine states has been theoretically [184] and experimentally reported [185]. In the experiment, an intense addressing beam is tightly focused by means of a high resolution optical system. This beam produces spatial dependent light shifts bringing the addressed atom into resonance with a chirped microwave pulse and eventually inducing a spin-flip between two different hyperfine levels of the atom.

On the other hand, during the last years, several proposals based on the interaction of spatially dependent fields, *e.g.*, standing waves, with three-level atoms in a Λ-type configuration have been considered, not only for single-site addressing in optical lattices but, more generally, for sub-wavelength resolution and localization [180, 206 213]. In the first approaches [206 213], a spatially modulated dark state is created by means of either electromagnetically induced transparency (EIT) [61] or coherent population trapping (CPT) [59, 160, 182, 183], which allows for a tight localization of the atomic population in one of the ground states, around the position of the nodes of the spatially dependent field. More recently, it has been shown that the resolution achieved with those CPT/EIT based techniques can be surpassed using stimulated Raman adiabatic passage (STIRAP) [181] processes, by means of the so-called Sub-wavelength Localization via Adiabatic Passage (SLAP) technique [180]. The SLAP technique relies on a position-dependent STIRAP of atoms between the two ground states of a three-level Λ atomic system, and has additional advantages compared with CPT/EIT techniques such as (i) robustness against parameter variations, (ii) coherence of the transfer process, that allows for its implementation also in Bose-Einstein condensates [180], and (iii) the absence of photon induced recoil.

In this Chapter, we apply the SLAP technique [180] to ultracold atoms in an optical lattice, where single-site addressing (SSA) requires to overcome the diffraction limit. In order to address only a single site, we use here Stokes and pump pulses with Gaussian shaped spatial distributions, with the pump presenting a node centered at the lattice site that we want to address. Assuming that all the atoms in the optical lattice are initially in the same internal ground state

and applying the standard STIRAP counterintuitive temporal sequence for the light pulses [181], we will demonstrate that it is possible to adiabatically transfer all the atoms, except the one at the node of the pump field, to an auxiliary ground state. We will show that this process is performed with higher efficiency and yields better spatial resolution than the CPT based techniques [206 213]. Also, we will demonstrate that our addressing technique requires shorter times than in the adiabatic spin-flip technique discussed in Ref. [185], and that larger addressing resolutions can be achieved using similar focusing of the addressing fields. Moreover, our technique has the additional advantage that it can be applied between two degenerated ground-state levels.

4.2 Physical model

The physical system under consideration, illustrated in Fig. 4.1(a), consists of a sample of ultracold neutral atoms loaded into a two-dimensional (2D) square optical lattice with spatial period λ 2, placed in the plane (x y), and illuminated by a pump and a Stokes laser pulse with Rabi frequencies Ω_P and Ω_S, respectively, propagating in the $-z$ direction with an adjustable time delay. The spatial profile of the pump pulse has a node coinciding with our target lattice site, at which the Stokes pulse is also centered. Since we consider the spatial profiles of the pulses having revolution symmetry around the propagation axis, represented by a dashed line in Fig. 4.1(a), in the following, and without loss of generality, we take into account only the transverse spatial dimension x. In our model, we assume the system to be in the Mott insulator regime with only one atom per lattice site. Each atom is considered to have only three relevant energy levels in a Λ-type configuration, defined by the interaction with the light pulses as shown in Fig. 4.1(b). Here, γ_{21} (γ_{23}) is the spontaneous transition rate from the excited state 2 to the ground state 1 (3) and Δ_P (Δ_S) is the detuning of the pump (Stokes) field. We assume that all atoms are initially in state 1 .

Our approach to achieve single site addressing is based on the SLAP technique [180], where, depending on their position, the atoms are transferred between two internal ground states by means of the STIRAP technique [181]. STIRAP consists in adiabatically following one of the energy eigenstates of the Λ-system, the so-called dark state, introduced in Eq. (2.27b), which under the two-photon resonance

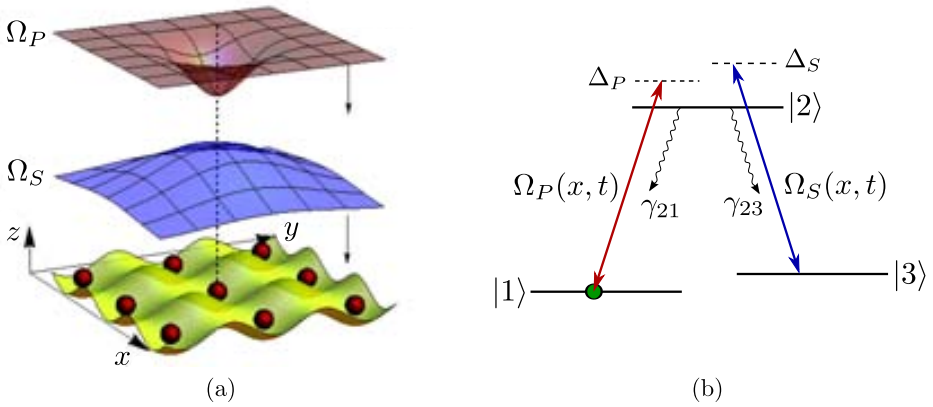

(a) (b)

Figure 4.1: (a) Physical system under investigation: The pump and Stokes light pulses, with Rabi frequencies Ω_P and Ω_S, propagate in the $-z$ direction and interact with the atoms of a single-occupancy optical lattice located in the $(x\ y)$ plane. (b) Scheme of the Λ-type three-level atoms, initially in state 1, that interact with pump and Stokes pulses. Excited level 2 has spontaneous transition rate γ_{21} (γ_{23}) to level 1 (3) and Δ_P (Δ_S) is the detuning of the pump (Stokes) field.

condition, *i.e.*, $\Delta_P = \Delta_S$, has the form

$$D(x\ t) = \cos\theta(x\ t)\ 1 - \sin\theta(x\ t)\ 3 \tag{4.1}$$

where $\tan\theta(x\ t) = \Omega_P(x\ t)\ \Omega_S(x\ t)$. Starting with all the population in 1, it is possible to coherently transfer the atomic population to state 3 changing adiabatically θ from $0°$ to $90°$ by means of a convenient time sequence of the fields. This time sequence corresponds to apply first the Stokes pulse and with a certain temporal overlap, the pump pulse. Since the process involves one of the eigenstates of the system, the population transfer is robust under fluctuations of the parameter values if these are adiabatically changed and the system does not evolve near degenerate energy eigenvalues.

In the SLAP technique, the pump field has a spatial structure with nodes yielding state-selective localization at those positions where the adiabatic passage process does not occur, *i.e.*, those atoms placed at the nodes of the pump field remain in 1 while those interacting with both fields, pump and Stokes, are transferred to 3. For our purposes, we use the SLAP technique with a pump field having a single node at the position of the target site. Therefore, at the end of

the SLAP process the population of all atoms illuminated is transferred from 1 to 3 except for the one at the node of the pump field. The spatial and temporal profiles for pump and Stokes Rabi frequencies are given by

$$\Omega_P(x\ t) = \Omega_{P0}(1 - e^{-x^2\ w_P^2})\, e^{-(t-t_P)^2\ 2\sigma^2} \tag{4.2a}$$

$$\Omega_S(x\ t) = \Omega_{S0}\, e^{-x^2\ w_S^2}\, e^{-(t-t_S)^2\ 2\sigma^2} \tag{4.2b}$$

where Ω_{P0} and Ω_{S0} are the peak Rabi frequencies, t_P and t_S are the centers of the temporal Gaussian profiles, w_P and w_S are the spatial widths of the node in the pump and of the Stokes field, respectively, and ϕ is the temporal width.

There exist several methods to create the required pump intensity profile with a central node: e.g. (i) re-imaging of a Gaussian beam with a dark central spot created by a circular absorption mask, using (ii) a Laguerre-Gaussian laser beam [214] or (iii) a *'bottle beam'* created by the interferometric overlap of two Gaussian beams with differing waists [215], or (iv) a flexible intensity patterns generated by spatial light modulators and subsequent imaging [216, 217].

4.3 Single-site addressing protocol

In our model, we assume that the spatial wavefunctions of the individual atoms placed at the different sites, centered at x_n (being n the site index), correspond to the ground state of the trapping potential, which in first approximation can be considered harmonic. Therefore, the full atomic distribution in the lattice is given, initially, by

$$\varphi_{\rm lat}(x) = \frac{1}{w_{\rm at}\ \ \overline{\overline{\nu}}}\ \ _n\ \exp\left[-\frac{(x-x_n)^2}{w_{\rm at}^2}\right] \tag{4.3}$$

where $w_{\rm at} =$ $\overline{\qquad m\qquad}$ is the width of the initial atomic distribution at an individual site, m is the mass of the trapped atom and is the harmonic trapping frequency. We assume that the addressed site is $x_0 = 0$ and their nearest neighbors $x_{\pm 1}$ are at a distance $\pm\lambda\ 2$ where λ is the wavelength of the fields that create the optical lattice.

In order to characterize our single-site addressing technique we consider that, once the SLAP technique has been applied, the final atomic population distribu-

tion in 1 , $\varphi_1^{\mathrm{SLAP}}(x)$, is given by

$$\varphi_1^{\mathrm{SLAP}}(x) = P_1^{\mathrm{SLAP}}{}_1(x)\varphi_{\mathrm{lat}}(x) \tag{4.4}$$

where $P_1^{\mathrm{SLAP}}{}_1(x)$ is the probability distribution that an atom remains in state 1 after the SLAP process. Using the SLAP technique, the addressing resolution that one can obtain is related to the global adiabaticity condition [181] at each spatial position x,

$$\left(\Omega_{S0}e^{-x^2\ w_S^2}\right)^2 + \ \Omega_{P0}\left(1 - e^{-x^2\ w_P^2}\right)^{\ 2} \geq \left(\frac{A}{T}\right)^2 \tag{4.5}$$

where $T = t_P - t_S$ and A is a dimensionless constant that, for optimal Gaussian temporal profiles and overlapping times, takes values around 10 [181]. Although usually the value $A \sim 10$ is accepted, we have found that $A = 20$ gives a more accurate description for the values of ϕ and R considered along this Chapter. In Eq. (4.5), the equality gives a spatial threshold x_{th} above which the adiabaticity condition is fulfilled. Assuming that the full width at half maximum (FWHM) of $P_1^{\mathrm{SLAP}}{}_1(x)$ is $(\Delta x)_{\mathrm{SLAP}} \sim x_{th}$ and expanding Eq. (4.5) up to first order in x one obtains

$$(\Delta x)_{\mathrm{SLAP}} = w_S \quad \frac{\overline{1 + \quad \overline{(R\ +1)\left(\frac{A}{T\Omega_{S0}}\right)^2 - R}}}{R\ +1} \tag{4.6}$$

where $R \ \equiv R\, w_S^4\ w_P^4$ and $R \equiv (\Omega_{P0}\ \Omega_{S0})^2$. Eq. (4.6) gives the width of the addressing region, and it tends to zero as R increases. Moreover, since $(\Delta x)_{\mathrm{SLAP}}$ must be real valued, we find that the inequality

$$\Omega_{S0}T < A \quad \overline{\frac{1+R}{R}} \tag{4.7}$$

must be fulfilled. Along this Chapter we will consider that Ω_{S0} is fixed, so R can be varied through $\Omega_{P0}\ w_P$ and w_S.

Two conditions should be satisfied for our SSA technique to work. First, the population of the atom in the addressed site must remain in state 1 after the action of the fields, and second, the rest of the atoms of the lattice have to be transferred to level 3 . Therefore, taking into account the overlap between $P_1^{\mathrm{SLAP}}{}_1(x)$ and $\varphi_{\mathrm{lat}}(x)$ in Eq. (4.4), it is clear that the FWHM of the probability

distribution $P_1^{\mathrm{SLAP}}{}_1(x)$ should satisfy

$$(\Delta x)_{\mathrm{at}} < (\Delta x)_{\mathrm{SLAP}} < x_1 - (\Delta x)_{\mathrm{at}} \tag{4.8}$$

where $(\Delta x)_{\mathrm{at}} = 2 \quad \overline{\ln 2}\, w_{\mathrm{at}}$, and $x_1 = \lambda \ 2$ is the position of the nearest neighboring site. Using Eq. (4.6), it is easy to see that these conditions fix the range for $\Omega_{S0}T$ to obtain SSA using the SLAP technique:

$$A\,\zeta_- < \Omega_{S0}T < A\,\zeta_+ \tag{4.9}$$

where

$$\zeta_\pm = \frac{1+R}{\left[(1+R)\left(\frac{x_\pm}{w_S}\right)^2 - 1\right]^2 + R} \tag{4.10}$$

with $x_+ = (\Delta x)_{\mathrm{at}}$ and $x_- = x_1 - (\Delta x)_{\mathrm{at}}$. Note that the upper limit for Eq. (4.9) is more restrictive than Eq. (4.7).

In order to have a quantitative description of the SSA performance, let us introduce the SSA efficiency as

$$\eta \equiv \mathcal{P}_{x_0}\,(1 - \mathcal{P}_{x_1}) \tag{4.11}$$

where $\mathcal{P}_{x_0}$ corresponds to the probability of finding the atom at the addressed site x_0 in state 1 , while $1 - \mathcal{P}_{x_1}$ corresponds to the probability that the atom in the neighbor site x_1 has been transferred to a different internal state. We define

$$\mathcal{P}_{x_i}^{\mathrm{SLAP}} \equiv \frac{\int_{-s}^{+s} \varphi_1^{\mathrm{SLAP}}(x)dx}{\int_{-s}^{+s} \varphi_{\mathrm{at}}(x)dx} \tag{4.12}$$

with $\pm s = x_i \pm \lambda \ 4$ and $i = 0 \ 1$, whereas $\varphi_1^{\mathrm{SLAP}}(x)$ and $\varphi_{\mathrm{at}}(x)$ have been defined in Eqs. (4.4) and (4.3), respectively. Using Eqs. (4.3) and (4.4), the explicit forms for Eqs. (4.12) are

$$\mathcal{P}_{x_0}^{\mathrm{SLAP}} = \frac{(\Delta x)_{\mathrm{SLAP}}}{\overline{(\Delta x)_{\mathrm{SLAP}}^2 + (\Delta x)_{\mathrm{at}}^2}} \tag{4.13a}$$

$$\mathcal{P}_{x_1}^{\mathrm{SLAP}} = \mathcal{P}_{x_0}^{\mathrm{SLAP}}\, e^{-4\ln(2)\, x_1^2 \ \left[(\Delta x)_{\mathrm{SLAP}}^2 + (\Delta x)_{\mathrm{at}}^2\right]} \tag{4.13b}$$

From these expressions, it can be seen that, for $x_1 > (\Delta x)_{\mathrm{at}}$, the limits given by Eq. (4.8), *i.e.*, $(\Delta x)_{\mathrm{SLAP}} = (\Delta x)_{\mathrm{at}}$ and $(\Delta x)_{\mathrm{SLAP}} = x_1 - (\Delta x)_{\mathrm{at}}$, correspond to

SSA efficiencies of $\sim 0\ 70$ and $\sim 0\ 94$, respectively.

An alternative technique to perform atomic localization based on spatial dependent dark states is the coherent population trapping (CPT) technique [206]. In the CPT [160] technique the dark state is populated after several cycles of coherent excitation followed by spontaneous emission from 2 to the ground states. Note that, while CPT relies on spontaneous emission, the SLAP technique is fully coherent. Moreover, the latter provides higher resolution, as shown in Ref. [180], and does not suffer from recoil since the localized atoms have not interacted with light. In what follows, we compare the range of parameters necessary to perform SSA considering both SLAP and CPT techniques. Note that we focus our comparative analysis in the CPT technique, although similar results are obtained considering the method proposed in Ref. [213], where the spatial dependent dark state, $D(x\ t)$, is created via the STIRAP technique by switching off the fields before completing the transfer process.

In order to compare both techniques, we define the final population distribution in 1 using CPT as $\varphi_1^{\mathrm{CPT}}(x)$ in an analogous way as it has been done for the SLAP technique in Eq. (4.4). Then, the FWHM of the corresponding probability function $P_1{}_1^{\mathrm{CPT}}(x)$ is obtained by imposing that $1\ D(x\ t)\ ^2 = 1\ 2$ and $t_P = t_S$ in Eqs. (4.2):

$$(\Delta x)_{\mathrm{CPT}} = \frac{2w_S}{\sqrt{1 + \quad \overline{R}}} \tag{4.14}$$

Fixing the desired Δx and using Eqs. (4.6) and (**??**) for SLAP and CPT, respectively, the constrains for the relevant parameters for each technique can be obtained. For simplicity, we consider that the Stokes pulse parameters w_S and Ω_{S0} are fixed, and only the node width w_P and pump peak Rabi frequency Ω_{P0} can be varied. Note that, for the SLAP case, we have to fix also A and T.

Taking $\Delta x = \lambda\ 4$, half of the site separation, the required values for R and w_P are plotted in Fig. 4.2(a). To simultaneously illuminate a large number of sites, we use a large Stokes beam waist of $w_S = 32\,\lambda_L = 24\,\lambda$, where $\lambda_L = \frac{3}{4}\lambda$ is the wavelength of both pump and Stokes fields. We choose this ratio $\lambda_L = \frac{3}{4}\lambda$ in order to be consistent with the specific numerical values used in Section 4.4. The solid (dashed) line corresponds to the SLAP (CPT) case with the parameter values $\Omega_{S0}T = 19$ and $A = 20$. Although usually the value $A \sim 10$ is accepted, we have found that $A = 20$ gives a more accurate description for the values of ϕ and R considered here. As w_P decreases, in both SLAP and CPT cases, lower values of R are needed to reach the fixed resolution Δx, since the narrower the node of the

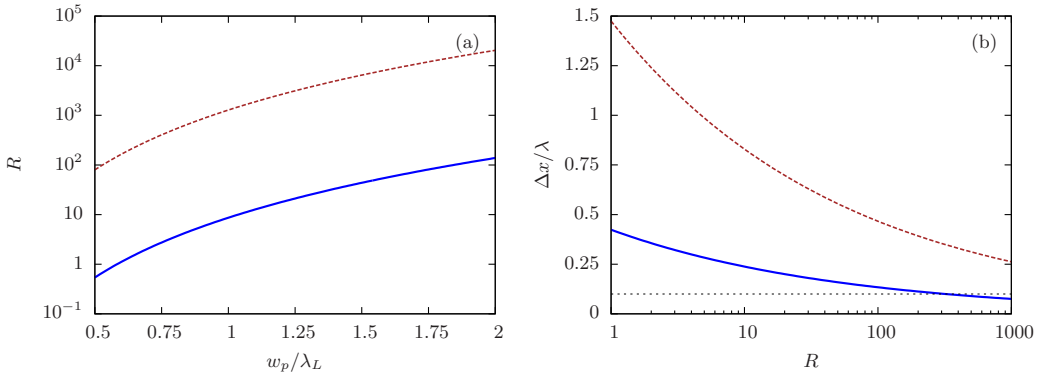

Figure 4.2: (a) Parameter values of R needed to perform SSA as a function of w_P, using SLAP (solid line) and CPT (dashed line) techniques. The addressing probability distribution widths are taken as $\Delta x = \lambda\ 4$ in both cases. (b) $(\Delta x)_{\rm SLAP}$ (solid line) and $(\Delta x)_{\rm CPT}$ (dashed line) as a function of R. The FWHM of the atomic distribution, $(\Delta x)_{\rm at} = \lambda\ 10$ corresponds to the horizontal dotted line and we have taken $w_P = \lambda_L$. The parameters used in both (a) and (b) are $w_S = 32\,\lambda_L = 24\,\lambda$, $\Omega_{S0}T = 19$ and $A = 20$.

pump field, the narrower the probability distribution of atoms remaining in 1 . In addition, for any given width of the node of the pump field w_P, the required values of R are lower in the SLAP case than in the CPT case.

It is important to realize that Eqs. (4.6) and (**??**) show the possibility to obtain, for certain parameter values, widths of the probability distribution, $(\Delta x)_{\rm SLAP}$ or $(\Delta x)_{\rm CPT}$, smaller than $(\Delta x)_{\rm at}$. In particular, using the SLAP technique this can be achieved with moderate R values. This is shown in Fig. 4.2(b), where $(\Delta x)_{\rm SLAP}$ (solid line) and $(\Delta x)_{\rm CPT}$ (dashed line) are represented as a function of R for $w_P = \lambda_L$ and the rest of parameters as in Fig. 4.2(a). The FWHM of the atomic distribution, $(\Delta x)_{\rm at} = \lambda\ 10$, is depicted with a horizontal dotted line to indicate the values where $(\Delta x)_{\rm SLAP} < (\Delta x)_{\rm at}$. As we stated in the discussion of Eqs. (4.13), this limit corresponds to a SSA efficiency of $\eta \sim 0\ 70$. This regime of parameters is interesting because it shows that the SLAP technique could be used for applications in site-selective imaging with a resolution down to the width of the atomic distribution at each site.

4.4 Numerical analysis

In this Section, by numerically integrating the corresponding density matrix equations, we study the implementation of the SLAP-based SSA technique for Λ-type

three-level ^{87}Rb atoms in a single-occupancy optical lattice. Numerical calculations using the CPT technique are also presented for comparison. The wavelength of the lasers that create the optical lattice, red detuned with respect to the D1 line of ^{87}Rb, is $\lambda = 1064$ nm. The potential depth of the optical lattice is chosen as $V_0 = 15E_r$, where E_r is the recoil energy. This corresponds to a harmonic trapping frequency of $= 2\nu \times 15\ 92$ kHz [188]. Therefore, the FWHM of the atom distribution at each site due to the confining potential is $(\Delta x)_{\rm at} = 142$ nm. Pump and Stokes fields with $\lambda_L = 795$ nm are coupled to 1 2 and 3 2, respectively, where $1 \equiv F = 2\ m_F = -2$, $2 \equiv F = 2\ m_F = -1$ and $3 \equiv F = 2\ m_F = 0$ are hyperfine energy levels of the D1 line of ^{87}Rb. The excited state 2 has a spontaneous transition rate $\gamma_{21} = 2\nu \times 0\ 96$ MHz ($\gamma_{23} = 2\nu \times 1\ 44$ MHz) to state 1 (3), and we assume no spin decoherence during the interaction time. We consider equal temporal pulse widths of $\phi = 0\ 2\,\mu$s with a temporal delay $T = 1\ 4\phi$, in such a way that the total SSA process time is 4ϕ. The Stokes pulse has a maximum Rabi frequency $\Omega_{S0} = 19\ T = 2\nu \times 10\ 8$ MHz, while the maximum Rabi frequency of the pump is varied through the parameter R, since $\Omega_{P0} = \Omega_{S0}\ \overline{R}$. Concerning the spatial profiles of the fields, we assume a wide Stokes profile, $w_S = 32\lambda_L$, and a narrow node for the pump, $w_P = \lambda_L$.

As it has been discussed in the previous Section 4.3, to properly perform SSA, the population of all the atoms in the lattice, except the one in the addressed site, must be transfered from 1 to 3 with high probability. In what follows, those requirements for the realization of the SSA are studied by numerically evaluating the SSA efficiency.

The signatures of SSA are shown in Fig. 4.3 where the numerically evaluated efficiency and probabilities defined in Eqs. (4.11) and (4.12) are plotted as a function of R for both the SLAP (circles) and CPT (crosses) techniques. Figs. 4.3(a) and 4.3(b) show the probabilities $\mathcal{P}_{x_0}$ and $1-\mathcal{P}_{x_1}$, respectively. For large values of R the probability of finding the atom at the addressed site in 1 is higher with the CPT than with the SLAP technique [see Fig. 4.3(a)], while for small values of R the probability of removing the atom from the neighboring site [see Fig. 4.3(b)] is higher in the SLAP case. This is explained by the fact that $(\Delta x)_{\rm SLAP} < (\Delta x)_{\rm CPT}$ for a given value of R, as it is shown in Fig. 4.2(b). The SSA efficiency results obtained by the numerical evaluation of Eqs. (4.11) and (4.12) are shown in Fig. 4.3(c), together with the corresponding analytical curves (solid and dashed lines) obtained using Eqs. (4.13), added for comparison. A good agreement is

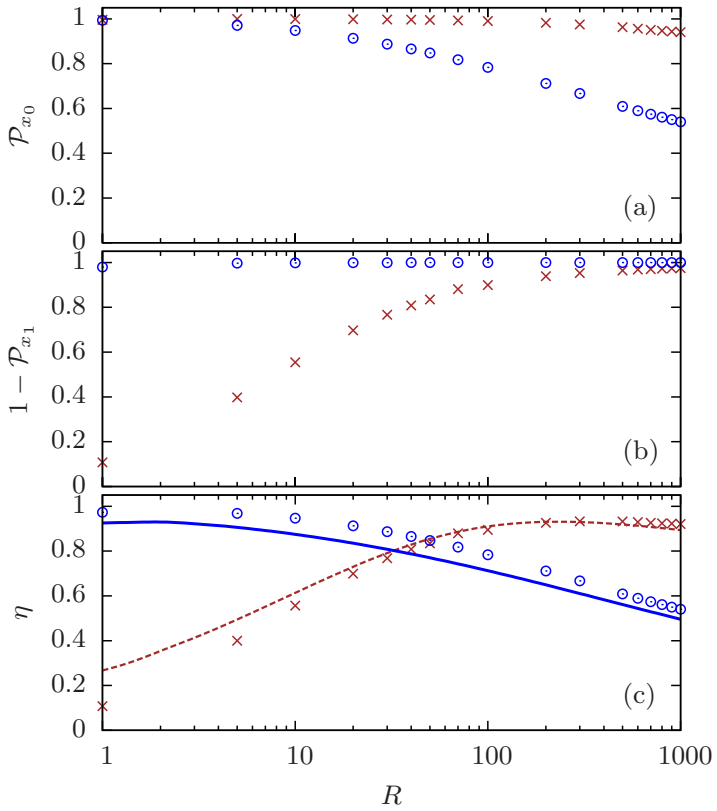

Figure 4.3: Numerical results for the probability of finding the atom located at x_0 in state 1 (a), the probability to transfer it from 1 to another state (b), and the efficiency η as a function of R (c), for the SSA with SLAP (circles) and CPT (crosses) techniques. Analytical curves for SLAP (solid line) and CPT (dashed lines), computed from Eqs. (4.11) and (4.12), are added in (c) for comparison (see text for the rest of parameters).

found between numerical and analytical results. From Fig. 4.3(c) it is clear that the SLAP technique is more efficient for lower values of the intensity ratio of the addressing fields ($R < 50$) than the CPT technique. Certainly, this is advantageous for the experimental implementation with limited laser power available.

Furthermore, an example of the spatial performance of the SSA using the SLAP and the CPT techniques is detailed in Figs. 4.4(a) and (b) for $R = 10$ and the rest of parameters as in Fig. 4.3. On the one hand, in Fig. 4.4(a) we plot the addressing probability distributions for the SLAP, $P_1^{\mathrm{SLAP}}{}_1(x)$, and CPT, $P_1^{\mathrm{CPT}}{}_1(x)$, techniques as a function of the position, with blue and red lines, respectively. Moreover, the pump and Stokes field profiles, $\Omega_P(x)$ and $\Omega_S(x)$, normalized to the pump

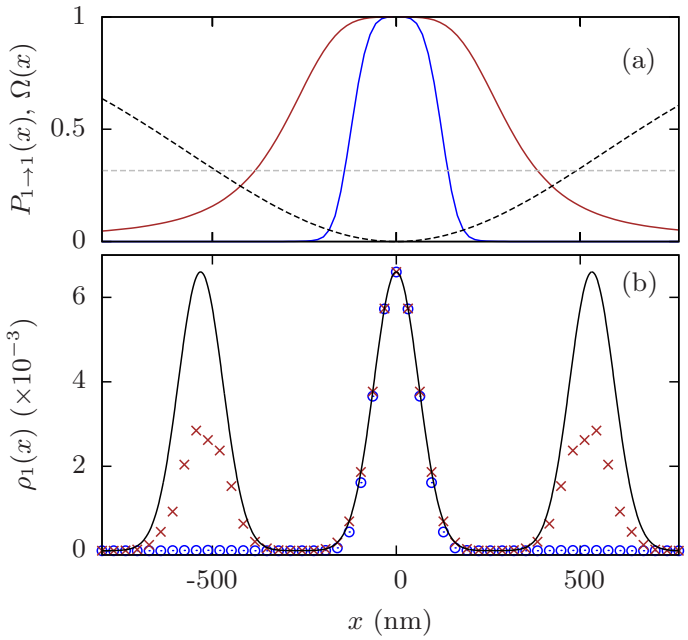

Figure 4.4: (a) Addressing probability distributions $P_{1\,1}^{\mathrm{SLAP}}(x)$ (blue line) and $P_{1\,1}^{\mathrm{CPT}}(x)$ (red line), using the SLAP and CPT techniques, respectively. The spatial profiles of the pump (black dashed line) and Stokes (gray dashed line) fields, normalized to the pump maximum Ω_{P0}, are also shown for comparison. (b) Final population distribution remaining in 1 using SLAP (circles) and CPT (crosses) single-site addressing techniques for $R = 10$. The initial atomic distribution in 1, $\varphi_{\mathrm{lat}}(x)$, is shown as solid line (see text for the parameters values).

maximum Ω_{P0}, are plotted with black and gray dashed lines, respectively. In this figure we observe that, first, the node of the pump profile is much wider than the two probability distributions, and second, the probability distribution using the SLAP technique is significantly narrower than the one using CPT. On the other hand, the final population distributions after performing SSA with the SLAP, $\varphi_1^{\mathrm{SLAP}}(x)$ [given by Eq. (4.4)], and the CPT, $\varphi_1^{\mathrm{CPT}}(x)$, techniques is plotted in Fig. 4.4(b) with blue circles and red crosses, respectively. The initial population distribution in 1, $\varphi_{\mathrm{lat}}(x)$ [Eq. (4.3)], at the addressed site ($x_0 = 0$), and at the two next neighbors $x_{\pm1} = \pm532$ nm is shown as solid line. Note that, in the SLAP case (circles), the population of state 1 around x_0 remains almost the same after the addressing process, while in the first neighbor sites it is practically zero. On the other hand, for the CPT case (crosses), the population in the addressed site remains also nearly unchanged, but it exhibits a significant amount of population in the neighbor sites. This is in full agreement with the discussion following

Figs. 4.3(a) and 4.3(b). For this example, the total efficiencies found are $\eta^{\mathrm{CPT}} =$ 0 56 and $\eta^{\mathrm{SLAP}} = 0\ 95$ according to the corresponding values shown in Fig. 4.3(c). In addition, as it is shown in Fig. 4.4(a), the width of the pump node required to perform the SSA method is much larger than the addressed region $(\Delta x)_{\mathrm{SLAP}}$. In particular, for the case shown in Fig. 4.4, $w_P = \lambda_L$ and $(\Delta x)_{\mathrm{SLAP}} \quad \lambda_L$ 3, thus obtaining addressing resolution beyond the diffraction limit.

Finally, we carry out a comparison between our proposal and the experiment reported in Ref. [185], where a focused laser beam induces position dependent light shifts, allowing to perform a spin-flip by means of a resonant microwave pulse at the addressed site. Since the microwave field involved in the experiment has a Rabi frequency of kHz, the total spin-flip time is in the order of ms. In contrast, as our proposal makes use of only optical fields, the addressing time is three orders of magnitude below (μs). Specifically, to achieve similar values of the addressing resolution in both techniques, $(\Delta x) \sim 300$ nm, we have obtained an addressing time of ~ 40 μs. This decrease of the total addressing time needed implies a reduction of the effects caused by spontaneous scattering of photons, which are a limitation for the light shifts based proposals [184, 185]. These effects could be strongly reduced in our case. Also, we have compared the resolution obtained in both techniques. In Ref. [185], they use an addressing beam with an intensity FWHM of approximately 600 nm, and obtain a spin-flip probability distribution with FWHM=330 nm. In our technique, using $R = 1$ and a width of the pump node $w_P = 509$ nm, which corresponds to the width of their addressing beam, a very similar FWHM of the addressing probability distribution is obtained: $(\Delta x)_{\mathrm{SLAP}} = 330\ 66$ nm. Note that this value can be reduced by increasing the ratio between the pump and the Stokes intensities, *e.g.*, $R = 10$ implies $(\Delta x)_{\mathrm{SLAP}} =$ 181 86 nm and for $R = 100$ we obtain $(\Delta x)_{\mathrm{SLAP}} = 100\ 82$ nm.

4.5 Conclusions

In this Chapter, we have discussed a proposal to perform single-site addressing (SSA) in an optical lattice by using the SLAP technique. With respect to other dark state based techniques such as CPT, this method is fully coherent, robust against variations of the parameter values, and we have found that it yields higher efficiencies for smaller values of the intensity ratio between the pump and the Stokes fields. Moreover, the addressed atom does not interact with the fields, minimizing all possible decoherent processes. On the other hand, with respect to

the recent experiment on SSA using adiabatic spin-flips [185], the present proposal allows to use two degenerated ground levels, takes shorter times to perform the addressing process, and provides similar or even larger addressing resolutions for similar focusing of the addressing fields.

The proposed method provides an achievable addressing resolution that can be pushed well below the diffraction limit of the addressing light field and of the optical setup used for addressing or detection of atoms at closely spaced lattice sites. This relaxes the requirements on the optical setup or extends the achievable spatial resolution to lattice spacings smaller than accessible to date. Through analytical considerations, we have derived the range of parameters for which SSA is properly achieved. Moreover, we have obtained expressions to estimate the resolution and the efficiency of the SLAP based addressing method, and we have compared them with the analogous expressions obtained using the CPT technique. Next, by integrating the density matrix equations with realistic parameter values for state-of-the-art optical lattices loaded with ^{87}Rb atoms, we have checked the validity of the analytical approach.

5

Purity and spectral bandwidth of heralded single photons

The work presented in this chapter was done under the supervision of Dr. Alessandro Zavatta, from the Quantum Optics group at the Istituto Nazionale di Ottica (INO-CNR) in Florence (Italy), and in collaboration with Dr. Alejandra Valencia, from the Institut de Ciències Fotòniques (ICFO) in Barcelona (Spain). The goal of the collaboration was the development of a model capable of describing and giving reliable predictions about the experiment that the Quantum Optics group is carrying out. The experiment deal with the preparation of heralded pure single photons, created by means of spontaneous parametric down-conversion (SPDC), with the required spectral and spatial properties for using them in a homodyne detection setup, and eventually in photon addition and subtraction experiments [218].

In this Chapter, we present the procedure and calculations that we performed and the subsequent obtained results. First, in Section 5.1, a brief motivation is given, where we remark the need of having pure and heralded controlled-bandwidth single photons, and the different ways to produce them. Second, in Section 5.2, the theoretical model, consisting in a generalization of the spatial-to-spectral mapping technique [219 221], is exposed. After a general overview of the SPDC process, we derive the wavefunction that describes the generated two-photon state after SPDC, as well as explicit expressions for the joint spectrum of the photons, the spectrum of the signal photon conditioned by idler detection, and the purity of the signal photon. In Section 5.3, we obtain theoretical estimations using experimental parameter values for the quantities derived in Section 5.2: joint spectrum, signal spectrum, and signal photon purity. After comparing the spectrum results with the purity, we conclude that although the technique used to create controlled-bandwidth photon pairs without frequency correlations has a

good performance, it is not useful to obtain pure single photons. Then, we analyze different possible configurations in order to find optimal conditions for a high purity of the signal photons. Finally, in Section 5.4 we summarize the results and present the conclusions.

5.1 Introduction

The generation of indistinguishable photons with high purity has a great relevance in many quantum optics applications [222]. For instance, Hong-Ou-Mandel interference (HOMI) [223], or high fidelity quantum gates in linear optical quantum computing, requires purity and indistinguishability of single photons [224 226].

There are many different methods to generate single photons, which can be classified into two general categories. The first one consists of a single emitter, such as a single atom, ion, crystal vacancy or quantum dot, placed in a resonant optical cavity. In the strong coupling regime, these kind of single photon sources are almost deterministic. However, in many cases, the photon production rate at the output of the source is very low. Furthermore, cavity quantum electrodynamic systems are difficult to implement and require ultra-high vacuum chambers, and cryogenic temperatures in some cases. The second category of single photon sources consists of a large number of emitters, *e.g.*, an atomic gas or a bulk medium, pumped by a high repetition rate pulsed laser. These sources are probabilistic, which means that each pulse of the pump train has a limited probability to produce single photons. This drawback is partially overcome by the fact that some multiple-emitter sources create pairs of photons instead of single photons. Such feature gives the possibility to detect one of the photons, the trigger photon, to announce a pair-creation event, thus revealing the availability of the other photon of the pair.

One of the most widely used methods to obtain heralded single photons is the one based on spontaneous parametric down-conversion (SPDC) with conditional measurement of one photon of the generated pair. SPDC is a three-wave mixing process in which a photon of the pump is converted into a pair of daughter photons, called signal and idler, fulfilling energy and momentum conservation. Thus, the detection of the trigger photon, *e.g.*, the idler photon, heralds the presence of the signal in the corresponding emission channel [227]. However, in general, photon pairs are not created in a state with the desired properties for some of the required applications. In particular, the existing correlation between them

limits their applicability to many quantum information protocols. For this reason, several proposals have investigated how to manipulate the properties of the down-converted photons [221, 228 232].

In order to obtain pure single photon pairs one needs to have no correlations between any of the physical properties of the two photons, *i.e.*, polarization, transverse wavevector distribution, and spectrum. Polarization uncorrelated photons can be obtained using type-I parametric down-conversion, where the created photons have the same polarization. Using this configuration, the correlations in transverse momentum can be erased by detecting a single field mode obtaining by strong spatial filtering or using single-mode fibers. Regarding the correlations in frequency, a direct approach to obtain spectrally uncorrelated photons is to implement strong filtering in the path of the trigger photon. However, this approach severely reduces the number of detected coincidences of signal and idler photons. Different possibilities have been proposed to solve this problem. One of them is to directly generate narrow-band photons by using cavity enhanced SPDC [233, 234]. Another way to obtain pure single photons is to create them directly in a frequency uncorrelated state. For instance, in collinear type-II SPDC, different methods to obtain pure and heralded single photons have been reported, *e.g.*, by choosing appropriate pump spectral width and non-linear crystal length [228], or by using a crystal with equal group velocities for pump and idler photons [235]. However, since those approaches use type-II phase-matching the indistinguishability requirement in polarization is not satisfied. Approaches towards removing the frequency correlations of SPDC photons as well as preserving indistinguishability in polarization have been proposed by using the spatial-to-spectral mapping technique [219 221]. This technique allows to map the spatial features of the pump to the spectrum of the down-converted photons, thus can be used to engineer the frequency profile of the photons emerging from the SPDC setup. Recently, systematic analysis of the conditions to obtain heralded pure single photons have been carried out [236, 237].

In this Chapter, we study the generation of controlled bandwidth and frequency uncorrelated single photons to use them in a balanced homodyne detection setup. In turn, the final goal of this setup is to significantly increase the homodyne detection rate in photon addition and subtraction experiments [218]. Homodyne detection [238 240] is an interferometric technique that allows to measure the amplitude and phase of a weak light mode. This is performed by overlapping the signal in a 50% reflecting beam splitter with a strong coherent local oscilla-

tor (LO) field having the same frequency, and typically coming from the same source. After detecting the interference of the fields at the beam splitter outputs and substracting them, the quadratures of the signal can be obtained. To perform homodyne detection, a proper spatio-temporal overlap between the signal photon and the LO must exist. This means that the bandwidth of the photon entering the homodyne detection setup, *e.g.*, the signal photon, has to match the bandwidth of the LO. However, usually the photons emitted in a SPDC process have large bandwidths that make impossible to overlap them with the LO, unless spectral filtering is performed, thus reducing drastically the homodyne detection rate. In order to achieve this overlapping, our goal is to use the spatial-to-spectral mapping technique to engineer the spectrum profile of the emitted photons into a suitable desired bandwidth, hence avoiding the filtering process. It is important to note that the spatial-to-spectral mapping technique [220, 221] uses a scheme in which the signal and idler photons are equal spatially and spectrally filtered before being projected into single-mode fibers and analyze their joint spectrum. In what follows we will call this setup the symmetric filtering configuration. However, in homodyne detection the photon entering the setup shall not be spatially neither spectrally filtered in order to have an efficient detection, thus the symmetric configuration used in Ref. [220, 221] does not apply to our case, *i.e.*, we must consider an asymmetric configuration.

In order to describe all the possible experimental setups, in the next Section 5.2 we perform a generalization of the spatial-to-spectral mapping technique [220, 221] to an arbitrary filtering configuration and use it to analyze the spectrum of the down-converted photons in both the symmetric and asymmetric filtering situations. Moreover, to use the signal photon for quantum information and quantum computing applications it should be in a pure state, *i.e.*, uncorrelated from the idler. Therefore, we also give an explicit expression for the purity following the method in Ref. [236].

5.2 Spatial-to-spectral mapping generalization

5.2.1 Spontaneous parametric down-conversion (SPDC)

In general, the optical polarization, P, of a medium can be described as a power series in the electric field, E, of the incident wave:

$$P = \epsilon_0 \ \ \gamma^{(1)}E + \gamma^{(2)}E^2 + \gamma^{(3)}E^3 + \tag{5.1}$$

where ϵ_0 is the electric permittivity in vacuum, and $\gamma^{(1)}$, $\gamma^{(2)}$, and $\gamma^{(3)}$ are the first, second and third order terms of the electric susceptibility, respectively. While in linear optics, the first order susceptibility, or linear susceptibility, is sufficient to describe the interaction of light and matter, for non-linear processes the high order terms play an essential role. For instance, in SPDC process, the second order non-linear term is the responsible for the production of photon pairs.

In SPDC [241, 242], the polarized medium is an anisotropic and non-centrosymmetric non-linear crystal, characterized by its optical axis and frequency-dependent ordinary and extraordinary refractive indices $n_o(\ )$ and $n_e(\ )$, respectively. As already mentioned, during the interaction of the pump field with the crystal, a spontaneous process may occur, in which a photon of the pump is converted into the so-called signal and idler photons. This process takes place with a low probability, 10^{-8} to 10^{-10}, so one needs high power lasers to obtain a significant number of down-conversion events. In this three-wave mixing process, the down-converted photons have the required frequencies and wavevectors to conserve energy and momentum, also referred to as phase-matching conditions [242, 243]:

$$_p = \ _s + \ _i \tag{5.2a}$$

$$k_p = k_s + k_i \tag{5.2b}$$

where the subscripts p, s, and i denote pump, signal and idler, respectively. Due to the fact that the two photons are created at the same time, their spectral, spatial, and polarization properties are correlated, *i.e.*, they are entangled. Regarding the properties of the created photons, different types of down-conversion processes can be considered. First, depending on the relative directions of the signal and idler wavevectors, one can have collinear SPDC, when signal and idler propagate in the same direction, or non-collinear SPDC, if signal and idler propagate in different directions. Second, when signal and idler frequencies are equal, *i.e.*, $_s = \ _i = \ _p\ 2$, the process is degenerate. Third, considering the polarization, one can have type-I or type-II SPDC. In type-I, the polarization of the down-converted photons is equal, but different from the polarization of the pump. In this case, the generated photons emerge from the crystal in directions lying in the same polarization cone. In type-II SPDC, the polarizations of the signal and the idler are orthogonal, and each photon emerges in a different polarization cone due to the birefringence of the material.

5.2.2 The biphoton function

We consider a SPDC process as the one sketched in Fig. 5.1, which consists of a type-I non-linear (NL) crystal of length L, pumped by a strong pulsed laser of central frequency $\frac{c}{p}$, and longitudinal and transverse wave vectors k_p and q_p, respectively, propagating in the $+z_p$ direction. We consider a planar configuration, *i.e.*, the signal and idler wavevectors lie in the same $z-y$ plane. In Fig. 5.1, z_s and z_i are determined by the angles π_s and π_i, where the subscripts s and i correspond to signal and idler photons, respectively, and can be expressed in terms of the pump coordinates using the transformation

$$z_\mu = z_p \cos\pi_\mu - y_p \sin\pi_\mu \tag{5.3a}$$

$$y_\mu = z_p \sin\pi_\mu + y_p \cos\pi_\mu \tag{5.3b}$$

$$x_\mu = x_p \tag{5.3c}$$

where $\mu = s\ i$. Outside the crystal, the propagation angles for signal ($_s$) and idler ($_i$) photons are given by the Snell s law.

The two-photon state at the output of the NL crystal , after applying first order perturbation theory reads $= 0\ 0\ +\ _{\rm PDC}$, where

$$_{\rm PDC} = -\frac{i}{-}\int_0^\tau dt H_I(t)\ 0\ 0 \tag{5.4}$$

is the state of the parametric down-converted photons, $0\ 0 \equiv 0_s \otimes 0_i$ is the vacuum state, is the reduced Planck s constant, and $^{\rightarrow}$ is the interaction time. The effective second-order Hamiltonian $H_I(t)$ in the interaction picture has the form [244]:

$$H_I(t) = \epsilon_0 d_{\rm eff} \int_V dV E_p^{(+)}(r\ t) E_s^{(-)}(r\ t) E_i^{(-)}(r\ t) + H\ c \tag{5.5}$$

where V is the interaction volume and $d_{\rm eff}$ is an effective second-order nonlinear coupling coefficient, which depends on $\gamma^{(2)}$, the propagation direction of the pump beam and the crystal type, and determines the down-conversion efficiency [245]. The fields corresponding to the positive frequency component of the pump, and

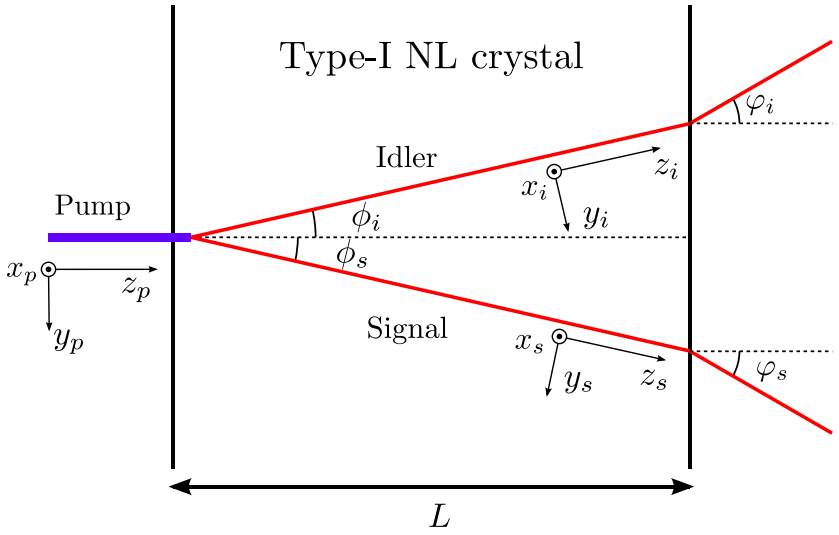

Figure 5.1: Scheme of the SPDC process. A pump pulse with central frequency ω_p^c and longitudinal and transverse wave vectors $\vec{k}_p$ and $\vec{q}_p$, respectively, propagating in the z_p direction enters a type-I non-linear (NL) crystal of length L. A pair of down-converted photons, signal and idler, identified by the subscript s and i, with central frequencies ω_s^c and ω_i^c, and longitudinal (transverse) momenta $\vec{k}_s$ and $\vec{k}_i$ ($\vec{q}_s$ and $\vec{q}_i$), respectively, are produced in directions z_s and z_i, determined by the angles ϕ_s and ϕ_i, respectively. Outside the crystal the angles, φ_s and φ_i, of the SPDC photons are given by the Snell's law.

the negative frequency components of signal and idler photons read

$$E_p^{(+)}(\vec{r},t) = A_p \int_{-\infty}^{+\infty} d\vec{q}_p d\omega_p \mathcal{E}_q(\vec{q}_p)\mathcal{E}_\omega(\omega_p)\exp[i\,(k_p z_p + \vec{q}_p\vec{x}_p - \omega_p t)], \tag{5.6a}$$

$$\hat{E}_s^{(-)}(\vec{r},t) = -iA_s \int_{-\infty}^{+\infty} d\vec{q}_s d\omega_s \exp[-i\,(k_s z_s + \vec{q}_s\vec{x_s} - \omega_s t)]\hat{a}^\dagger(\omega_s,\vec{q}_s), \tag{5.6b}$$

$$\hat{E}_i^{(-)}(\vec{r},t) = -iA_i \int_{-\infty}^{+\infty} d\vec{q}_i d\omega_i \exp[-i\,(k_i z_i + \vec{q}_i\vec{x}_i - \omega_i t)]\hat{a}^\dagger(\omega_i,\vec{q}_i), \tag{5.6c}$$

respectively, where $\vec{x}_\nu = (x_\nu, y_\nu)$, $\vec{q}_\nu = (q_{\nu x}, q_{\nu y})$, $\nu = \{p,s,i\}$, A_p is the pump amplitude, $A_\mu = \sqrt{\hbar\omega_\mu^c/2\epsilon_0 n(\omega_\mu^c)V_Q}$ with $n(\omega_\mu^c)$ being the index of refraction for the frequency ω_μ^c, and V_Q the quantization volume. The functions

$$\mathcal{E}_q(\vec{q}_p) = \exp\left[-|\vec{q}_p|^2\,\frac{\mathrm{w}_0^2}{2}\right], \tag{5.7a}$$

$$\mathcal{E}_\omega(\omega_p) = \exp\left[-\frac{\Omega_p^2}{2B_p^2}\right] = \exp\left[-\frac{(\Omega_s+\Omega_i)^2}{2B_p^2}\right] \tag{5.7b}$$

are, respectively, the spatial, in transverse momentum space, and spectral envelopes of the pump pulse, where w_0 is the beam waist, B_p the spectral width, and $\Omega_\nu = \ _\nu - \ ^0_\nu$ is the detuning from the central frequency. Note that in Eq. (5.5), while the pump field is classical, the signal and idler fields are expressed in the second quantization form, being $a\ (\ _\mu\ q_\mu)$ the creation operator for the generated photons.

Inserting Eqs. (5.6a)-(5.6c) in Eq. (5.5), and using Eqs. (5.3a)-(5.3c), the interaction Hamiltonian reads:

$$H_I(t) = -K \int dV \iiint_-^+ dq_p dq_s dq_i \iiint_-^+ d\ _p d\ _s d\ _i \mathcal{E}_q(q_p) \mathcal{E}\ (\ _p) a\ (\ _s\ q_s) \times a\ (\ _i\ q_i) e^{-i\Delta_k z_p} e^{-i(\Delta_0 - q_{py}) y_p} e^{-i(q_{sx}+q_{ix}-q_{px}) x_p} e^{-i[\ _p - (\ _s + \ _i)t]} \tag{5.8}$$

where $K = \epsilon_0 d_{\text{eff}} A_p A_s A_i$ and,

$$\Delta_k = k_{iz}\cos\pi_i + k_{sz}\cos\pi_s - k_{pz} + q_{sy}\sin\pi_s + q_{iy}\sin\pi_i \tag{5.9a}$$

$$\Delta_0 = -k_{iz}\sin\pi_i - k_{sz}\sin\pi_s + q_{sy}\cos\pi_s + q_{iy}\cos\pi_i \tag{5.9b}$$

Expanding the wave vectors in Taylor series up to first order, $k_\nu \quad k^0_\nu + n_\nu \Omega_\nu$, where $n_\nu = \frac{dk_\nu}{d\ _\nu}$ is the refractive index, and considering the particular case $\pi_i = -\pi_s = \pi$, we get

$$\Delta_k \quad -(n_p - n_s\cos\pi)\,\Omega_+ + (q_{sy} - q_{iy})\sin\pi \tag{5.10a}$$

$$\Delta_0 \quad -n_s\Omega_-\sin\pi + (q_{sy} + q_{iy})\cos\pi \tag{5.10b}$$

where we have used $k^0_{pz} = k^0_{sz}\cos\pi + k^0_{iz}\cos\pi$, $\left(-k^0_{iz} + k^0_{sz}\right)\sin\pi = 0$, $n_s = n_i$, and $\Omega_\pm = \Omega_s \pm \Omega_i$. Therefore, the interaction Hamiltonian (5.8) can be rewritten as:

$$\begin{aligned} H_I(t) = -K \iiint_-^+ dq_p dq_s dq_i \iiint_-^+ d\ _p d\ _s d\ _i \mathcal{E}_q(q_p) \mathcal{E}\ (\ _p) \times \\ a\ (\ _s\ q_s) a\ (\ _i\ q_i) e^{-i[\ _p - (\ _s + \ _i)]t} \times \\ \int_0^L e^{-i\Delta_k z_p} dz_p \int_-^+ e^{-i(q_{sx}+q_{ix}-q_{px})x_p} dx_p \int_-^+ e^{-i(\Delta_0 - q_{py})y_p} dy_p \end{aligned} \tag{5.11}$$

Inserting the expression for the interaction Hamiltonian (5.11) in (5.4), the state

function of the SPDC photons can be written as

$$\begin{aligned} \text{PDC} \;=& \frac{i}{-}K \iiint_{-}^{+} dq_p dq_s dq_i \iiint_{-}^{+} d\;\; {}_p d\;\; {}_s d\;\; {}_i \mathcal{E}_q(q_p)\mathcal{E}\;\; (\;\; {}_p)\delta(\;\; {}_p - \;\; {}_s - \;\; {}_i) \times \\ & L\,\mathrm{sinc}\left(\frac{\Delta_k L}{2}\right) e^{-i\Delta_k L\;\; 2}\delta\left(q_{sx} + q_{ix} - q_{px}\right)\delta\left(\Delta_0 - q_{py}\right)\;\; 1\;\; 1 \end{aligned} \tag{5.12}$$

where we have used $\int_0^\tau \exp\left[-i\left(\;\; {}_p - \left(\;\; {}_s + \;\; {}_i\right) t\right)\right] dt \quad \delta\left(\;\; {}_p - \;\; {}_s - \;\; {}_i\right)$. The delta functions $\delta\left(\Delta_0 - q_{py}\right)$ and $\delta\left(q_{sx} + q_{ix} - q_{px}\right)$ come from the fact that we have considered the pump beam waist much smaller than the transverse dimensions of the crystal. It is important to mention that we have validated this assumption by numerically calculating the integrals in the last line of Eq. (5.11) using the parameter values given in Section 5.3. Finally, the wavefunction of the paired photons just after the SPDC process can be expressed as

$$\text{PDC} \;= \eta \iint_{-}^{+} dq_s dq_i \iint_{-}^{+} d\Omega_s d\Omega_i \Phi\left(\Omega_s\;\; \Omega_i\;\; q_s\;\; q_i\right)\;\; 1\;\; 1 \tag{5.13}$$

where $\eta = iKL \quad$ gives the down-conversion efficiency, and the mode function $\Phi\left(\Omega_s\;\; \Omega_i\;\; q_s\;\; q_i\right)$ or biphoton is defined as:

$$\Phi\left(\Omega_s\;\; \Omega_i\;\; q_s\;\; q_i\right) = \mathcal{E}_q(q_{sx} + q_{ix}\;\; \Delta_0)\mathcal{E}\;\; (\Omega_s + \Omega_i) e^{-(\alpha\Delta_k L\;\; 2)^2} e^{-i\Delta_k L\;\; 2} \tag{5.14}$$

where we have approximated the phase-matching function $\mathrm{sinc}\left(\frac{\Delta_k L}{2}\right)$ by an exponential function with the same width at the $1\;\; e^2$ of the intensity, *i.e.*, $\mathrm{sinc}\left(\Delta_k L\;\; 2\right)$ $\exp\;\; -\alpha^2\left(\Delta_k L\;\; 2\right)^2$ with $\alpha = 0\,455$ [221]. This approximation has also been validated through numerical integration. Note that in the biphoton function, Eq. (5.14), the dependence on the frequency and momentum variables appears through the phase-matching condition Δ_k, but also through the pump envelopes $\mathcal{E}$ and $\mathcal{E}_q$. The latter dependence is the basis of the spatial-to-spectral mapping technique, since by controlling the pump parameters, for instance the pump waist w_0, we can modify the spatial and spectral properties of the SPDC photons.

A. Joint Spectrum

In order to perform homodyne detection efficiently, we need an input state with the same bandwidth than the local oscillator (LO). Usually, the photons emerging from a SPDC setup exhibit large bandwidths. Therefore, to avoid filtering it is convenient to directly prepare the photons in a frequency state by shaping the

distribution of their joint spectrum in such a way that it exhibits a desired bandwidth. Moreover, for quantum information and quantum computing purposes, photons with a high purity, *i.e.*, with a low correlation degree with its partner, are desirable. Regarding frequency correlations, this means that the joint spectrum of the SPDC photons should be a separable product of two functions, each one depending either on Ω_s or Ω_i. Both requirements, controlled bandwidth and no frequency correlations, can be satisfied by using the spatial-to-spectral mapping technique [220, 221] described above, which allows to transfer the spatial properties of the pump beam to the spectral features of the emitted photons [see Eq. (5.14)]. Here we consider this technique without restricting ourselves to the symmetric filtering case.

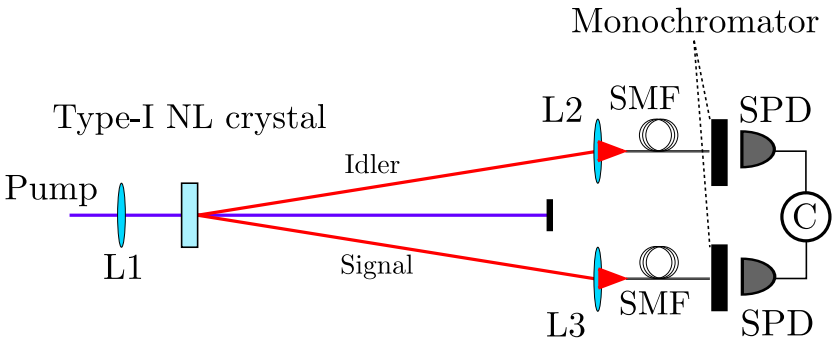

Figure 5.2: Setup of the detection process to analyze the joint spectrum of the photons. The lens L1 focuses the pump beam into the BBO crystal, and the down-converted photons are collected by lenses L2 and L3, which project them into single-mode fibers (SMF). After the fibers, a couple of monochromators scan the frequency of the collected photons, which are detected by proportional photodiodes (PPD) connected to a coincidence detector device (C).

In the experiments to measure the joint spectrum of the signal and idler pairs, the photons are collected by convergent lenses that focus them into single-mode fibers, as it is depicted in Figure 5.2. The detection is performed by means of two proportional photodiodes, which are connected to a coincidence counter, and a pair of monochromators are used to scan the frequencies of the idler and signal photons. The spatial filters consist in the combination of a lens and a single-mode fiber[1], which are modeled in the calculations by Gaussian shaped filters of the

[1]Indeed, the filtering can be performed only with a single-mode fiber, but then the number of collected photons is very low.

form

$$U_j\left(q_j\right) = N_{sj} \exp \quad - \; q_j \;^2 \frac{\mathrm{w}_{sj}^2}{2} \tag{5.15}$$

where w_{sj} is the width of the spatial filtering profile, N_{sj} an attenuation factor due to a possible light absorption by the optical elements, and $j = \;\; s \;\; i \;\;$ denotes signal or idler channels. These filters act on the two-photon wavefunction as a projector $\quad _{\mathrm{PDC}} \; = p_F \quad _{\mathrm{PDC}}$, being

$$p_F = \iint_{-}^{+} \; dq_i dq_s \iint_{-}^{+} \; d\Omega_i d\Omega_s F_i\left(\Omega_i\right) U_i\left(q_i\right) F_s\left(\Omega_s\right) U_s\left(q_s\right) \;\; 1 \;\; 1 \quad 1 \;\; 1 \tag{5.16}$$

and, in order to keep generality, we have included Gaussian functions to describe a possible frequency filter of the form

$$F_j\left(\Omega_j\right) = N_{fj} \exp \quad - \frac{\Omega_j^2}{2B_{fj}^2} \tag{5.17}$$

with B_{fj} the width of the frequency filter profile and N_{fj} an attenuation factor due to a possible non-desired absorption. Therefore, the joint spectrum, or probability distribution to detect signal and idler photons at given frequencies, *i.e.*, $S_J(\Omega_s \;\; \Omega_i) = \left| \;\; 1_{\Omega_s} \;\; 1_{\Omega_i} \;\; \iint dq_s dq_i \left\langle 1_{q_s} \;\; 1_{q_i} \right| \quad _{\mathrm{PDC}} \; \right|^2$, where we have used the notation $1_j \;\; = \left|1_{\Omega_j}\right\rangle \otimes \left|1_{q_j}\right\rangle$, reads

$$S_J(\Omega_s \;\; \Omega_i) = \left| \iint_{-}^{+} \; dq_s dq_i \Phi\left(\Omega_s \;\; \Omega_i \;\; q_s \;\; q_i\right) U_s\left(q_s\right) U_i\left(q_i\right) F_s\left(\Omega_s\right) F_i\left(\Omega_i\right) \right|^2 \tag{5.18}$$

Carrying out the integrals of Eq. (5.18), the peak normalized spectrum $S_J(\Omega_s \;\; \Omega_i) \equiv S_J(\Omega_s \;\; \Omega_i) \;\; S_J(0 \;\; 0)$ of the down-converted photons takes the form:

$$S_J(\Omega_s \;\; \Omega_i) = \exp\left[-\frac{\Omega_+^2}{2\phi_+^2}\right] \exp\left[-\frac{\Omega_-^2}{2\phi_-^2}\right] \exp\left[\frac{\Omega_+\Omega_-}{\phi_c^2}\right] \tag{5.19}$$

where

$$\frac{1}{\phi_+^2} = \frac{-\kappa^2\ 2}{A_+ + \mathrm{w}_{si}^2} - \delta\kappa^2\left(1 + \frac{A_-}{A_+ + \mathrm{w}_{si}^2}\right)^2 + (\alpha L)^2\left(n_p - n_s\cos\pi\right)^2 + \frac{2}{B_p^2} + \frac{1}{2B_{fs}^2} + \frac{1}{2B_{fi}^2} \tag{5.20a}$$

$$\frac{1}{\phi_-^2} = \frac{-\beta^2\ 2}{A_+ + \mathrm{w}_{si}^2} - \delta\beta^2\left(1 - \frac{A_-}{A_+ + \mathrm{w}_{si}^2}\right)^2 + 2n_s^2\mathrm{w}_0^2\sin^2\pi + \frac{1}{2B_{fs}^2} + \frac{1}{2B_{fi}^2} \tag{5.20b}$$

$$\frac{1}{\phi_c^2} = \frac{-\beta\kappa\ 2}{A_+ + \mathrm{w}_{si}^2} + \delta\beta\kappa\left(1 - \frac{A_+}{A_+ + \mathrm{w}_{si}^2}\right)\left(1 + \frac{A_-}{A_+ + \mathrm{w}_{si}^2}\right) + \frac{1}{2B_{fs}^2} - \frac{1}{2B_{fi}^2} \tag{5.20c}$$

and

$$A_\pm = \mathrm{w}_0^2\cos^2\pi \pm \frac{(\alpha L)^2}{2}\sin^2\pi \tag{5.21a}$$

$$\beta = 2\mathrm{w}_0^2 n_s\cos\pi\sin\pi \tag{5.21b}$$

$$\kappa = (\alpha L)^2\left(n_p - n_s\cos\pi\right)\sin\pi \tag{5.21c}$$

$$\delta = \frac{\left(A_+ + \mathrm{w}_{si}^2\right)}{2\left[\left(A_+ + \mathrm{w}_{ss}^2\right)\left(A_+ + \mathrm{w}_{si}^2\right) - A_-^2\right]} \tag{5.21d}$$

In Eq. (5.19), the variables $\Omega_\pm$ and the respective widths $\phi_\pm$ determine the kind of correlations between the emitted photons. In particular, when $\phi_+ - \phi_- \ll \phi_c$, there is contribution to the spectrum only from $\Omega_+ = \Omega_s + \Omega_i$, so the photons are correlated in frequency, *i.e.*, the joint spectrum is distributed along the line $\Omega_s = \Omega_i$, while for $\phi_- - \phi_+ \ll \phi_c$ the contribution of $\Omega_- = \Omega_s - \Omega_i$ dominates and they are anticorrelated, *i.e.*, the joint spectrum follows the line $\Omega_s = -\Omega_i$. For the case when both widths are equal, $\phi_+ = \phi_- \equiv \phi$, the spectrum function expressed in terms of Ω_s and Ω_i variables is separable, *i.e.*, it can be written as a product of two contributions:

$$S_J(\Omega_s\ \Omega_i) = \exp\left[-\frac{\Omega_s^2}{2\phi_s^2}\right]\exp\left[-\frac{\Omega_i^2}{2\phi_i^2}\right] \tag{5.22}$$

where $\phi_s = \sqrt{\phi^2\phi_c^2\ 2\left(\phi_c^2 - \phi^2\right)}$ and $\phi_i = \sqrt{\phi^2\phi_c^2\ 2\left(\phi_c^2 + \phi^2\right)}$, which means that the photons are frequency uncorrelated. Note that by imposing equal spatial and spectral filters, *i.e.*, $\mathrm{w}_{ss} = \mathrm{w}_{si}$ and $B_{fs} = B_{fi}$, respectively, we obtain $1 \ll \phi_c =$

0, and therefore one recovers the results of Refs. [220, 221], in which the joint spectrum is a symmetric Gaussian distribution. However, the situation with equal filters is not suitable for our case because, while the signal photon should enter the homodyne detection setup without being spatial nor spectral filtered, the idler photon is spatially filtered by the lens and the single-mode fiber. From Eqs. (5.20) and (5.21) the optimal parameter values for the production of uncorrelated photon pairs, *i.e.*, those for which $\phi_+ = \phi_-$, can be obtained. In particular the optimal pump spatial width, w_0, is given by

$$\begin{aligned}\mathrm{w}_0^2 = & \left[\frac{1}{B_p^2} + \frac{(\alpha L)^2}{2}\left(n_p - n_s\cos\pi\right)^2\right] + \frac{\mathrm{w}_{si}^2 + \mathrm{w}_{ss}^2}{\mathrm{w}_{si}^2\mathrm{w}_{ss}^2} \quad \frac{\alpha L \sin\pi}{\overline{2}B_p} \quad ^2 \times \\ & \left[\frac{\mathrm{w}_{si}^2 + \mathrm{w}_{ss}^2}{\mathrm{w}_{si}^2\mathrm{w}_{ss}^2}\left\{\frac{(\alpha L)^2}{2} \quad n_s^2\sin^4\pi - \left(n_p - n_s\cos\pi\right)^2\cos^2\pi \quad - \frac{\cos^2\pi}{B_p^2}\right] + \right. \\ & \left. n_s^2\sin^2\pi - \frac{(\alpha L)^2\sin^2(2\pi)}{2B_p^2\mathrm{w}_{si}^2\mathrm{w}_{ss}^2} \right. \quad ^{-1} \end{aligned} \tag{5.23}$$

In the case of not spatially projecting the signal photon, $\mathrm{w}_{ss} = 0$, the optimal parameter value has a simpler form:

$$\mathrm{w}_0 = \frac{\frac{(\alpha L)^2}{2}\frac{\sin^2\omega}{B_p^2}}{\frac{(\alpha L)^2}{2} \quad N_s^2\sin^4\pi - \left(N_p - N_s\cos\pi\right)^2\cos^2\pi - \frac{\sin^2(2\omega)}{B_p^2\mathrm{w}_{si}^2} \quad - \frac{\cos^2\omega}{B_p^2}} \tag{5.24}$$

Note that, in order to found real values for this expression, additional conditions are needed for the angle π and the refractive indices n_p and n_s. These conditions will be discussed in more detail in the next Section 5.3. On the contrary, when one considers equal spatial filters, real values of Eq. (5.23) can be found in general by tuning w_{ss} (which is equal to w_{si}) at will.

B. Spectrum of conditioned signal

After finding the optimal parameter conditions for the production of uncorrelated photon pairs, the next step is to use the signal photon for homodyne detection. In this scheme, the idler photon is used to herald the presence of the signal. This allows to minimize the time for which the homodyne detection setup is coupled with the vacuum state, by opening the detection setup only when the signal photon is arriving. The difference with respect to the previous setup (Fig. 5.2) is that

the heralding is performed by removing the monochromator of the idler path (see Fig. 5.3), so we do not perform frequency measurement in the idler channel. In addition, the signal photon is directly sent to the homodyne detection setup, thus it is not spatially nor spectrally filtered. However, for generality, we keep the functions $U_s(q_s)$ and $F_s(\Omega_s)$ in the calculations, whose width can be arbitrarily enlarged in order to fit our non-filtering requirements. Finally, for homodyne detection we need a signal photon with a controlled bandwidth that matches as much as possible the one of the LO. Therefore, our aim is to analyze the spectrum of the signal photon detected in coincidence with the idler.

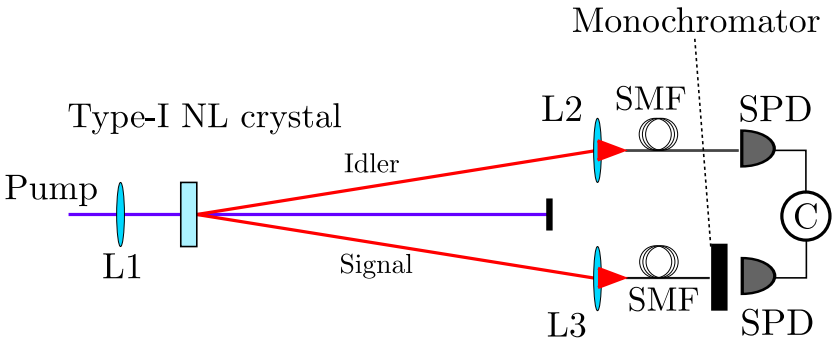

Figure 5.3: Setup of the detection process to analyze the spectrum of the signal photons conditioned to detection of an idler. The difference with respect to the setup shown in Fig. 5.2 is that here there is no monochromator in the idler channel to measure the idler frequency.

Mathematically, the difference of this configuration with respect to Eq. (5.18) is that, since we are not projecting the frequency state of the idler photon, we must keep the integral over all the possible frequencies Ω_i. Therefore, the signal photon spectrum, in coincidence with the idler, is

$$S_C(\Omega_s) = \left| \int_-^+ d\Omega_i \iint_-^+ dq_s dq_i \Phi(\Omega_s\ \ \Omega_i\ \ q_s\ \ q_i)\, U_s(q_s)\, U_i(q_i)\, F_s(\Omega_s)\, F_i(\Omega_i) \right|^2 \tag{5.25}$$

After carrying out the integrals and normalizing to the peak value, $S_C(0)$, Eq. (5.25) reads

$$S_C(\Omega_s) = \exp\ \frac{2\left(\phi_-^2\phi_+^2 - \phi_c^4\right)\Omega_s^2}{\phi_c^4\left(\phi_+^2 + \phi_-^2\right) + 2\phi_-^2\phi_+^2\phi_c^2} \tag{5.26}$$

Note that in the case where $\phi_+ = \phi_- \equiv \phi$, the width of the signal photon spectrum coincides with the one of the joint spectrum, ϕ_s in Eq. (5.22), for $\Omega_i = 0$. This result is the one that we expect since for $\phi_+ = \phi_-$ the frequency spectra of signal

and idler photons are independent. Eq. (5.26) shows that we can use the spatial-to-spectral technique to engineer the signal photon with a proper spectrum profile that matches the local oscillator (LO) of the homodyne detection. In addition, by satisfying $\phi_+ = \phi_-$, we can achieve frequency uncorrelated photon pairs without the need of strong spatial or spectral filtering, *i.e.*, using $B_{fs} = B_{fi}$ and $\mathrm{w}_{ss} = \mathrm{w}_{si} = 0$. In order to quantify the degree of correlation between the two photons, in what follows we introduce the purity of the signal photon.

C. Purity of the signal photon

The possibility to create signal photons with high purity is important because it allows to implement quantum gates and operations with high fidelity, and also increases the homodyne detection efficiency. In particular, the overall efficiency that we have after the measurement is $\eta_T = \eta_d P_s$, where η_d is the detection efficiency and P_s is the purity of the signal photon, which is defined as

$$P_s = \frac{\mathrm{Tr}\left(\varphi_s^2\right)}{\left[\mathrm{Tr}\left(\varphi_s\right)\right]^2} \tag{5.27}$$

where φ_s is the density matrix of the signal photon and $\mathrm{Tr}\left(\varphi\right)$ is the trace of φ. In the case of $P_s = 1$ the signal photon is pure, *i.e.*, the two photons of the pair are uncorrelated, while if $P_s < 1$ the two-photon state is a mixture state, with $P_s = 0$ corresponding to a maximally entangled state. The state of the signal photon φ_s is given by

$$\varphi_s = \mathrm{Tr}_{\,i}\left(\varphi_{si}\right) \tag{5.28}$$

where $\mathrm{Tr}_{\,i}$ is the partial trace over the idler variables and, $\varphi_{si} =$ PDC PDC is the density matrix of the biphoton state after passing all the optical elements of the experimental setup, just before the single-photon detection. Using Eqs. (5.13), (5.16), and (5.28), the density matrix of the signal photon reads

$$\begin{aligned}\varphi_s = \iiint_{-}^{+} dq_s dq_i dq_s \iiint_{-}^{+} d\Omega_s d\Omega_i d\Omega_s F_i^2\left(\Omega_i\right) U_i^2\left(q_i\right) F_s\left(\Omega_s\right) F_s\left(\Omega_s\right) \times \\ \times U_s\left(q_s\right) U_s\left(q_s\right) \Phi\left(\Omega_s\ \ \Omega_i\ \ q_s\ \ q_i\right) \Phi^*\left(\Omega_s\ \ \Omega_i\ \ q_s\ \ q_i\right)\ 1_s\ \left\langle 1_s\right|\end{aligned} \tag{5.29}$$

and therefore,

$$\begin{aligned}\mathrm{Tr}\left(\varphi_s^2\right) = \iint_-^+ dq_s dq_i \iint_-^+ dq_s\, dq_i \iint_-^+ d\Omega_s d\Omega_i \iint_-^+ d\Omega_s d\Omega_i \times \\ \left[F_i\left(\Omega_i\right) U_i\left(q_i\right) F_s\left(\Omega_s\right) U_s\left(q_s\right) F_i\left(\Omega_i\right) U_i\left(q_i\right) F_s\left(\Omega_s\right) U_s\left(q_s\right)\right]^2 \times \\ \Phi\left(\Omega_s\ \Omega_i\ q_s\ q_i\right) \Phi^*\left(\Omega_s\ \Omega_i\ q_s\ q_i\right) \Phi\left(\Omega_s\ \Omega_i\ q_s\ q_i\right) \Phi^*\left(\Omega_s\ \Omega_i\ q_s\ q_i\right)\end{aligned} \tag{5.30}$$

and

$$\begin{aligned}\mathrm{Tr}(\varphi_s) \;=\; \iint_-^+ dq_s dq_i \iint_-^+ d\Omega_s d\Omega_i \left[F_i\left(\Omega_i\right) U_i\left(q_i\right) F_s\left(\Omega_s\right) U_s\left(q_s\right)\right]^2 \times \\ \Phi\left(\Omega_s\ \Omega_i\ q_s\ q_i\right)^2\end{aligned} \tag{5.31}$$

To perform those integrals we use the following mathematical equivalence [236]:

$$\int_-^+ \exp\left[-\frac{v^t M v}{2} + i v^t u\right] dv = \frac{(2\nu)^{n\ 2}}{\overline{\mathrm{Det}(M)}} \exp\left[-\frac{u^t M^{-1} u}{2}\right] \tag{5.32}$$

where M is a symmetric and positive definite $n \times n$ matrix, and v and u are vectors of order n. Since the product of the biphoton function, Eq. (5.14), with the filter functions, Eqs. (5.15) and (5.17), can be written as an exponential function with the exponent being a second order polynomial of the variables q_{sx}, q_{sy}, q_{ix}, q_{iy}, Ω_s and Ω_i we can use Eq. (5.32) to carry out the integrals of Eqs. (5.30) and (5.31). For Eq. (5.30), $v = (q_{sx}\ q_{sy}\ q_{sx}\ q_{sy}\ q_{ix}\ q_{iy}\ q_{ix}\ q_{iy}\ \Omega_s\ \Omega_i\ \Omega_s\ \Omega_i)^t$, $u = 0$, and the matrix M reads

$$M = \begin{pmatrix}
a_s & 0 & 0 & 0 & f & 0 & f & 0 & 0 & 0 & 0 & 0 \\
0 & b_s & 0 & 0 & 0 & g & 0 & g & h & 0 & l & l \\
0 & 0 & a_s & 0 & f & 0 & f & 0 & 0 & 0 & 0 & 0 \\
0 & 0 & 0 & b_s & 0 & g & 0 & g & 0 & h & l & l \\
f & 0 & f & 0 & a_i & 0 & 0 & 0 & 0 & 0 & 0 & 0 \\
0 & g & 0 & g & 0 & b_i & 0 & 0 & -l & -l & -h & 0 \\
f & 0 & f & 0 & 0 & 0 & a_i & 0 & 0 & 0 & 0 & 0 \\
0 & g & 0 & g & 0 & 0 & 0 & b_i & -l & -l & 0 & -h \\
0 & h & 0 & 0 & 0 & -l & 0 & -l & d_s & 0 & m & m \\
0 & 0 & 0 & h & 0 & -l & 0 & -l & 0 & d_s & m & m \\
0 & l & 0 & l & 0 & -h & 0 & 0 & m & m & d_i & 0 \\
0 & l & 0 & l & 0 & 0 & 0 & -h & m & m & 0 & d_i
\end{pmatrix} \tag{5.33}$$

where

$$a_j = 2\left(\mathrm{w}_0^2 + \mathrm{w}_{sj}^2\right) \tag{5.34a}$$

$$b_j = 2\mathrm{w}_{sj}^2 + 2\mathrm{w}_0^2\cos^2\pi + L^2\alpha^2\sin^2\pi \tag{5.34b}$$

$$d_j = \frac{2}{B_{fj}^2} + \frac{2}{B_p^2} + L^2\alpha^2\left(n_p - n_s\cos\pi\right)^2 + 2\mathrm{w}_0^2 n_s^2\sin^2\pi \tag{5.34c}$$

$$f = \mathrm{w}_0^2 \tag{5.34d}$$

$$g = \mathrm{w}_0^2\cos^2\pi - \frac{1}{2}L^2\alpha^2\sin^2\pi \tag{5.34e}$$

$$h = -\left[L^2\alpha^2\left(n_p - n_s\cos\pi\right) + 2\mathrm{w}_0^2 n_s\cos\pi\right]\sin\pi \tag{5.34f}$$

$$l = -\frac{1}{2}\left[L^2\alpha^2\left(n_p - n_s\cos\pi\right) - 2\mathrm{w}_0^2\cos\pi\right]\sin\pi \tag{5.34g}$$

$$m = \frac{1}{B_p^2} + \frac{1}{2}L^2\alpha^2\left(n_p - n_s\cos\pi\right)^2 - \mathrm{w}_0^2 n_s^2\sin^2\pi \tag{5.34h}$$

being $j = \ s\ i\ $, while for Eq. (5.31), $v = (q_{sx}\ q_{sy}\ q_{ix}\ q_{iy}\ \Omega_s\ \Omega_i)^t$, $u = 0$, and the matrix M is

$$M = \begin{pmatrix} a_s & 0 & 2f & 0 & 0 & 0 \\ 0 & b_s & 0 & 2g & h & 2l \\ 2f & 0 & a_i & 0 & 0 & 0 \\ 0 & 2g & 0 & b_i & -2l & -h \\ 0 & h & 0 & -2l & d_s & 2m \\ 0 & 2l & 0 & -h & 2m & d_i \end{pmatrix} \tag{5.35}$$

Therefore, by using the identity in Eq. (5.32) to calculate Eqs. (5.30) and (5.31), one can estimate the purity of the photons that arrive at the homodyne detection setup, Eq. (5.27). In the next Section 5.3 we use experimental values for the parameters to give specific predictions about the spectrum and purity of the photons produced in the SPDC process.

5.3 Experimental setup and theoretical predictions

A schematic description of the experimental setup implemented in the group of Dr. Zavatta, in the Quantum Optics laboratory, is shown in Fig. 5.4. In the experiment, the light used to produce photon pairs is generated from a Ti:Sapphire laser which emits femtosecond light pulses with central wavelength of approximately 800 nm. Part of the light intensity is redirected with a beam splitter to the homodyne

detection setup, to be used as the local oscillator (LO). The homodyne detection setup consists in a 50% reflecting beam splitter, a couple of proportional photodiodes, and a device that performs substraction of the two beam splitter outputs. The light that is not used as LO, after being frequency doubled in a second harmonic generator, *i.e.*, the outcoming light has central wavelength $\lambda_p^c = 400$ nm, is focused into a β-barium-borate (BBO) crystal prepared for type-I parametric down-conversion, of thickness $L = 0\ 3$ mm and transverse section 5×5 mm^2. For this kind of crystal the ordinary and extraordinary refractive indices, given by the Sellmeier equations, are [246]

$$n_o(\lambda) = \sqrt{2\ 7359 + \frac{0\ 01878}{\lambda^2 - 0\ 01822} - 0\ 01354\lambda^2} \tag{5.36a}$$

$$n_e(\lambda) = \sqrt{2\ 3753 + \frac{0\ 01224}{\lambda^2 - 0\ 01667} - 0\ 01516\lambda^2} \tag{5.36b}$$

which correspond to a ray propagating perpendicularly to the optical axis, and determine the possible phase-matching angles θ and the refractive indices of the pump (n_p), signal (n_s), and idler (n_i) photons. Since we consider degenerated non-collinear type-I SPDC the signal and idler photons are emitted in the same polarization cone and propagate as ordinary rays, *i.e.*, their refractive indices $n_s = n_i = dk_s\ d\ _s$, with $k_s = k_i = 2\nu n_o(\lambda_s)\ \lambda_s$, do not depend on the propagation angle with respect to the optical axis. On the other hand, the pump propagates as an extraordinary ray, $n_p(\theta) = dk_p(\theta)\ d\ _p$, where $k_p(\theta) = 2\nu n_e\left(\lambda_p\ \theta\right)\ \lambda_p$ and

$$n_e\left(\lambda\ \theta\right) = \left(\frac{\cos^2\theta}{n_o\left(\lambda\right)^2} + \frac{\sin^2\theta}{n_e\left(\lambda\right)^2}\right)^{-1\ 2} \tag{5.37}$$

The phase-matching angle θ can be found by solving

$${}_p^c n_e\left(\lambda_p^c\ \theta\right) = {}_i^c n_o\left(\lambda_i^c\right)\cos\pi_i + {}_s^c n_o\left(\lambda_s^c\right)\cos\pi_s \tag{5.38}$$

which comes from the phase-matching condition [Eq. (5.2b)].

The bandwidth of the pump pulses is taken as $B_p = 21\ 26$ THz [see Eq. (5.7b)], and the pump spatial width w_0 inside the crystal [Eq. (5.7a)] can be varied between $w_0^{(\min)} \sim 10\ \mu$m (due to the diffraction limit) and $w_0^{(\max)}\ \ 1800\ \mu$m (due to the transverse size of the crystal). One of the down-converted photons, the signal, is sent to the homodyne detection setup, while the other, the idler, can be spatially and/or spectrally filtered, and is used as a trigger to herald the presence of the

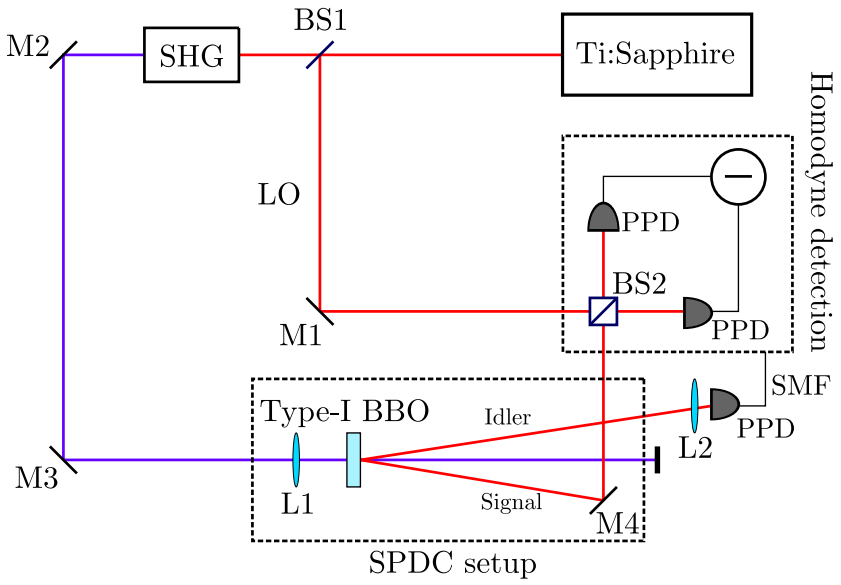

Figure 5.4: Experimental setup used for homodyne detection of spectrum engineered heralded single photons. The light source is a Ti:Sapphire laser, M1, M2, M3 and M4 are perfectly reflecting mirrors, BS1 and BS2 are beam splitters (the latter a 50% splitter), SHG is the second harmonic generator, L1 and L2 are convergent lenses, SMF is a single-mode fiber, and PPD are proportional photodiodes.

signal, in such a way that the time that the homodyne detection is coupled with the vacuum state can be minimized.

At a preliminary stage of the experiment, in order to prepare the system for the emission of frequency uncorrelated photon pairs, the joint spectrum is measured. Therefore, the homodyne detection setup is not present, and a setup as the one described in Fig. 5.2 is used: both the signal and the idler photons generated inside the crystal are projected into transverse Gaussian modes of width $w_{ss} = w_{si} = 1480\ \mu$m [see Eq. (5.15)] and sent, through single-mode fibers, to a pair of monochromators that independently scan the frequency of each photon. In order to obtain an optimal detection efficiency no frequency filtering is implemented in any of the channels, *i.e.*, $B_{fs} = B_{fi}$, apart from the projection operation done by the momochromators. Finally, proportional photodiodes are connected to a coincidence detection device used to obtain the data. For this symmetric configuration, the generated photons are collected at angles $_i = - _s = 1\ 5^\circ$ [see Fig. 5.1], which imply refractive indices of $n_p = 5\ 81 \times 10^{-3}$, $n_s = 5\ 61 \times 10^{-3}$, and an angle inside the crystal $\pi_i = -\pi_s = 0\ 90^\circ$, which is obtained using the Snell s law $n_o(\lambda_s^c) \sin \pi_i = \sin \ _i$.

From Eq. (5.23), and using the above listed parameter values, the optimal pump spatial width for the production of frequency uncorrelated photons is $w_0 = 682\,54$ μm. Using this value, Eq. (5.22) allows to give a prediction of the joint spectrum for frequency uncorrelated photon pairs, plotted in Fig. 5.5 as a function of λ_s and λ_i. We observe that the spectrum corresponds to a perfect circle with a full width at half maximum (FWHM) $\Delta\lambda_s = 7\,9$ nm, which from Eq. (5.22) is related to ϕ_s by $\Delta\lambda_s = 4(\lambda_s^c)^2\phi_s\nu c \sqrt{\ln 4}\left[(2\nu c)^2 - \phi_s^2(\lambda_s^c)^2\ln 4\right]$. Note that, since we have $\phi_+ = \phi_-$, the down-converted photons exhibit no frequency correlation. The preliminary experimental results give $\Delta\lambda_s^{(\mathrm{exp})} \sim 8$ nm for this configuration, thus the analytical model describes accurately the experiment.

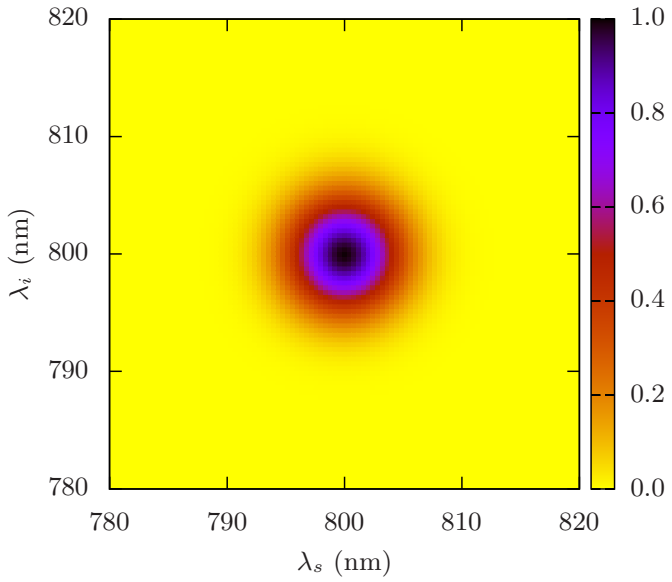

Figure 5.5: Analytically calculated joint spectrum of the signal and idler photons, as a function of λ_s and λ_i for the symmetric filtering configuration. The parameters used are $\alpha = 0\,455$, $L = 300$ μm, $w_0 = 682\,54$ μm, $w_{ss} = w_{si} = 1480$ μm, $n_p = 5\,81 \times 10^{-3}$, $n_s = 5\,61 \times 10^{-3}$, $\pi = 0\,90°$, $B_p = 21\,26$, and $B_{fs} = B_{fi}$.

The result shown in Fig. 5.5 is found for a configuration similar to the one in Refs. [220, 221], where symmetric filtering is performed in both emission channels. However, as discussed in the previous Section 5.2, for the homodyne detection we avoid any filtering process in the signal channel, *i.e.*, in addition to B_{fs} we must take $w_{ss} = 0$. In this situation, the optimal value for the pump spatial width is given by Eq. (5.24), which has certain restrictions on the emission angle π in

order to be real valued. In particular, using the need for a real value of w_0, together with the limitation of a maximum width attainable $w_0^{(max)}$ due to the transverse size of the crystal, we find that $\pi = 17\,11°$. This new angle implies that the refractive indices for the pump and signal (or idler) photons are $n_p = 5\,51 \times 10^{-3}$ and $n_s = 5\,62 \times 10^{-3}$, respectively, and the photons should be collected at angles outside the crystal of $\quad_i = -\quad_s = 29\,25°$. For those parameter values, the optimal pump spatial width [Eq. (5.24)] corresponds to $w_0 = 953\,54\,\mu$m. The predicted joint spectrum of the signal and idler photons for this asymmetric configuration is plotted in Fig. 5.6 as a function of λ_s and λ_i. In this case, the figure obtained is not symmetric anymore since now 1 $\phi_c = 0$ in Eq. (5.19). However, the condition $\phi_+ = \phi_-$ is still fulfilled, *i.e.*, the widths of the diagonals in the figure are equal, which means that the paired photons present no frequency correlations between them.

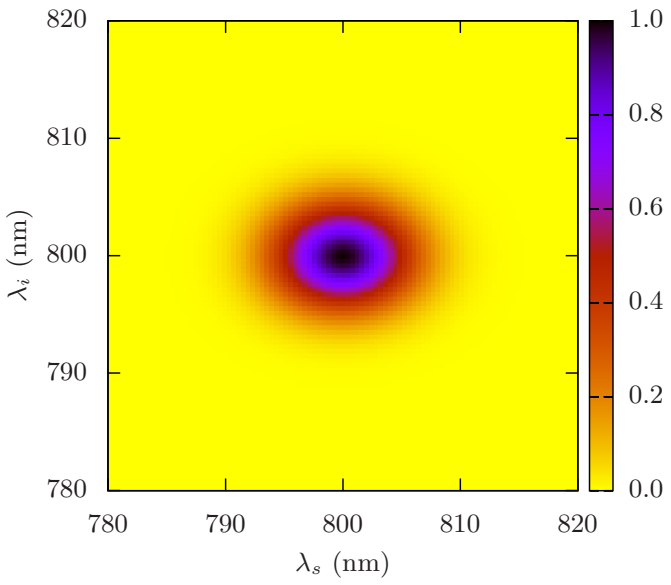

Figure 5.6: Analytically calculated joint spectrum of the signal and idler photons, as a function of λ_s and λ_i for the asymmetric filtering configuration. The parameters used are $\alpha = 0\,455$, $L = 300\ \mu$m, $w_0 = 953\,54\ \mu$m, $w_{ss} = 0$, $w_{si} = 1480\ \mu$m, $n_p = 5\,51 \times 10^{-3}$, $n_s = 5\,62 \times 10^{-3}$, $\pi = 17\,11°$, $B_p = 21\,26$ THz, and $B_{fs} = B_{fi}$.

Eq. (5.26) evaluated with the parameters found for this configuration allows us to obtain an estimation of the spectrum profile of the signal photon entering the

homodyne detection setup. The full width at half maximum of the signal photon spectrum expressed as a function of the wavelength λ_s for this configuration takes the value $\Delta\lambda_s = 9\,6$ nm, which is similar to the one obtained in the symmetric filtering case. As previously mentioned, this value is important since it should match as much as possible with the spectral width of the LO. For this configuration, no experimental measurements of the signal photon bandwidth have been performed, so we can not check the predicted value.

5.3.1 Purity of the signal photon

Though we have seen that the analytical model for the spectrum correctly describes the experimental results, the homodyne detection efficiency obtained in the preliminary experiment (Fig. 5.4) is very low. As stated in Subsection 5.2.2, the homodyne detection efficiency depends on the purity of the signal photon, so a low efficiency indicates that the purity of the signal photon is much lower than unity. This fact is apparently in contradiction with the separability of the joint spectrum that we have observed (Figs. 5.5 and 5.6). Calculating the purity by means of Eq. (5.27), using Eqs. (5.30) and (5.31), for the optimal parameter values corresponding to the symmetric (Fig. 5.5) and asymmetric (Fig. 5.6) configurations, we find $P_s = 0\,275$ and $P_s = 0\,042$, respectively, which are really small values. This means that even preparing the setup to produce frequency uncorrelated photon pairs, signal an idler photons are still correlated through the transverse momentum variables. Actually, this result is consistent with the work done by Osorio *et al.* [236], in which they found, using symmetric filtering in signal and idler channels, that having uncorrelated photon pairs in frequency implies in general a certain degree of correlation in the transverse momentum space, and *vice versa*. Therefore in order to ensure a low degree of correlation in all the variables, the spatial-to-spectral mapping technique is not useful, and one has to focus directly on the purity of the signal photon. As it was shown in Ref. [236], different modifications in the experimental setup could be done to rise the purity, such as increase the down-conversion angle π, or perform strong spatial/spectral filtering in both signal and idler channels. Of course, in the non-symmetric configuration this strong filtering should be performed only in the idler channel.

In order to study the behavior of the purity for different experimental setups, we show in Fig. 5.7 the purity of the signal photon as a function of w_0, for the configurations with small (a) and large (b) output angles, $\pi = 0\,90^\circ$ and $\pi = 17\,11^\circ$, with the corresponding refractive indices for the pump $n_p = 5\,81 \times 10^{-3}$

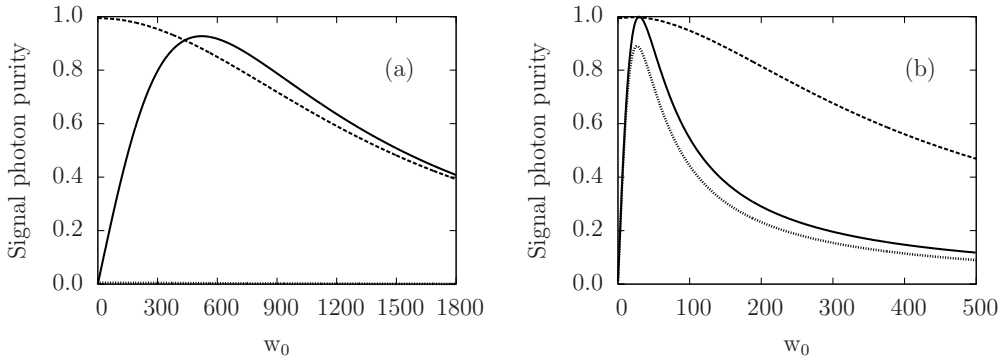

Figure 5.7: Purity of the signal photon detected in coincidence with the idler as a function of the pump spatial width w_0 for the configurations with (a) $\pi = 0\ 90^\circ$ and $n_p = 5\ 81 \times 10^{-3}$, and (b) $\pi = 17\ 11^\circ$ and $n_p = 5\ 51 \times 10^{-3}$. The different line-styles correspond to a symmetric filtering configuration with $w_{ss} = w_{si} = 1480\ \mu$m (solid lines), and asymmetric configurations ($w_{ss} = 0$) with (dashed lines) and without (dotted lines) spectral filtering in the idler channel, using $B_{fi} = B_p$ 10 and B_{fi} , respectively. The rest of the parameters are the same as in Figs. 5.5 and 5.6.

and $n_p = 5\ 51 \times 10^{-3}$, respectively. The solid lines correspond to a symmetric filtering configuration with $w_{ss} = w_{si} = 1480\ \mu$m, while dashed (dotted) lines correspond to an asymmetric configuration, *i.e.*, $w_{ss} = 0$, with (without) spectral filtering in the idler channel, using $B_{fi} = B_p$ 10 ($B_{fi} =$). The rest of parameter are fixed at the same values that in Figs. 5.5 and 5.6: $\alpha = 0\ 455$, $L = 300\ \mu$m, $w_{ss} = 1480\ \mu$m, $n_s = 5\ 62 \times 10^{-3}$, $B_p = 21\ 26$ THz, and B_{fs} .

We observe in the figures that in all the cases there is an optimal pump width $w_0^{(\mathrm{opt})}$ which gives a maximum value for the purity. However, we note that these values of $w_0^{(\mathrm{opt})}$ do not coincide with the optimal widths for the generation of frequency uncorrelated photon pairs w_0, due to do not considering the correlations coming from the transverse momentum variable. For instance, for the asymmetric configuration represented with the dotted line in Fig. 5.7(b), we have obtained that the width $w_0^{(\mathrm{opt})} = 26\ 57\ \mu$m maximizes the purity, while $w_0 = 953\ 54\ \mu$m is the ideal value to erase the spectrum correlations of the photons. Comparing both figures, we also see that in the case with the smaller π angle (a), the purity varies smoothly and its peak value is smaller than in the case with a larger output angle (b), though in the latter, the range of w_0 in which the purity takes higher values is smaller. Moreover, we observe that, for a fixed w_0, as the width of any

of the filters is reduced, in general the purity tends to increase. This behavior is further analyzed in Fig. 5.8, where the purity is plotted as a function of the widths of the spatial, (a)-(b) and spectral (c)-(d) filters for both the signal and the idler channels, and for two different values of the pump waist, $w_0 = 750$ μm in (a)-(c) and $w_0 = w_0^{(max)}$ in (b)-(d). In cases (a)-(b) the spectral filters are assumed to have an infinite width $B_{fs} = B_{fi}$, while in (c)-(d) the spatial filter widths are $w_{ss} = w_{si} = 1480$ μm. The rest of the parameters are the same as in Fig. 5.5. From these figures, we conclude that the narrower the filters, both spatial or spectral, the more pure is the signal photon obtained. Moreover, we note that comparing (a) with (b) and (c) with (d), the behavior of the purity is similar when the pump waist is changed. However, the purity takes higher values in the case where w_0 is smaller (note the difference in the scale of the color bars). Finally, we have observed (not shown in the figure) that when taking $w_{ss} = w_{si} = 0$, the purity drops to zero for any values of the spectral filter widths. This behavior is not observed when we take infinitely wide spectral filters ($B_{fs} = B_{fi}$), so it is clear that some degree of filtering is needed in the signal or idler (or both) channel to have pure single photons.

As a conclusion, the purity of the emitted photons can not be directly manipulated only through the parameter w_0, and a more complex analysis is needed. In this line, a model to describe the purity of the signal photon was presented in Ref. [236], using a symmetric filtering configuration, and different setups were considered to explore the variation of the signal photon purity under parameter variations. In Ref. [237], a complete analysis of the correlation coefficients was performed in order to find the conditions for a full factorizability of the biphoton function.

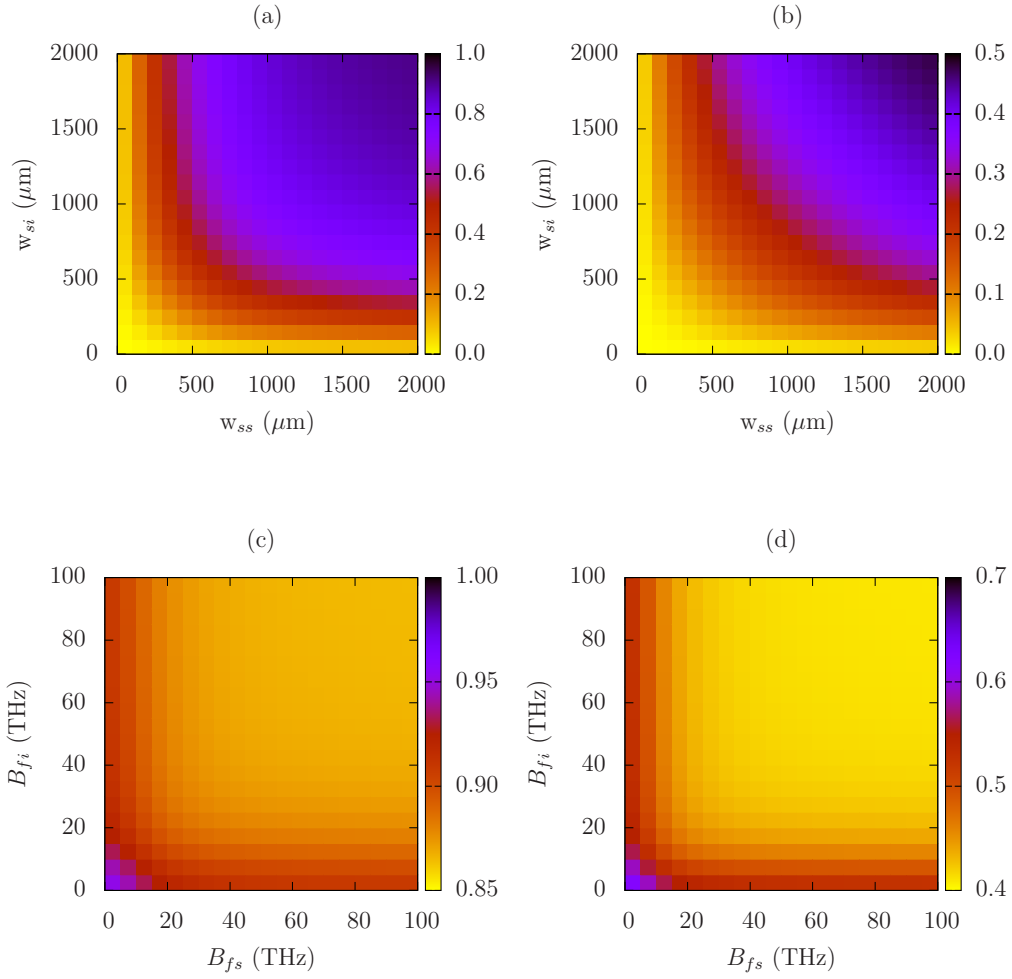

Figure 5.8: Purity of the signal photon as a function of the widths of (a)-(b) the spatial filters, w_{si} and w_{ss}, and the (c)-(d) spectral filters, for two different values of the pump waist: $w_0 = 749$ μm (a)-(c) and $w_0 = w_0^{(max)}$ (b)-(d). In (a)-(b) we use spectral filters with $B_{fs} = B_{fi}$, while in (c)-(d) the spatial filter widths are $w_{ss} = w_{si} = 1480$ μm. The rest of the parameters are the same as in Fig. 5.5.

5.4 Conclusions

In this Chapter, we have used the spatial-to-spectral mapping technique to describe the generation of frequency uncorrelated photon pairs in a SPDC setup and use them as a source of heralded pure single photons. Since the aim of our work is to use one of the two photons for homodyne detection, we have extended the results of Refs. [220, 221] to a general case in which arbitrary spatial or frequency filtering in any of the emission channels can be performed. We have derived explicit expressions for the signal and idler joint spectrum, as well as for the signal spectrum conditioned to the idler detection, and we have obtained the optimal parameter values for the production of frequency uncorrelated photon pairs. In addition, an expression for the purity of the signal photon has been obtained. Next, the analytical model has been compared with preliminary experimental results for the spectrum of the SPDC photons in the symmetric filtering configuration, and a good agreement between the theoretical predictions and the experiment has been found. However, a poor purity for the frequency uncorrelated photon pairs has been obtained. One possible explanation for this result is that, as discussed in Ref. [236], the entanglement between the spatial and spectral degrees of freedom of the biphoton degrades the purity of the signal photon despite having its spectrum uncorrelated from the idler. Therefore, several configurations have been studied in order to analyze the behavior of the signal photon purity under different parameter variations. We have observed that a strong spatial or spectral filtering, either in the signal or in the idler channel, implies an increase of the purity of the signal photon. This increment is even more important if the filtering process is implemented in both channels at the same time, as well as when the pump is tightly focused (small waist w_0) or when the photons are collected at large down-conversion angles (large π).

In conclusion, the spatial-to-spectral mapping technique is useful to control the spectrum of SPDC photons, and allows to obtain frequency uncorrelated photons, but it does not ensure a high purity for heralded single photons, unless a strong spectral filtering is performed. There are still some open questions, such as whether it is possible to find an optimal configuration for the generation of pure single photons without the use of strong filtering, for instance, in the idler channel, which severely limits the heralding efficiency. With this goal, a detailed analysis of the conditions that maximize the purity, obtained in Ref. [237], should be performed.

6

General conclusions

In this Thesis, we have discussed new approaches to implement quantum memories for polarization and frequency encoded single photon qubits, by means of the controlled reversible inhomogeneous broadening (CRIB) [105, 109, 111] and electromagnetically induced transparency (EIT) [61] techniques, respectively. In addition, we have proposed a novel protocol for single-site addressing of neutral atoms in optical lattices based on the subwavelength localization via adiabatic passage (SLAP) technique [180]. Finally, we have developed a theoretical model capable of describing the generation of single photon pairs, through spontaneous parametric down-conversion, with suitable properties to use them in homodyne detection experiments. In this Chapter, we present the main conclusions of these proposals.

In Chapter 2, we have presented two proposals to implement an optical quantum memory for polarization qubits. We have developed an extension of the controlled reversible inhomogeneous broadening (CRIB) technique [105, 109, 111] with V- and Λ-type three-level atoms. Worth to notice, the derivation of the evolution equations has been done in the semiclassical formalism and, due to their linearity, they can also be applied to the single-photon case.

For the V configuration, we have shown the possibility of polarization-encoded single-photon qubit storage without the need of using two separated quantum memories. Under the weak field approximation, the equations describing the evolution of the two optical coherences and the field polarization components are decoupled, thus the system is equivalent to two independent two-level quantum memories. Therefore, this approach, compared with the up to now most proposed polarization quantum memories, allows to avoid the detrimental effects associated with the spatial splitting and recombination of the single photon qubit, and minimizes the efforts required to control the environmental conditions of two spatially

separated quantum memories. Moreover, in both forward and backward retrieval schemes, we have analyzed the effect, in the efficiency and the fidelity of the quantum memory, of homogeneous and inhomogeneous phase noise affecting the atomic coherences of the atoms. We have shown that the addition of a random phase π in the atomic coherences, equal for all the atoms of the medium, that could be due to, for instance, a spatially homogeneous magnetic field, does not affect the efficiency of the retrieval process. However, the fidelity is in general smaller than one. In addition, we have shown that if this phase noise is inhomogeneous, *i.e.*, it affects differently the atoms of the medium, not only the fidelity is lowered, but also the reemission efficiency. This is due to the fact that atoms having different phases are not able to endow a collective rephasing to reemit the previously stored light pulse. To provide quantitative results, we have characterized the influence of the width of the noise distribution, given by a von Mises distribution, on the reemision efficiency as a function of the optical depth. As expected, we have found that the narrower the noise distribution, the higher the reemission efficiency.

For the Λ configuration, we have considered a preparation of the atoms in a coherent superposition of the ground states, *i.e.*, a phaseonium medium [140]. This kind of coherent preparation gives rise to the transparent propagation of a certain combination of the two polarization components with matched envelopes. This effect is caused by the fact that the polarization components are time dependent and, as a consequence, the so-called dark field gradually populates the dark state. Since the evolution of the field components during the propagation, and thus the state at the output of the medium, is determined by the specific preparation of the phaseonium, we have proposed a possible use of this system as a qubit polarization filter. In particular, we have shown that for an input photonic state of the form $\quad_{\text{in}} = a_L\ L\ + a_R\ R$, being L and R , the left and right circular polarization components, propagating in a phasonium medium prepared in a superposition state of the two ground levels $\quad_{\text{at}} = c_1\ 1\ + c_2\ 2$, the state of the polarization qubit at the output is $\quad^{\text{f}}_{\text{out}}\quad c_2\ L\ - c_1\ R$. In addition, we have applied the CRIB technique to recover the part of the photon that is absorbed by the medium, *i.e.*, the superposition state orthogonal to the transmitted one, $\left|\ ^{\text{b}}_{\text{out}}\right\rangle\quad c_1^*\ L\ + c_2^*\ R$. The latter implementation can be devised as a sieve for polarization single photon qubits, or considering both the transmitted and recovered components, a tunable polarization qubit splitter whose basis is determined by the atomic amplitudes c_1 and c_2. Finally, we have also demonstrated the realization of a polarization quantum memory in this coherently prepared medium,

by adding a position dependent phase in the ground state coherence. In this situation, the polarization components can not evolve to populate the dark state, since it is different at each position. Thus, we have demonstrated that the field is reversibly mapped into the atomic coherences, and it can be retrieved using the CRIB technique with high efficiency and fidelity. It is important to note that, for both V and Λ configurations, we have numerically integrated the full optical Bloch equations, governing the evolution of the system, to validate the analytical approach, obtaining a good agreement between the analytic results and the numerical simulations.

In Chapter 3, we have addressed the storage of frequency encoded single photon qubits, *i.e.*, a two-color quantum memory, using the electromagnetically induced transparency (EIT) technique [61] in a double-Λ-type atomic ensemble. We have considered an atomic configuration where (i) the population is excited only by the single photon components, and (ii) one of the Λ schemes is detuned far from the one photon resonance. This configuration allows to avoid envelope matching effects arising usually in the resonant case. We have derived and analytically solved the evolution equations in a full quantum mechanical treatment, and we have shown that, under certain conditions, the two frequency components propagate with the same group velocity. In this situation, the field components are able to exchange energy, and undergo complementary sinusoidal oscillations as they propagate. Specifically, we have obtained that the input frequency superposition state of the single photon is periodically recovered at those positions z of the medium fulfilling $\mathrm{Re}(\alpha)z = 2\nu n$ (n $\mathbb{Z}$), being α a parameter proportional to the ratio between the density of the medium and the detuning of the far detuned control field. We have analyzed the dependence on the specific initial superposition state and the phase between the two strong control fields in this propagation dynamics, and we have found that for appropriate parameter values the oscillations both in the phase and in the intensity of the frequency components are suppressed, *i.e.*, they propagate as matched amplitudes. Moreover, we have numerically demonstrated, using realistic parameter values, the storage and subsequent retrieval of a frequency superposition state by turning off and on the control fields. The calculated total efficiency and conditional fidelity are $\eta = 91\ 01\%$ and $F_c = 99\ 69\%$, respectively, while the storage time has been fixed at $\sim 0\ 35\,\mu$s.

Next, in Chapter 4, we have proposed a new the single site addressing (SSA) protocol of ultracold Λ-type three-level atoms in an optical lattice by selectively changing their internal state, depending on their position. This is achieved by

means of the subwavelength localization via adiabatic passage (SLAP) technique [180], a variation of stimulated Raman adiabatic passage (STIRAP) [181], in which the pump field has a spatial profile with a node at the position to address. We have derived analytic expressions for the FWHM of the addressing probability distribution $(\Delta x)_{\rm SLAP}$, and obtained the conditions for the parameter values in order to optimally address the target site. In particular, we have obtained expressions of the addressing efficiency, defined as the probability of transferring all the atoms of the lattice except the one at the addressed site, as a function of $(\Delta x)_{\rm SLAP}$. In order to have an assessment of the performance of our addressing protocol, we have established both qualitative and quantitative comparisons with other SSA proposals [184, 185, 206 213].

On the one hand, compared with the group of techniques reported in Refs. [206 213], which are based on coherent population trapping (CPT) [59, 160, 182, 183], we have shown that the adiabatic following of the dark state allows for a higher addressing resolution using the same intensity and focusing requirements of the addressing fields. As a consequence, the addressing efficiency is higher in the SLAP case, for smaller values of the intensity ratio R between the pump and the Stokes fields ($R < 50$), than for the CPT technique. These results have been verified by numerically integrating the density matrix equations using parameter values corresponding to the D1 line of ^{87}Rb with state-of-the art optical lattices. For instance, for $R = 10$ we have obtained addressing efficiencies of $\eta^{\rm SLAP} = 0\ 95$ and $\eta^{\rm CPT} = 0\ 56$, for the SLAP and CPT techniques, respectively. We have also pointed out additional advantages of the SLAP based SSA technique in front of the CPT based techniques, such as robustness of the addressing process against parameter variations, coherence of the population transfer mechanism, and the absence of photon induced recoil.

On the other hand, we have compared the SSA via SLAP technique with the recent SSA proposal in which a strong off-resonant focused beam and a microwave (MW) chirped pulse are used to produce an adiabatic spin-flip in the target atoms [184, 185]. First, since in the two proposals the fields that perform the internal state change belong to different domains, optical (MHz) in the SLAP and MW (kHz) in spin-flip approach, the adiabaticity requirements impose different timescales for the interaction times. In particular, we have shown that, by fixing similar widths of the addressing probability distribution for both techniques $(\Delta x) \sim 300$ nm, the SSA via SLAP technique works even with interaction times almost three orders of magnitude shorter than in the spin-flip approach. In ad-

dition, we have found that, for similar focusing requirements of the addressing beams, and using $R = 1$, the SLAP technique provides a similar addressing resolution than the adiabatic spin-flip technique, $(\Delta x)_{\mathrm{SLAP}} = 330\ 66$ nm. Note that in our proposal, by increasing the ratio R, the FWHM of the addressing probability distribution can be further reduced: $R = 10$ implies $(\Delta x)_{\mathrm{SLAP}} = 181\ 86$ nm and for $R = 100$ we obtain $(\Delta x)_{\mathrm{SLAP}} = 100\ 82$ nm.

Finally, in Chapter 5, we have developed a theoretical model for the production of pure and heralded single photons with controllable bandwidths, needed in a wide variety of quantum information applications, using a spontaneous parametric down-conversion (SPDC) setup. We have extended the spatial-to-spectral mapping technique [219 221]to cases in which homodyne detection of one of the photons of the pair, the signal, is performed, *i.e.*, using neither spatial nor spectral filtering in the signal channel. First, we have considered the joint spectrum of the signal and idler photons, and we have obtained an expression for the optimal pump waist w_0 that allows for the production of heralded and spectrally uncorrelated photon pairs. This means that, for this optimal parameter, the joint spectrum is a separable function of the signal and idler frequencies. In addition, we have derived analytical expressions for the spectrum and the purity of the signal photon conditioned to the idler detection. Next, we have used these expressions and experimental parameter values to predict the width of the signal photon spectrum distribution and the purity for two spatial filtering widths and emission angles: (i) $\mathrm{w}_{ss} = 1480\,\mu$m and $\pi = 0\ 90^\circ$, and (ii) $\mathrm{w}_{ss} = 0$ and $\pi = 17\ 11^\circ$. Those cases correspond to optimal pump waists of $\mathrm{w}_0 = 682\ 54\,\mu$m and $\mathrm{w}_0 = 953\ 54\,\mu$m, respectively, and give similar full widths at half maximum (FWHM) for the signal photon spectrum distribution, $\Delta\lambda_s = 7\ 9$ nm and $\Delta\lambda_s = 9\ 6$ nm, respectively. In the former case (i), for which we have experimental data available corresponding to $\Delta\lambda_s^{(\mathrm{exp})} \sim 8$ nm, we conclude that the analytical value gives a reliable prediction of the signal photon spectrum distribution. Interestingly, the obtained values for the purity of the signal photons P_s taking into account the optimal parameters are much smaller than expected. In particular, we have found $P_s = 0\ 275$ and $P_s = 0\ 042$ for the the situations (i) and (ii), respectively. Thus, different sets of parameters have been used to explore the behavior of the purity under different experimental situations. First, we have obtained that, representing the purity as a function of the pump waist, the maximum does not occur at w_0, corresponding to the production of spectrally uncorrelated photons. Moreover, the purity increases for the case of using a larger angle (ii), as well as when strong filtering is per-

formed. Second, we have studied the purity as a function of spectral and spatial filter widths, for two different values of the pump waist, and we have observed that the smaller the pump waist the higher the purity. From all these results we have concluded that, in agreement with previous related works [236, 237], the photons of each pair, although being spectrally pure, are correlated through the spatial degrees of freedom. Moreover, we have also concluded that in order to obtain truly pure single photons, the usual approach of performing strong filtering in the emission channels, specially in frequency, is apparently the best option, although this dramatically reduces the count rate.

Bibliography

[1] N. Gisin, G. Ribordy, W. Tittel, and H. Zbinden. *Quantum cryptography.* Reviews of Modern Physics **74**, 145 (2002). doi:10.1103/RevModPhys.74.145.

[2] N. D. Mermin. *Quantum Computer Science Ch. 3*, (Cambridge University Press 2007).

[3] R. Ursin, F. Tiefenbacher, T. Schmitt-Manderbach, H. Weier, T. Scheidl, M. Lindenthal, B. Blauensteiner, T. Jennewein, J. Perdigues, P. Trojek, *et al. Entanglement-based quantum communication over 144 km.* Nature Physics **3**, 481 (2007). doi:10.1038/nphys629.

[4] H.-J. Briegel, W. Dur, J. I. Cirac, and P. Zoller. *Quantum Repeaters: The Role of Imperfect Local Operations in Quantum Communication.* Physical Review Letters **81**, 5932 (1998). doi:10.1103/PhysRevLett.81.5932.

[5] N. Sangouard, C. Simon, H. de Riedmatten, and N. Gisin. *Quantum repeaters based on atomic ensembles and linear optics.* Reviews of Modern Physics **83**, 33 (2011). doi:10.1103/RevModPhys.83.33.

[6] M. Zukowski, A. Zeilinger, M. A. Horne, and A. K. Ekert. *"Event-ready-detectors" Bell experiment via entanglement swapping.* Physical Review Letters **71**, 4287 (1993). doi:10.1103/PhysRevLett.71.4287.

[7] J. S. Bell. *On the Einstein-Podolsky-Rosen paradox.* Physics **1**, 195 (1964).

[8] J. S. Bell. *On the Problem of Hidden Variables in Quantum Mechanics.* Reviews of Modern Physics **38**, 447 (1966). doi:10.1103/RevModPhys.38.447.

[9] C. Simon and W. T. M. Irvine. *Robust Long-Distance Entanglement and a Loophole-Free Bell Test with Ions and Photons.* Physical Review Letters **91**, 110405 (2003). doi:10.1103/PhysRevLett.91.110405.

[10] H. Buhrman, R. Cleve, S. Massar, and R. de Wolf. *Nonlocality and communication complexity.* Reviews of Modern Physics **82**, 665 (2010). doi:10.1103/RevModPhys.82.665.

[11] C. K. Hong and L. Mandel. *Experimental realization of a localized one-photon state.* Physical Review Letters **56**, 58 (1986). doi:10.1103/PhysRevLett.56.58.

[12] E. Knill, R. Laflamme, and G. J. Milburn. *A scheme for efficient quantum computation with linear optics.* Nature **409**, 46 (2001). doi:10.1038/35051009.

[13] P. Kok, W. J. Munro, K. Nemoto, T. C. Ralph, J. P. Dowling, and G. J. Milburn. *Linear optical quantum computing with photonic qubits.* Reviews of Modern Physics **79**, 135 (2007). doi:10.1103/RevModPhys.79.135.

[14] N. Sangouard, C. Simon, J. Minář, H. Zbinden, H. de Riedmatten, and N. Gisin. *Long-distance entanglement distribution with single-photon sources.* Physical Review A **76**, 050301 (2007). doi:10.1103/PhysRevA.76.050301.

[15] S. Chen, Y.-A. Chen, T. Strassel, Z.-S. Yuan, B. Zhao, J. Schmiedmayer, and J.-W. Pan. *Deterministic and Storable Single-Photon Source Based on a Quantum Memory.* Physical Review Letters **97**, 173004 (2006). doi:10.1103/PhysRevLett.97.173004.

[16] D. N. Matsukevich, T. Chanelière, S. D. Jenkins, S.-Y. Lan, T. A. B. Kennedy, and A. Kuzmich. *Deterministic Single Photons via Conditional Quantum Evolution.* Physical Review Letters **97**, 013601 (2006). doi:10.1103/PhysRevLett.97.013601.

[17] J. Appel, O. D. Windpassinger, P. J., U. B. Hoff, N. Kjffirgaard, and P. E. S. *Mesoscopic atomic entanglement for precision measurements beyond the standard quantum limit.* Proc. Natl Acad. Sci. USA **106**, 10960 (2009). doi:doi:10.1073/pnas.0901550106.

[18] W. Wasilewski, K. Jensen, H. Krauter, J. J. Renema, M. V. Balabas, and E. S. Polzik. *Quantum Noise Limited and Entanglement-Assisted Magnetometry.* Physical Review Letters **104**, 133601 (2010). doi:10.1103/PhysRevLett.104.133601.

[19] F. Wolfgramm, A. Cerè, F. A. Beduini, A. Predojević, M. Koschorreck, and M. W. Mitchell. *Squeezed-Light Optical Magnetometry.* Physical Review Letters **105**, 053601 (2010). doi:10.1103/PhysRevLett.105.053601.

[20] J. Appel, E. Figueroa, D. Korystov, M. Lobino, and A. I. Lvovsky. *Quantum Memory for Squeezed Light.* Physical Review Letters **100**, 093602 (2008). doi:10.1103/PhysRevLett.100.093602.

[21] K. Honda, D. Akamatsu, M. Arikawa, Y. Yokoi, K. Akiba, S. Nagatsuka, T. Tanimura, A. Furusawa, and M. Kozuma. *Storage and Retrieval of a Squeezed Vacuum.* Physical Review Letters **100**, 093601 (2008). doi:10.1103/PhysRevLett.100.093601.

[22] A. Kuzmich, L. Mandel, and N. P. Bigelow. *Generation of Spin Squeezing via Continuous Quantum Nondemolition Measurement.* Physical Review Letters **85**, 1594 (2000). doi:10.1103/PhysRevLett.85.1594.

[23] B. Julsgaard, A. Kozhekin, and E. Polzik. *Experimental long-lived entanglement of two macroscopic objects.* Nature **413**, 400 (2001). doi:10.1038/35096524.

[24] T. Fernholz, H. Krauter, K. Jensen, J. F. Sherson, A. S. Sffrensen, and E. S. Polzik. *Spin Squeezing of Atomic Ensembles via Nuclear-Electronic Spin Entanglement.* Physical Review Letters **101**, 073601 (2008). doi:10.1103/PhysRevLett.101.073601.

[25] A. Uhlmann. *The "transition probability" in the state space of a*-algebra.* Reports on Mathematical Physics **9**, 273 (1976).

[26] W. Tittel, M. Afzelius, T. Chanelière, R. L. Cone, S. Kroll, S. A. Moiseev, and M. Sellars. *Photon-echo quantum memory in solid state systems.* Laser & Photonics Reviews **4**, 244 (2010). doi:10.1002/lpor.200810056.

[27] N. Sangouard, C. Simon, M. Afzelius, and N. Gisin. *Analysis of a quantum memory for photons based on controlled reversible inhomogeneous broadening.* Physical Review A **75**, 032327 (2007). doi:10.1103/PhysRevA.75.032327.

[28] K. Hammerer, A. S. Sffrensen, and E. S. Polzik. *Quantum interface between light and atomic ensembles.* Reviews of Modern Physics **82**, 1041 (2010). doi:10.1103/RevModPhys.82.1041.

[29] M. P. Hedges, J. J. Longdell, Y. Li, and M. J. Sellars. *Efficient quantum memory for light.* Nature **465**, 1052 (2010). doi:10.1038/nature09081.

[30] X. H. Bao, A. Reingruber, P. Dietrich, J. Rui, A. Duck, T. Strassel, L. Li, N. Liu, B. Zhao, and J. Pan. *Efficient and long-lived quantum memory with cold atoms inside a ring cavity.* Nature Physics (2012). doi:10.1038/nphys2324.

[31] H. P. Specht, C. Nolleke, A. Reiserer, M. Uphoff, E. Figueroa, S. Ritter, and G. Rempe. *A single-atom quantum memory.* Nature **473**, 190 (2011). doi:10.1038/nature09997.

[32] M. Razavi, M. Piani, and N. Lutkenhaus. *Quantum repeaters with imperfect memories: Cost and scalability.* Physical Review A **80**, 032301 (2009). doi:10.1103/PhysRevA.80.032301.

[33] N. Sangouard, C. Simon, B. Zhao, Y. Chen, H. de Riedmatten, J. Pan, and N. Gisin. *Robust and efficient quantum repeaters with atomic ensembles and linear optics.* Physical Review A **77**, 062301 (2008). doi:10.1103/PhysRevA.77.062301.

[34] J. J. Longdell, E. Fraval, M. J. Sellars, and N. B. Manson. *Stopped Light with Storage Times Greater than One Second Using Electromagnetically Induced Transparency in a Solid.* Physical Review Letters **95**, 063601 (2005). doi:10.1103/PhysRevLett.95.063601.

[35] J. Nunn, K. Reim, K. C. Lee, V. O. Lorenz, B. J. Sussman, I. A. Walmsley, and D. Jaksch. *Multimode Memories in Atomic Ensembles.* Physical Review Letters **101**, 260502 (2008). doi:10.1103/PhysRevLett.101.260502.

[36] M. Afzelius, C. Simon, H. de Riedmatten, and N. Gisin. *Multimode quantum memory based on atomic frequency combs.* Physical Review A **79**, 052329 (2009). doi:10.1103/PhysRevA.79.052329.

[37] C. Simon, H. de Riedmatten, M. Afzelius, N. Sangouard, H. Zbinden, and N. Gisin. *Quantum Repeaters with Photon Pair Sources and Multimode Memories.* Physical Review Letters **98**, 190503 (2007). doi:10.1103/PhysRevLett.98.190503.

[38] O. A. Collins, S. D. Jenkins, A. Kuzmich, and T. A. B. Kennedy. *Multiplexed Memory-Insensitive Quantum Repeaters.* Physical Review Letters **98**, 060502 (2007). doi:10.1103/PhysRevLett.98.060502.

[39] G. Hétet, J. J. Longdell, M. J. Sellars, P. K. Lam, and B. C. Buchler. *Multimodal Properties and Dynamics of Gradient Echo Quantum Memory.* Physical Review Letters **101**, 203601 (2008). doi:10.1103/PhysRevLett.101.203601.

[40] M. Hosseini, B. M. Sparkes, G. Hétet, J. J. Longdell, P. K. Lam, and B. C. Buchler. *Coherent optical pulse sequencer for quantum applications.* Nature **461**, 241 (2009). doi:10.1038/nature08325.

[41] I. Usmani, M. Afzelius, H. d. Riedmatten, and N. Gisin. *Mapping multiple photonic qubits into and out of one solid-state atomic ensemble.* Nature Communications **1**, 12 (2010). doi:10.1038/ncomms1010.

[42] M. Bonarota, J. Le Gouet, and T. Chanelière. *Highly multimode storage in a crystal.* New Journal of Physics **13**, 013013 (2011). doi:10.1088/1367-2630/13/1/013013.

[43] D. V. Vasilyev, I. V. Sokolov, and E. S. Polzik. *Quantum memory for images: A quantum hologram.* Physical Review A **77**, 020302 (2008). doi:10.1103/PhysRevA.77.020302.

[44] H.-N. Dai, H. Zhang, S.-J. Yang, T.-M. Zhao, J. Rui, Y.-J. Deng, L. Li, N.-L. Liu, S. Chen, X.-H. Bao, X.-M. Jin, B. Zhao, and J.-W. Pan. *Holographic Storage of Biphoton Entanglement.* Physical Review Letters **108**, 210501 (2012). doi:10.1103/PhysRevLett.108.210501.

[45] K. Surmacz, J. Nunn, K. Reim, K. C. Lee, V. O. Lorenz, B. Sussman, I. A. Walmsley, and D. Jaksch. *Efficient spatially resolved multimode quantum memory.* Physical Review A **78**, 033806 (2008). doi:10.1103/PhysRevA.78.033806.

[46] E. Saglamyurek, N. Sinclair, J. Jin, J. A. Slater, D. Oblak, F. Bussières, M. George, R. Ricken, W. Sohler, and W. Tittel. *Broadband waveguide quantum memory for entangled photons.* Nature **469**, 512 (2011). doi:10.1038/nature09719.

[47] K. F. Reim, J. Nunn, V. O. Lorenz, B. J. Sussman, K. C. Lee, N. K. Langford, D. Jaksch, and I. A. Walmsley. *Towards high-speed optical quantum memories*. Nature Photonics **4**, 218 (2010). doi:10.1038/nphoton.2010.30.

[48] B. Lauritzen, J. Minář, H. de Riedmatten, M. Afzelius, N. Sangouard, C. Simon, and N. Gisin. *Telecommunication-Wavelength Solid-State Memory at the Single Photon Level*. Physical Review Letters **104**, 080502 (2010). doi:10.1103/PhysRevLett.104.080502.

[49] C. Clausen, I. Usmani, F. Bussières, N. Sangouard, M. Afzelius, H. d. Riedmatten, and N. Gisin. *Quantum storage of photonic entanglement in a crystal*. Nature **469**, 508 (2011). doi:10.1038/nature09662.

[50] C. Simon, M. Afzelius, J. Appel, A. Boyer de la Giroday, S. J. Dewhurst, N. Gisin, C. Y. Hu, F. Jelezko, S. Kroll, J. H. Muller, J. Nunn, E. S. Polzik, J. G. Rarity, H. De Riedmatten, W. Rosenfeld, A. J. Shields, N. Skold, R. M. Stevenson, R. Thew, I. A. Walmsley, M. C. Weber, H. Weinfurter, J. Wrachtrup, and R. J. Young. *Quantum memories A review based on the European integrated project "Qubit Applications (QAP)"*. The European Physical Journal D - Atomic, Molecular, Optical and Plasma Physics **58**, 1 (2010). doi:10.1140/epjd/e2010-00103-y.

[51] T. B. Pittman, B. C. Jacobs, and J. D. Franson. *Single photons on pseudodemand from stored parametric down-conversion*. Physical Review A **66**, 042303 (2002). doi:10.1103/PhysRevA.66.042303.

[52] T. B. Pittman and J. D. Franson. *Cyclical quantum memory for photonic qubits*. Physical Review A **66**, 062302 (2002). doi:10.1103/PhysRevA.66.062302.

[53] P. M. Leung and T. C. Ralph. *Quantum memory scheme based on optical fibers and cavities*. Physical Review A **74**, 022311 (2006). doi:10.1103/PhysRevA.74.022311.

[54] X. Maıtre, E. Hagley, G. Nogues, C. Wunderlich, P. Goy, M. Brune, J. M. Raimond, and S. Haroche. *Quantum Memory with a Single Photon in a Cavity*. Physical Review Letters **79**, 769 (1997). doi:10.1103/PhysRevLett.79.769.

[55] T. Tanabe, M. Notomi, E. Kuramochi, A. Shinya, and H. Taniyama. *Trapping and delaying photons for one nanosecond in an ultrasmall high-Q photonic-crystal nanocavity.* Nature Photonics **1**, 49 (2007). doi:10.1038/nphoton.2006.51.

[56] T. Tanabe, M. Notomi, H. Taniyama, and E. Kuramochi. *Dynamic Release of Trapped Light from an Ultrahigh-Q Nanocavity via Adiabatic Frequency Tuning.* Physical Review Letters **102**, 043907 (2009). doi:10.1103/PhysRevLett.102.043907.

[57] B. Julsgaard, J. Sherson, J. I. Cirac, J. Fiurášek, and E. S. Polzik. *Experimental demonstration of quantum memory for light.* Nature **432**, 482 (2004). doi:10.1038/nature03064.

[58] J. F. Sherson, H. Krauter, R. K. Olsson, B. Julsgaard, K. Hammerer, I. Cirac, and E. S. Polzik. *Quantum teleportation between light and matter.* Nature **443**, 557 (2006). doi:10.1038/nature05136.

[59] S. Harris. *Electromagnetically induced transparency.* Physics Today **50**, 36 (1997). doi:10.1063/1.881806.

[60] Z. Dutton, N. Ginsberg, C. Slowe, and L. Hau. *The art of taming light: ultra-slow and stopped light.* Europhysics News **35**, 33 (2004). doi:10.1051/epn:2004201.

[61] M. Fleischhauer, A. Imamoglu, and J. P. Marangos. *Electromagnetically induced transparency: Optics in coherent media.* Reviews of Modern Physics **77**, 633 (2005). doi:10.1103/RevModPhys.77.633.

[62] S. E. Harris, J. E. Field, and A. Kasapi. *Dispersive properties of electromagnetically induced transparency.* Physical Review A **46**, R29 (1992). doi:10.1103/PhysRevA.46.R29.

[63] L. Hau, S. Harris, Z. Dutton, and C. Behroozi. *Light speed reduction to 17 metres per second in an ultracold atomic gas.* Nature **397**, 594 (1999). doi:10.1038/17561.

[64] M. Fleischhauer and M. D. Lukin. *Dark-State Polaritons in Electromagnetically Induced Transparency.* Physical Review Letters **84**, 5094 (2000). doi:10.1103/PhysRevLett.84.5094.

[65] C. Liu, Z. Dutton, C. H. Behroozi, and L. V. Hau. *Observation of coherent optical information storage in an atomic medium using halted light pulses.* Nature **409**, 490 (2001). doi:10.1038/35054017.

[66] D. F. Phillips, A. Fleischhauer, A. Mair, R. L. Walsworth, and M. D. Lukin. *Storage of Light in Atomic Vapor.* Physical Review Letters **86**, 783 (2001). doi:10.1103/PhysRevLett.86.783.

[67] M. D. Lukin. *Colloquium: Trapping and manipulating photon states in atomic ensembles.* Reviews of Modern Physics **75**, 457 (2003). doi:10.1103/RevModPhys.75.457.

[68] M. Fleischhauer and M. D. Lukin. *Quantum memory for photons: Dark-state polaritons.* Physical Review A **65**, 022314 (2002). doi:10.1103/PhysRevA.65.022314.

[69] A. B. Matsko, Y. V. Rostovtsev, O. Kocharovskaya, A. S. Zibrov, and M. O. Scully. *Nonadiabatic approach to quantum optical information storage.* Physical Review A **64**, 043809 (2001). doi:10.1103/PhysRevA.64.043809.

[70] F. Beil, J. Klein, G. Nikoghosyan, and T. Halfmann. *Electromagnetically induced transparency and retrieval of light pulses in a Λ-type and a V-type level scheme in* $Pr^3+:Y_2SiO_5$. Journal of Physics B: Atomic, Molecular and Optical Physics **41**, 074001 (2008). doi:10.1088/0953-4075/41/7/074001.

[71] A. Mair, J. Hager, D. F. Phillips, R. L. Walsworth, and M. D. Lukin. *Phase coherence and control of stored photonic information.* Physical Review A **65**, 031802 (2002). doi:10.1103/PhysRevA.65.031802.

[72] M. D. Eisaman, A. André, F. Massou, M. Fleischhauer, A. S. Zibrov, and M. D. Lukin. *Electromagnetically induced transparency with tunable single-photon pulses.* Nature **438**, 837 (2005). doi:10.1038/nature04327.

[73] I. Novikova, A. V. Gorshkov, D. F. Phillips, A. S. Sffrensen, M. D. Lukin, and R. L. Walsworth. *Optimal Control of Light Pulse Storage and Retrieval.* Physical Review Letters **98**, 243602 (2007). doi:10.1103/PhysRevLett.98.243602.

[74] I. Novikova, N. B. Phillips, and A. V. Gorshkov. *Optimal light storage with full pulse-shape control.* Physical Review A **78**, 021802 (2008). doi:10.1103/PhysRevA.78.021802.

[75] Y. Cho and Y. Kim. *Atomic vapor quantum memory for a photonic polarization qubit.* Optics Express **18**, 25786 (2010). doi:10.1364/OE.18.025786.

[76] K. S. Choi, H. Deng, J. Laurat, and H. J. Kimble. *Mapping photonic entanglement into and out of a quantum memory.* Nature **452**, 67 (2008). doi:10.1038/nature06670.

[77] R. M. Camacho, P. K. Vudyasetu, and J. C. Howell. *Four-wave-mixing stopped light in hot atomic rubidium vapour.* Nature Photonics **3**, 103 (2009). doi:10.1038/nphoton.2008.290.

[78] K. S. Choi, A. Goban, S. B. Papp, S. J. v. Enk, and H. J. Kimble. *Entanglement of spin waves among four quantum memories.* Nature **468**, 412 (2010). doi:10.1038/nature09568.

[79] A. Javan, O. Kocharovskaya, H. Lee, and M. O. Scully. *Narrowing of electromagnetically induced transparency resonance in a Doppler-broadened medium.* Physical Review A **66**, 013805 (2002). doi:10.1103/PhysRevA.66.013805.

[80] C. Mewes and M. Fleischhauer. *Two-photon linewidth of light "stopping" via electromagnetically induced transparency.* Physical Review A **66**, 033820 (2002). doi:10.1103/PhysRevA.66.033820.

[81] M. T. L. Hsu, G. Hétet, O. Glockl, J. J. Longdell, B. C. Buchler, H.-A. Bachor, and P. K. Lam. *Quantum Study of Information Delay in Electromagnetically Induced Transparency.* Physical Review Letters **97**, 183601 (2006). doi:10.1103/PhysRevLett.97.183601.

[82] M. D. Lukin, M. Fleischhauer, A. S. Zibrov, H. G. Robinson, V. L. Velichansky, L. Hollberg, and M. O. Scully. *Spectroscopy in Dense Coherent Media: Line Narrowing and Interference Effects.* Physical Review Letters **79**, 2959 (1997). doi:10.1103/PhysRevLett.79.2959.

[83] N. B. Phillips, A. V. Gorshkov, and I. Novikova. *Light storage in an optically thick atomic ensemble under conditions of electromagnetically induced transparency and four-wave mixing.* Physical Review A **83**, 063823 (2011). doi:10.1103/PhysRevA.83.063823.

[84] A. E. Kozhekin, K. Mfflmer, and E. Polzik. *Quantum memory for light.* Physical Review A **62**, 033809 (2000). doi:10.1103/PhysRevA.62.033809.

[85] K. F. Reim, P. Michelberger, K. C. Lee, J. Nunn, N. K. Langford, and I. A. Walmsley. *Single-Photon-Level Quantum Memory at Room Temperature.* Physical Review Letters **107**, 053603 (2011). doi:10.1103/PhysRevLett.107.053603.

[86] K. F. Reim, J. Nunn, X.-M. Jin, P. S. Michelberger, T. F. M. Champion, D. G. England, K. C. Lee, W. S. Kolthammer, N. K. Langford, and I. A. Walmsley. *Multipulse Addressing of a Raman Quantum Memory: Configurable Beam Splitting and Efficient Readout.* Physical Review Letters **108**, 263602 (2012). doi:10.1103/PhysRevLett.108.263602.

[87] M. G. Raymer and J. Mostowski. *Stimulated Raman scattering: Unified treatment of spontaneous initiation and spatial propagation.* Physical Review A **24**, 1980 (1981). doi:10.1103/PhysRevA.24.1980.

[88] J. Nunn, I. A. Walmsley, M. G. Raymer, K. Surmacz, F. C. Waldermann, Z. Wang, and D. Jaksch. *Mapping broadband single-photon wave packets into an atomic memory.* Physical Review A **75**, 011401 (2007). doi:10.1103/PhysRevA.75.011401.

[89] O. S. Mishina, D. V. Kupriyanov, J. H. Muller, and E. S. Polzik. *Spectral theory of quantum memory and entanglement via Raman scattering of light by an atomic ensemble.* Physical Review A **75**, 042326 (2007). doi:10.1103/PhysRevA.75.042326.

[90] O. S. Mishina, N. V. Larionov, A. S. Sheremet, I. M. Sokolov, and D. V. Kupriyanov. *Stimulated Raman process in a scattering medium applied to the quantum memory scheme.* Physical Review A **78**, 042313 (2008). doi:10.1103/PhysRevA.78.042313.

[91] L. Duan, M. Lukin, I. Cirac, and P. Zoller. *Long-distance quantum communication with atomic ensembles and linear optics.* Nature **414**, 413 (2001). doi:10.1038/35106500.

[92] R. Zhao, Y. O. Dudin, S. D. Jenkins, C. J. Campbell, D. N. Matsukevich, T. a. B. Kennedy, and A. Kuzmich. *Long-lived quantum memory.* Nature Physics **5**, 100 (2009). doi:10.1038/nphys1152.

[93] A. Kuzmich, W. P. Bowen, A. D. Boozer, A. Boca, C. W. Chou, L. M. Duan, and H. J. Kimble. *Generation of nonclassical photon pairs for scalable quantum communication with atomic ensembles.* Nature (2003).

[94] D. N. Matsukevich, T. Chanelière, M. Bhattacharya, S.-Y. Lan, S. D. Jenkins, T. A. B. Kennedy, and A. Kuzmich. *Entanglement of a Photon and a Collective Atomic Excitation.* Physical Review Letters **95**, 040405 (2005). doi:10.1103/PhysRevLett.95.040405.

[95] J. Laurat, C. Chou, H. Deng, K. Choi, D. Felinto, H. Riedmatten, and H. Kimble. *Towards experimental entanglement connection with atomic ensembles in the single excitation regime.* New Journal of Physics **9**, 207 (2007). doi:10.1088/1367-2630/9/6/207.

[96] D. N. Matsukevich and A. Kuzmich. *Quantum State Transfer Between Matter and Light.* Science **306**, 663 (2004). doi:10.1126/science.1103346.

[97] C. W. Chou, H. d. Riedmatten, D. Felinto, S. V. Polyakov, S. J. v. Enk, and H. J. Kimble. *Measurement-induced entanglement for excitation stored in remote atomic ensembles.* Nature **438**, 828 (2005). doi:10.1038/nature04353.

[98] T. Chanelière, D. N. Matsukevich, S. D. Jenkins, S. Lan, T. a. B. Kennedy, and A. Kuzmich. *Storage and retrieval of single photons transmitted between remote quantum memories.* Nature **438**, 833 (2005). doi:10.1038/nature04315.

[99] H. Tanji, S. Ghosh, J. Simon, B. Bloom, and V. Vuletić. *Heralded Single-Magnon Quantum Memory for Photon Polarization States.* Physical Review Letters **103**, 043601 (2009). doi:10.1103/PhysRevLett.103.043601.

[100] Y.-A. Chen, S. Chen, Z.-S. Yuan, B. Zhao, C.-S. Chuu, J. Schmiedmayer, and J.-W. Pan. *Memory-built-in quantum teleportation with photonic and atomic qubits.* Nature Physics **4**, 103 (2008). doi:10.1038/nphys832.

[101] J. Simon, H. Tanji, J. K. Thompson, and V. Vuletic. *Interfacing Collective Atomic Excitations and Single Photons.* Physical Review Letters **98**, 183601 (2007). doi:10.1103/PhysRevLett.98.183601.

[102] N. A. Kurnit, I. D. Abella, and S. R. Hartmann. *Observation of a Photon Echo.* Physical Review Letters **13**, 567 (1964). doi:10.1103/PhysRevLett.13.567.

[103] E. L. Hahn. *Spin Echoes.* Phys. Rev. **80**, 580 (1950). doi:10.1103/PhysRev.80.580.

[104] J. Ruggiero, J.-L. Le Gouet, C. Simon, and T. Chanelière. *Why the two-pulse photon echo is not a good quantum memory protocol.* Physical Review A **79**, 053851 (2009). doi:10.1103/PhysRevA.79.053851.

[105] S. A. Moiseev and S. Kroll. *Complete Reconstruction of the Quantum State of a Single-Photon Wave Packet Absorbed by a Doppler-Broadened Transition.* Physical Review Letters **87**, 173601 (2001). doi:10.1103/PhysRevLett.87.173601.

[106] E. Fraval, M. J. Sellars, and J. J. Longdell. *Method of Extending Hyperfine Coherence Times in* $Pr^{3+} : Y_2SiO_5$. Physical Review Letters **92**, 077601 (2004). doi:10.1103/PhysRevLett.92.077601.

[107] E. Fraval, M. J. Sellars, and J. J. Longdell. *Dynamic Decoherence Control of a Solid-State Nuclear-Quadrupole Qubit.* Physical Review Letters **95**, 030506 (2005). doi:10.1103/PhysRevLett.95.030506.

[108] M. Nilsson and S. Kroll. *Solid state quantum memory using complete absorption and re-emission of photons by tailored and externally controlled inhomogeneous absorption profiles.* Optics Communications **247**, 393 (2005). doi:10.1016/j.optcom.2004.11.077.

[109] B. Kraus, W. Tittel, N. Gisin, M. Nilsson, S. Kroll, and J. I. Cirac. *Quantum memory for nonstationary light fields based on controlled reversible inhomogeneous broadening.* Physical Review A **73**, 020302 (2006). doi:10.1103/PhysRevA.73.020302.

[110] J. J. Longdell, G. Hétet, P. K. Lam, and M. J. Sellars. *Analytic treatment of controlled reversible inhomogeneous broadening quantum memories for light using two-level atoms.* Physical Review A **78**, 032337 (2008). doi:10.1103/PhysRevA.78.032337.

[111] A. L. Alexander, J. J. Longdell, M. J. Sellars, and N. B. Manson. *Photon Echoes Produced by Switching Electric Fields.* Physical Review Letters **96**, 043602 (2006). doi:10.1103/PhysRevLett.96.043602.

[112] G. Hétet, J. J. Longdell, A. L. Alexander, P. K. Lam, and M. J. Sellars. *Electro-Optic Quantum Memory for Light Using Two-Level Atoms.* Physical Review Letters **100**, 023601 (2008). doi:10.1103/PhysRevLett.100.023601.

[113] B. Lauritzen, J. Minář, H. de Riedmatten, M. Afzelius, and N. Gisin. *Approaches for a quantum memory at telecommunication wavelengths.* Physical Review A **83**, 012318 (2011). doi:10.1103/PhysRevA.83.012318.

[114] F. Carreno and M. Antón. *Gradient echo memory in a tripod-like dense atomic medium.* Optics Communications **283**, 4787 (2010). doi:10.1016/j.optcom.2010.07.024.

[115] D. Viscor, A. Ferraro, Y. Loiko, R. Corbalán, J. Mompart, and V. Ahufinger. *Optical quantum memory for polarization qubits with V-type three-level atoms.* Journal of Physics B: Atomic, Molecular and Optical Physics **44**, 195504 (2011). doi:10.1088/0953-4075/44/19/195504.

[116] D. Viscor, A. Ferraro, Y. Loiko, J. Mompart, and V. Ahufinger. *Quantum-state storage and processing for polarization qubits in an inhomogeneously broadened Λ-type three-level medium.* Physical Review A **84**, 042314 (2011). doi:10.1103/PhysRevA.84.042314.

[117] G. Hétet, M. Hosseini, B. M. Sparkes, D. Oblak, P. K. Lam, and B. C. Buchler. *Photon echoes generated by reversing magnetic field gradients in a rubidium vapor.* Optics Letters **33**, 2323 (2008). doi:10.1364/OL.33.002323.

[118] J.-L. Le Gouet and P. R. Berman. *Raman scheme for adjustable-bandwidth quantum memory.* Physical Review A **80**, 012320 (2009). doi:10.1103/PhysRevA.80.012320.

[119] B. M. Sparkes, M. Hosseini, G. Hétet, P. K. Lam, and B. C. Buchler. *ac Stark gradient echo memory in cold atoms.* Physical Review A **82**, 043847 (2010). doi:10.1103/PhysRevA.82.043847.

[120] M. Hosseini, B. Sparkes, G. Campbell, P. Lam, and B. Buchler. *Storage and manipulation of light using a Raman gradient-echo process.* Journal of Physics B: Atomic, Molecular and Optical Physics **45**, 124004 (2012). doi:10.1088/0953-4075/45/12/124004.

[121] W. H. Hesselink and D. A. Wiersma. *Picosecond Photon Echoes Stimulated from an Accumulated Grating.* Physical Review Letters **43**, 1991 (1979). doi:10.1103/PhysRevLett.43.1991.

[122] L. Rippe, M. Nilsson, S. Kroll, R. Klieber, and D. Suter. *Experimental demonstration of efficient and selective population transfer and qubit distillation in a rare-earth-metal-ion-doped crystal.* Physical Review A **71**, 062328 (2005). doi:10.1103/PhysRevA.71.062328.

[123] H. de Riedmatten, M. Afzelius, M. U. Staudt, C. Simon, and N. Gisin. *A solid-state light-matter interface at the single-photon level.* Nature **456**, 773 (2008). doi:10.1038/nature07607.

[124] M. Mitsunaga, R. Yano, and N. Uesugi. *Spectrally programmed stimulated photon echo.* Optics letters **16**, 264 (1991). doi:10.1364/OL.16.000264.

[125] M. Afzelius, I. Usmani, A. Amari, B. Lauritzen, A. Walther, C. Simon, N. Sangouard, J. Minář, H. de Riedmatten, N. Gisin, and S. Kroll. *Demonstration of Atomic Frequency Comb Memory for Light with Spin-Wave Storage.* Physical Review Letters **104**, 040503 (2010). doi:10.1103/PhysRevLett.104.040503.

[126] J. Minář, N. Sangouard, M. Afzelius, H. de Riedmatten, and N. Gisin. *Spin-wave storage using chirped control fields in atomic frequency comb-based quantum memory.* Physical Review A **82**, 042309 (2010). doi:10.1103/PhysRevA.82.042309.

[127] T. Chanelière, J. Ruggiero, M. Bonarota, M. Afzelius, and J. Le Gouet. *Efficient light storage in a crystal using an atomic frequency comb.* New Journal of Physics **12**, 023025 (2010). doi:10.1088/1367-2630/12/2/023025.

[128] M. Bonarota, J. Ruggiero, J. L. L. Gouet, and T. Chanelière. *Efficiency optimization for atomic frequency comb storage.* Physical Review A **81**, 033803 (2010). doi:10.1103/PhysRevA.81.033803.

[129] J. Longdell. *Quantum information: Entanglement on ice.* Nature **469**, 475 (2011). doi:10.1038/469475a.

[130] I. Usmani, C. Clausen, F. Bussières, N. Sangouard, M. Afzelius, and N. Gisin. *Heralded quantum entanglement between two crystals.* Nature Photonics **6**, 234 (2012). doi:10.1038/nphoton.2012.34.

[131] C. Clausen, F. Bussières, M. Afzelius, and N. Gisin. *Quantum Storage of Heralded Polarization Qubits in Birefringent and Anisotropically*

Absorbing Materials. Physical Review Letters **108**, 190503 (2012). doi:10.1103/PhysRevLett.108.190503.

[132] M. Gundoğan, P. M. Ledingham, A. Almasi, M. Cristiani, and H. de Riedmatten. *Quantum Storage of a Photonic Polarization Qubit in a Solid.* Physical Review Letters **108**, 190504 (2012). doi:10.1103/PhysRevLett.108.190504.

[133] Z. Zhou, W. Lin, M. Yang, C. Li, and G. Guo. *Realization of Reliable Solid-State Quantum Memory for Photonic Polarization Qubit.* Physical Review Letters **108**, 190505 (2012). doi:10.1103/PhysRevLett.108.190505.

[134] N. Piro, F. Rohde, C. Schuck, M. Almendros, J. Huwer, J. Ghosh, A. Haase, M. Hennrich, F. Dubin, and J. Eschner. *Heralded single-photon absorption by a single atom.* Nature Physics **7**, 17 (2011). doi:10.1038/nphys1805.

[135] T. Wilk, S. Webster, A. Kuhn, and G. Rempe. *Single-atom single-photon quantum interface.* Science **317**, 488 (2007). doi:10.1126/science.1143835.

[136] M. Mucke, E. Figueroa, J. Bochmann, C. Hahn, K. Murr, S. Ritter, C. Villas-Boas, and G. Rempe. *Electromagnetically induced transparency with single atoms in a cavity.* Nature **465**, 755 (2010). doi:10.1038/nature09093.

[137] T. Kampschulte, W. Alt, S. Brakhane, M. Eckstein, R. Reimann, A. Widera, and D. Meschede. *Optical Control of the Refractive Index of a Single Atom.* Physical Review Letters **105**, 153603 (2010). doi:10.1103/PhysRevLett.105.153603.

[138] A. D. Boozer, A. Boca, R. Miller, T. E. Northup, and H. J. Kimble. *Reversible State Transfer between Light and a Single Trapped Atom.* Physical Review Letters **98**, 193601 (2007). doi:10.1103/PhysRevLett.98.193601.

[139] A. Amari, A. Walther, M. Sabooni, M. Huang, S. Kroll, M. Afzelius, I. Usmani, B. Lauritzen, N. Sangouard, H. de Riedmatten, and N. Gisin. *Towards an efficient atomic frequency comb quantum memory.* Journal of Luminescence **130**, 1579 (2010). doi:10.1016/j.jlumin.2010.01.012.

[140] M. O. Scully. *From lasers and masers to phaseonium and phasers.* Physics Reports **219**, 191 (1992). doi:10.1016/0370-1573(92)90136-N.

[141] A. I. Lvovsky, B. C. Sanders, and W. Tittel. *Optical quantum memory.* Nature Photonics **3**, 706 (2009). doi:10.1038/nphoton.2009.231.

[142] H. d. Riedmatten. *Quantum optics: Light storage at record bandwidths.* Nature Photonics **4**, 206 (2010). doi:10.1038/nphoton.2010.81.

[143] E. Saglamyurek, N. Sinclair, J. Jin, J. A. Slater, D. Oblak, F. Bussières, M. George, R. Ricken, W. Sohler, and W. Tittel. *Conditional Detection of Pure Quantum States of Light after Storage in a Tm-Doped Waveguide.* Physical Review Letters **108**, 083602 (2012). doi:10.1103/PhysRevLett.108.083602.

[144] H. Kimble. *The quantum internet.* Nature **453**, 1023 (2008). doi:10.1038/nature07127.

[145] M. U. Staudt, M. Afzelius, H. de Riedmatten, S. R. Hastings-Simon, C. Simon, R. Ricken, H. Suche, W. Sohler, and N. Gisin. *Interference of Multimode Photon Echoes Generated in Spatially Separated Solid-State Atomic Ensembles.* Physical Review Letters **99**, 173602 (2007). doi:10.1103/PhysRevLett.99.173602.

[146] M. D. Lukin, S. F. Yelin, and M. Fleischhauer. *Entanglement of Atomic Ensembles by Trapping Correlated Photon States.* Physical Review Letters **84**, 4232 (2000). doi:10.1103/PhysRevLett.84.4232.

[147] S. A. Moiseev and B. S. Ham. *Photon-echo quantum memory with efficient multipulse readings.* Physical Review A **70**, 063809 (2004). doi:10.1103/PhysRevA.70.063809.

[148] M. O. Scully and M. S. Zubairy. *Quantum Optics*, (Cambridge University Press 2001).

[149] S. E. Harris. *Electromagnetically induced transparency with matched pulses.* Physical Review Letters **70**, 552 (1993). doi:10.1103/PhysRevLett.70.552.

[150] S. E. Harris. *Normal modes for electromagnetically induced transparency.* Physical Review Letters **72**, 52 (1994). doi:10.1103/PhysRevLett.72.52.

[151] M. Fleischhauer and T. Richter. *Pulse matching and correlation of phase fluctuations in Λ systems.* Physical Review A **51**, 2430 (1995). doi:10.1103/PhysRevA.51.2430.

[152] V. Kozlov and J. Eberly. *Ultrashort pulses in phaseonium: the interplay between SIT and EIT.* Optics Communications **179**, 85 (2000). doi:10.1016/S0030-4018(99)00730-0.

[153] J. H. Eberly and V. V. Kozlov. *Wave Equation for Dark Coherence in Three-Level Media.* Physical Review Letters **88**, 243604 (2002). doi:10.1103/PhysRevLett.88.243604.

[154] M. J. Konopnicki and J. H. Eberly. *Simultaneous propagation of short different-wavelength optical pulses.* Physical Review A **24**, 2567 (1981). doi:10.1103/PhysRevA.24.2567.

[155] R. Grobe, F. T. Hioe, and J. H. Eberly. *Formation of Shape-Preserving Pulses in a Nonlinear Adiabatically Integrable System.* Physical Review Letters **73**, 3183 (1994). doi:10.1103/PhysRevLett.73.3183.

[156] J. H. Eberly, M. L. Pons, and H. R. Haq. *Dressed-field pulses in an absorbing medium.* Physical Review Letters **72**, 56 (1994). doi:10.1103/PhysRevLett.72.56.

[157] N. Sangouard, L. P. Yatsenko, B. W. Shore, and T. Halfmann. *Preparation of nondegenerate coherent superpositions in a three-state ladder system assisted by Stark shifts.* Physical Review A **73**, 043415 (2006). doi:10.1103/PhysRevA.73.043415.

[158] V. V. Kozlov and E. B. Kozlova. *Adiabatic and nonadiabatic preparation of a ground-state coherence in an optically thick lambda medium.* Optics Communications **282**, 892 (2009). doi:10.1016/j.optcom.2008.11.059.

[159] M. Fleischhauer and A. S. Manka. *Propagation of laser pulses and coherent population transfer in dissipative three-level systems: An adiabatic dressed-state picture.* Physical Review A **54**, 794 (1996). doi:10.1103/PhysRevA.54.794.

[160] E. Arimondo. *Progress in Optics, Vol. 35*, (Elsevier , New York1996).

[161] B. D. Clader and J. H. Eberly. *Two-pulse propagation in a partially phase-coherent medium.* Physical Review A **78**, 033803 (2008). doi:10.1103/PhysRevA.78.033803.

[162] E. A. Korsunsky and D. V. Kosachiov. *Phase-dependent nonlinear optics with double-Λ atoms.* Physical Review A **60**, 4996 (1999). doi:10.1103/PhysRevA.60.4996.

[163] M. G. Payne and L. Deng. *Quantum Entanglement of Fock States with Perfectly Efficient Ultraslow Single-Probe Photon Four-Wave Mixing.* Physical Review Letters **91**, 123602 (2003). doi:10.1103/PhysRevLett.91.123602.

[164] C. Polycarpou, K. N. Cassemiro, G. Venturi, A. Zavatta, and M. Bellini. *Adaptive Detection of Arbitrarily Shaped Ultrashort Quantum Light States.* Physical Review Letters **109**, 053602 (2012). doi:10.1103/PhysRevLett.109.053602.

[165] R. García-Maraver, R. Corbalán, K. Eckert, S. Rebić, M. Artoni, and J. Mompart. *Cavity QED quantum phase gates for a single longitudinal mode of the intracavity field.* Physical Review A **70**, 062324 (2004). doi:10.1103/PhysRevA.70.062324.

[166] A. Raczyński and J. Zaremba. *Controlled light storage in a double lambda system.* Optics Communications **209**, 149 (2002). doi:10.1016/S0030-4018(02)01642-5.

[167] A. Raczyński, J. Zaremba, and S. Zielinska-Kaniasty. *Electromagnetically induced transparency and storing of a pair of pulses of light.* Physical Review A **69**, 043801 (2004). doi:10.1103/PhysRevA.69.043801.

[168] Z. Li, L. Xu, and K. Wang. *The dark-state polaritons of a double-Λ atomic ensemble.* Physics Letters A **346**, 269 (2005). doi:10.1016/j.physleta.2005.08.009.

[169] Y.-W. Lin, W.-T. Liao, T. Peters, H.-C. Chou, J.-S. Wang, H.-W. Cho, P.-C. Kuan, and I. A. Yu. *Stationary Light Pulses in Cold Atomic Media and without Bragg Gratings.* Physical Review Letters **102**, 213601 (2009). doi:10.1103/PhysRevLett.102.213601.

[170] J.-H. Wu, M. Artoni, and G. C. La Rocca. *Stationary light pulses in cold thermal atomic clouds.* Physical Review A **82**, 013807 (2010). doi:10.1103/PhysRevA.82.013807.

[171] J. H. Wu, M. Artoni, and G. C. La Rocca. *Decay of stationary light pulses in ultracold atoms.* Physical Review A **81**, 033822 (2010). doi:10.1103/PhysRevA.81.033822.

[172] J. H. Wu, M. Artoni, and G. C. La Rocca. *All-Optical Light Confinement in Dynamic Cavities in Cold Atoms.* Physical Review Letters **103**, 133601 (2009). doi:10.1103/PhysRevLett.103.133601.

[173] S. Lloyd, M. S. Shahriar, J. H. Shapiro, and P. R. Hemmer. *Long Distance, Unconditional Teleportation of Atomic States via Complete Bell State Measurements.* Physical Review Letters **87**, 167903 (2001). doi:10.1103/PhysRevLett.87.167903.

[174] J. H. Shapiro. *Architectures for long-distance quantum teleportation.* New Journal of Physics **4**, 47 (2002). doi:10.1088/1367-2630/4/1/347.

[175] Z. J. Liu, W. B. Yan, and L. Zhou. *Collective excitation and photon entanglement in double-Λ atomic ensemble.* The European Physical Journal D - Atomic, Molecular, Optical and Plasma Physics **57**, 111 (2010). doi:10.1140/epjd/e2009-00323-2.

[176] Y. D. Chong and M. Soljačić. *Dark-state polaritons in single- and double-Λ media.* Physical Review A **77**, 013823 (2008). doi:10.1103/PhysRevA.77.013823.

[177] A. J. Merriam, S. J. Sharpe, M. Shverdin, D. Manuszak, G. Y. Yin, and S. E. Harris. *Efficient Nonlinear Frequency Conversion in an All-Resonant Double-Λ System.* Physical Review Letters **84**, 5308 (2000). doi:10.1103/PhysRevLett.84.5308.

[178] Z. Li, L. Deng, L. Xu, and K. Wang. *Controllable shape-matched propagation of two signal beams in a double-Λ atomic ensemble.* The European Physical Journal D - Atomic, Molecular, Optical and Plasma Physics **40**, 147 (2006). doi:10.1140/epjd/e2006-00141-0.

[179] M. Jain, H. Xia, G. Y. Yin, A. J. Merriam, and S. E. Harris. *Efficient Nonlinear Frequency Conversion with Maximal Atomic Coherence.* Physical Review Letters **77**, 4326 (1996). doi:10.1103/PhysRevLett.77.4326.

[180] J. Mompart, V. Ahufinger, and G. Birkl. *Coherent patterning of matter waves with subwavelength localization.* Physical Review A **79**, 053638 (2009). doi:10.1103/PhysRevA.79.053638.

[181] K. Bergmann, H. Theuer, and B. W. Shore. *Coherent population transfer among quantum states of atoms and molecules.* Reviews of Modern Physics **70**, 1003 (1998). doi:10.1103/RevModPhys.70.1003.

[182] G. Alzetta, L. Moi, and G. Orriols. *Nonabsorption hyperfine resonances in a sodium vapour irradiated by a multimode dye-laser.* Il Nuovo Cimento B (1971-1996) **52**, 209 (1979). doi:10.1007/BF02739035.

[183] J. P. Marangos. *Electromagnetically induced transparency.* Journal of Modern Optics **45**, 471 (1998). doi:10.1080/09500349808231909.

[184] C. Zhang, S. L. Rolston, and S. Das Sarma. *Manipulation of single neutral atoms in optical lattices.* Physical Review A **74**, 042316 (2006). doi:10.1103/PhysRevA.74.042316.

[185] C. Weitenberg, M. Endres, J. F. Sherson, M. Cheneau, P. Schauß, T. Fukuhara, I. Bloch, and S. Kuhr. *Single-spin addressing in an atomic Mott insulator.* Nature **471**, 319 (2011). doi:10.1038/nature09827.

[186] M. Endres, M. Cheneau, T. Fukuhara, C. Weitenberg, P. Schauß, C. Gross, L. Mazza, M. C. Banuls, L. Pollet, I. Bloch, and S. Kuhr. *Observation of Correlated Particle-Hole Pairs and String Order in Low-Dimensional Mott Insulators.* Science **334**, 200 (2011). doi:10.1126/science.1209284.

[187] N. S. Ginsberg, S. R. Garner, and L. V. Hau. *Coherent control of optical information with matter wave dynamics.* Nature **445**, 623 (2007). doi:10.1038/nature05493.

[188] I. Bloch, J. Dalibard, and W. Zwerger. *Many-body physics with ultracold gases.* Reviews of Modern Physics **80**, 885 (2008). doi:10.1103/RevModPhys.80.885.

[189] G. K. Brennen, C. M. Caves, P. S. Jessen, and I. H. Deutsch. *Quantum Logic Gates in Optical Lattices.* Physical Review Letters **82**, 1060 (1999). doi:10.1103/PhysRevLett.82.1060.

[190] R. Raussendorf and H. J. Briegel. *A One-Way Quantum Computer*. Physical Review Letters **86**, 5188 (2001). doi:10.1103/PhysRevLett.86.5188.

[191] D. Jaksch and P. Zoller. *The cold atom Hubbard toolbox*. Annals of Physics **315**, 52 (2005). doi:10.1016/j.aop.2004.09.010.

[192] R. Scheunemann, F. S. Cataliotti, T. W. Hansch, and M. Weitz. *Resolving and addressing atoms in individual sites of a CO_2-laser optical lattice*. Physical Review A **62**, 051801 (2000). doi:10.1103/PhysRevA.62.051801.

[193] R. Dumke, M. Volk, T. Muther, F. B. J. Buchkremer, G. Birkl, and W. Ertmer. *Micro-optical Realization of Arrays of Selectively Addressable Dipole Traps: A Scalable Configuration for Quantum Computation with Atomic Qubits*. Physical Review Letters **89**, 097903 (2002). doi:10.1103/PhysRevLett.89.097903.

[194] S. Peil, J. V. Porto, B. L. Tolra, J. M. Obrecht, B. E. King, M. Subbotin, S. L. Rolston, and W. D. Phillips. *Patterned loading of a Bose-Einstein condensate into an optical lattice*. Physical Review A **67**, 051603 (2003). doi:10.1103/PhysRevA.67.051603.

[195] Y. Miroshnychenko, W. Alt, I. Dotsenko, L. Forster, M. Khudaverdyan, D. Meschede, D. Schrader, and A. Rauschenbeutel. *Quantum engineering: An atom-sorting machine*. Nature **442**, 151 (2006). doi:10.1038/442151a.

[196] K. D. Nelson, X. Li, and D. S. Weiss. *Imaging single atoms in a three-dimensional array*. Nature Physics **3**, 556 (2007). doi:10.1038/nphys645.

[197] G. Birkl and J. Fortágh. *Micro traps for quantum information processing and precision force sensing*. Laser & Photonics Reviews **1**, 12 (2007). doi:10.1002/lpor.200610002.

[198] D. Schrader, I. Dotsenko, M. Khudaverdyan, Y. Miroshnychenko, A. Rauschenbeutel, and D. Meschede. *Neutral Atom Quantum Register*. Physical Review Letters **93**, 150501 (2004). doi:10.1103/PhysRevLett.93.150501.

[199] P. Wurtz, T. Langen, T. Gericke, A. Koglbauer, and H. Ott. *Experimental Demonstration of Single-Site Addressability in a Two-Dimensional Optical Lattice*. Physical Review Letters **103**, 080404 (2009). doi:10.1103/PhysRevLett.103.080404.

[200] T. Gericke, P. Wurtz, D. Reitz, T. Langen, and H. Ott. *High-resolution scanning electron microscopy of an ultracold quantum gas.* Nature Physics **4**, 949 (2008). doi:10.1038/nphys1102.

[201] W. S. Bakr, J. I. Gillen, A. Peng, S. Folling, and M. Greiner. *A quantum gas microscope for detecting single atoms in a Hubbard-regime optical lattice.* Nature **462**, 74 (2009). doi:10.1038/nature08482.

[202] W. S. Bakr, A. Peng, M. E. Tai, R. Ma, J. Simon, J. I. Gillen, S. Folling, L. Pollet, and M. Greiner. *Probing the Superfluid-to-Mott Insulator Transition at the Single-Atom Level.* Science **329**, 547 (2010). doi:10.1126/science.1192368.

[203] N. Gemelke, X. Zhang, C.-L. Hung, and C. Chin. *In situ observation of incompressible Mott-insulating domains in ultracold atomic gases.* Nature **460**, 995 (2009). doi:10.1038/nature08244.

[204] M. Karski, L. Forster, J. M. Choi, W. Alt, A. Widera, and D. Meschede. *Nearest-Neighbor Detection of Atoms in a 1D Optical Lattice by Fluorescence Imaging.* Physical Review Letters **102**, 053001 (2009). doi:10.1103/PhysRevLett.102.053001.

[205] J. F. Sherson, C. Weitenberg, M. Endres, M. Cheneau, I. Bloch, and S. Kuhr. *Single-atom-resolved fluorescence imaging of an atomic Mott insulator.* Nature **467**, 68 (2010). doi:10.1038/nature09378.

[206] G. S. Agarwal and K. T. Kapale. *Subwavelength atom localization via coherent population trapping.* Journal of Physics B: Atomic, Molecular and Optical Physics **39**, 3437 (2006). doi:10.1088/0953-4075/39/17/002.

[207] J. Cho. *Addressing Individual Atoms in Optical Lattices with Standing-Wave Driving Fields.* Physical Review Letters **99**, 020502 (2007). doi:10.1103/PhysRevLett.99.020502.

[208] A. V. Gorshkov, L. Jiang, M. Greiner, P. Zoller, and M. D. Lukin. *Coherent Quantum Optical Control with Subwavelength Resolution.* Physical Review Letters **100**, 093005 (2008). doi:10.1103/PhysRevLett.100.093005.

[209] M. Holland, S. Marksteiner, P. Marte, and P. Zoller. *Measurement Induced Localization from Spontaneous Decay.* Physical Review Letters **76**, 3683 (1996). doi:10.1103/PhysRevLett.76.3683.

[210] E. Paspalakis and P. L. Knight. *Localizing an atom via quantum interference.* Physical Review A **63**, 065802 (2001). doi:10.1103/PhysRevA.63.065802.

[211] M. Sahrai, H. Tajalli, K. T. Kapale, and M. S. Zubairy. *Subwavelength atom localization via amplitude and phase control of the absorption spectrum.* Physical Review A **72**, 013820 (2005). doi:10.1103/PhysRevA.72.013820.

[212] M. Kiffner, J. Evers, and M. S. Zubairy. *Resonant Interferometric Lithography beyond the Diffraction Limit.* Physical Review Letters **100**, 073602 (2008). doi:10.1103/PhysRevLett.100.073602.

[213] D. D. Yavuz and N. A. Proite. *Nanoscale resolution fluorescence microscopy using electromagnetically induced transparency.* Physical Review A **76**, 041802 (2007). doi:10.1103/PhysRevA.76.041802.

[214] N. R. Heckenberg, R. McDuff, C. P. Smith, H. Rubinsztein-Dunlop, and M. J. Wegener. *Laser beams with phase singularities.* Optical and Quantum Electronics **24**, S951 (1992). doi:10.1007/BF01588597.

[215] L. Isenhower, W. Williams, A. Dally, and M. Saffman. *Atom trapping in an interferometrically generated bottle beam trap.* Optics Letters **34**, 1159 (2009). doi:10.1364/OL.34.001159.

[216] S. Bergamini, B. Darquié, M. Jones, L. Jacubowiez, A. Browaeys, and P. Grangier. *Holographic generation of microtrap arrays for single atoms by use of a programmable phase modulator.* Journal of the Optical Society of America B **21**, 1889 (2004). doi:10.1364/JOSAB.21.001889.

[217] J. Kruse, C. Gierl, M. Schlosser, and G. Birkl. *Reconfigurable site-selective manipulation of atomic quantum systems in two-dimensional arrays of dipole traps.* Physical Review A **81**, 060308 (2010). doi:10.1103/PhysRevA.81.060308.

[218] V. Parigi, A. Zavatta, M. Kim, and M. Bellini. *Probing Quantum Commutation Rules by Addition and Subtraction of Single Photons to/from a Light Field.* Science **317**, 1890 (2007). doi:10.1126/science.1146204.

[219] J. P. Torres, C. I. Osorio, and L. Torner. *Orbital angular momentum of entangled counterpropagating photons.* Optics Letters **29**, 1939 (2004). doi:10.1364/OL.29.001939.

[220] S. Carrasco, J. P. Torres, L. Torner, A. Sergienko, B. E. A. Saleh, and M. C. Teich. *Spatial-to-spectral mapping in spontaneous parametric down-conversion.* Physical Review A **70**, 043817 (2004). doi:10.1103/PhysRevA.70.043817.

[221] A. Valencia, A. Ceré, X. Shi, G. Molina-Terriza, and J. P. Torres. *Shaping the Waveform of Entangled Photons.* Physical Review Letters **99**, 243601 (2007). doi:10.1103/PhysRevLett.99.243601.

[222] I. A. Walmsley and M. G. Raymer. *Toward Quantum-Information Processing with Photons.* Science **307**, 1733 (2005). doi:10.1126/science.1107451.

[223] C. K. Hong, Z. Y. Ou, and L. Mandel. *Measurement of subpicosecond time intervals between two photons by interference.* Physical Review Letters **59**, 2044 (1987). doi:10.1103/PhysRevLett.59.2044.

[224] F. A. Bovino, G. Castagnoli, A. Ekert, P. Horodecki, C. M. Alves, and A. V. Sergienko. *Direct Measurement of Nonlinear Properties of Bipartite Quantum States.* Physical Review Letters **95**, 240407 (2005). doi:10.1103/PhysRevLett.95.240407.

[225] P. P. Rohde and T. C. Ralph. *Frequency and temporal effects in linear optical quantum computing.* Physical Review A **71**, 032320 (2005). doi:10.1103/PhysRevA.71.032320.

[226] P. P. Rohde, G. J. Pryde, J. L. O Brien, and T. C. Ralph. *Quantum-gate characterization in an extended Hilbert space.* Physical Review A **72**, 032306 (2005). doi:10.1103/PhysRevA.72.032306.

[227] T. Aichele, A. Lvovsky, and S. Schiller. *Optical mode characterization of single photons prepared by means of conditional measurements on a biphoton state.* The European Physical Journal D - Atomic, Molecular, Optical and Plasma Physics **18**, 237 (2002). doi:10.1140/epjd/e20020028.

[228] W. P. Grice, A. B. U Ren, and I. A. Walmsley. *Eliminating frequency and space-time correlations in multiphoton states.* Physical Review A **64**, 063815 (2001). doi:10.1103/PhysRevA.64.063815.

[229] O. Kuzucu, M. Fiorentino, M. A. Albota, F. N. C. Wong, and F. X. Kartner. *Two-Photon Coincident-Frequency Entanglement via Ex-*

tended Phase Matching. Physical Review Letters **94**, 083601 (2005). doi:10.1103/PhysRevLett.94.083601.

[230] A. B. U Ren, C. Silberhorn, R. Erdmann, K. Banaszek, W. P. Grice, I. A. Walmsley, and M. G. Raymer. *Generation of Pure-State Single-Photon Wavepackets by Conditional Preparation Based on Spontaneous Parametric Downconversion.* Laser Physics **15**, 146 (2005).

[231] M. B. Nasr, S. Carrasco, B. E. A. Saleh, A. V. Sergienko, M. C. Teich, J. P. Torres, L. Torner, D. S. Hum, and M. M. Fejer. *Ultrabroadband Biphotons Generated via Chirped Quasi-Phase-Matched Optical Parametric Down-Conversion.* Physical Review Letters **100**, 183601 (2008). doi:10.1103/PhysRevLett.100.183601.

[232] M. Hendrych, M. Micuda, and J. P. Torres. *Tunable control of the frequency correlations of entangled photons.* Optics Letters **32**, 2339 (2007). doi:10.1364/OL.32.002339.

[233] M. G. Raymer, J. Noh, K. Banaszek, and I. A. Walmsley. *Pure-state single-photon wave-packet generation by parametric down-conversion in a distributed microcavity.* Physical Review A **72**, 023825 (2005). doi:10.1103/PhysRevA.72.023825.

[234] J. S. Neergaard-Nielsen, B. M. Nielsen, H. Takahashi, A. I. Vistnes, and E. S. Polzik. *High purity bright single photon source.* Optics Express **15**, 7940 (2007). doi:10.1364/OE.15.007940.

[235] P. J. Mosley, J. S. Lundeen, B. J. Smith, P. Wasylczyk, A. B. U Ren, C. Silberhorn, and I. A. Walmsley. *Heralded Generation of Ultrafast Single Photons in Pure Quantum States.* Physical Review Letters **100**, 133601 (2008). doi:10.1103/PhysRevLett.100.133601.

[236] C. I. Osorio, A. Valencia, and J. P. Torres. *Spatiotemporal correlations in entangled photons generated by spontaneous parametric down conversion.* New Journal of Physics **10**, 113012 (2008). doi:10.1088/1367-2630/10/11/113012.

[237] L. E. Vicent, A. B. U Ren, R. Rangarajan, C. I. Osorio, J. P. Torres, L. Zhang, and I. A. Walmsley. *Design of bright, fiber-coupled and fully factorable photon pair sources.* New Journal of Physics **12**, 093027 (2010). doi:10.1088/1367-2630/12/9/093027.

[238] U. Leonhardt. *Measuring the Quantum State of Light*, (Cambridge University Press 1997).

[239] A. Zavatta, S. Viciani, and M. Bellini. *Non-classical field characterization by high-frequency, time-domain quantum homodyne tomography.* Laser Physics Letters **3**, 3 (2006). doi:10.1002/lapl.200510060.

[240] A. I. Lvovsky and M. G. Raymer. *Continuous-variable optical quantum-state tomography.* Reviews of Modern Physics **81**, 299 (2009). doi:10.1103/RevModPhys.81.299.

[241] D. C. Burnham and D. L. Weinberg. *Observation of Simultaneity in Parametric Production of Optical Photon Pairs.* Physical Review Letters **25**, 84 (1970). doi:10.1103/PhysRevLett.25.84.

[242] D. Klyshko. *Photons and nonlinear optics*, (Gordon and Breach Science 1988).

[243] P. A. Franken and J. F. Ward. *Optical Harmonics and Nonlinear Phenomena.* Reviews of Modern Physics **35**, 23 (1963). doi:10.1103/RevModPhys.35.23.

[244] D. N. Klyshko. *Scattering of Light in a Medium with Nonlinear Polarizability.* Soviet Journal of Experimental and Theoretical Physics **28**, 522 (1969).

[245] J. E. Midwinter and J. Warner. *The effects of phase matching method and of uniaxial crystal symmetry on the polar distribution of second-order non-linear optical polarization.* British Journal of Applied Physics **16**, 1135 (2002). doi:10.1088/0508-3443/16/8/312.

[246] M. Bass and V. Mahajan. *Handbook of optics*, vol. 2, (McGraw-Hill 2001).